DOI
https://orcid.org/0000-0001-5672-7389

VILNIUS UNIVERSITY
CENTER FOR PHYSICAL SCIENCES AND TECHNOLOGY

Darius
Urbonas

Silicon micro ring resonators decorated by metal and perforations for optical sensors

DOCTORAL DISSERTATION

Technological sciences,
Material Engineering T 008

VILNIUS 2022

This dissertation was written between 2014 and 2021 at the Center for Physical Sciences and Technology. The research was supported by a grant VP1–3.1-SMM-10-V02–026 from the European Social Fund Agency in Lithuania, European Cooperation in Science and Technology (COST) Action (MP1205), by a grant No. S-LJB-19-1 from Research Council of Lithuania the Joint Research Project hybRING between Lithuania and Japan. Part of the FDTD simulation work was performed on the swinSTAR supercomputer at Swinburne University of Technology.

Academic supervisor:
Dr. Raimondas Petruškevičius (Center for Physical Sciences and Technology, Technological sciences, Material engineering — T 008).

Dissertation Defence Panel:
Chairman — Dr. Gediminas Račiukaitis (Center for Physical Sciences and Technology, Technological sciences, Material engineering — T 008).
Members:
Prof. Dr. Taro Arakawa (Yokohama National University, Technological sciences, Material engineering — T 008),
Prof. Dr. Zigmas Balevičius (Center for Physical Sciences and Technology, Technological sciences, Material engineering — T 008),
Prof. Habil. Dr. Gediminas Juzeliūnas (Vilnius University, Technological sciences, Material engineering — T 008),
Prof. Dr. Darius Viržonis (Kaunas University of Technology, Technological sciences, Material engineering — T 008).

The dissertation shall be defended at a public meeting of the Dissertation Defence Panel at 10 (hour), on 02 September 2022 in the hall of FTMC Institute of Physics and remote way.
Address: Savanoriu Ave. 231, LT-02300 Vilnius, Lithuania
Tel. +370 5 264 8884; e-mail: office@ftmc.lt

The text of this dissertation can be accessed at the libraries of Center for Physical Sciences and Technology and Vilnius University, as well as on the website of Vilnius University: www.vu.lt/lt/naujienos/ivykiu-kalendorius

DOI
https://orcid.org/0000-0001-5672-7389

VILNIAUS UNIVERSITETAS
FIZINIŲ IR TECHNOLOGIJOS MOKSLŲ CENTRAS

Darius
Urbonas

Metalu ir perforacijomis dekoruoti silicio mikrožiediniai rezonatoriai optiniams jutikliams

DAKTARO DISERTACIJA

Technologijos mokslai,
Medžiagų inžinerija T 008

VILNIUS 2022

Ši disertacija buvo rašoma 2014-2021 m. Fizinių ir technologijos mokslų centre. Tyrimą rėmė Europos socialinio fondo agentūros Lietuvoje dotacija VP1-3.1-SMM-10-V02-026, Europos bendradarbiavimo mokslo ir technologijų srityje (COST) veiksmas (MP1205), Lietuvos mokslo tarybos dotacija Nr. S-LJB-19-1 Lietuvos ir Japonijos bendras mokslinių tyrimų projektas hybRING. Dalis FDTD modeliavimo darbų atlikta Swinburne technologijos universiteto superkompiuteriu swinSTAR.

Mokslinis vadovas:
prof. dr. Raimondas Petruškevičius (Fizinių ir technologijos mokslų centras, technologijos mokslai, medžiagų inžinerija, T 008).

Gynimo taryba:
Pirmininkas — dr. Gediminas Račiukaitis (Fizinių ir technologijos mokslų centras, technologijos mokslai, medžiagų inžinerija – T 008).
Nariai:
Prof. dr. Taro Arakawa (Yokohamos nacionalinis universitetas, technologijos mokslai, medžiagų inžinerija – T 008),
Prof. dr. Zigmas Balevičius (Fizinių ir technologijos mokslų centras, technologijos mokslai, medžiagų inžinerija – T 008),
Prof. habil. dr. Gediminas Juzeliūnas (Vilniaus universitetas, technologijos mokslai, medžiagų inžinerija – T 008),
Prof. dr. Darius Viržonis (Kauno technologijos universitetas, technologijos mokslai, medžiagų inžinerija – T 008).

Disertacija ginama viešame gynimo tarybos posėdyje 2022 m. rugsėjo mėn. 02 d. 10 val. FTMC Fizikos instituto saleje ir nuotoliniu būdu.
Adresas: Savanoriu pr. 231, LT-02300 Vilnius, Lietuva
Tel. +370 5 264 8884; el. paštas: office@ftmc.lt

Disertaciją galima peržiūrėti Fizinių ir technologijos centro, Vilniaus universiteto bibliotekose ir VU interneto svetainėje adresu: https://www.vu.lt/naujienos/ivykiu-kalendorius

CONTENTS

ACKNOWLEDGEMENTS

During the writing of this dissertation, I have received a great deal of assistance and support. First, I would like to thank Center for Physical Sciences and Technology, its director prof. habil. dr. Gintaras Valušis, head of Material Science as well as Department of Laser Technologies, its director dr. Gediminas Račiukaitis for all the support and encouragement.

I am sincerely grateful to my supervisor dr. Raimondas Petruškevičius for his sharing of knowledge and theoretical expertise, guidance, suggestions, encouragement, fruitful discussions and all the support.

I would also like to thank Ramūnas Valiokas, Tomas Rakickas, Regimantas Januskevičius, Valerijus Smilgevičius, Rytis Butkus, Skirmantas Ališauskas, Darius Kezys and Saulius Juodkazis for great discussions and work together.

I am grateful to Edgaras Markauskas, Konstantinas Vaškevičius, Armandas Balčytis and Martynas Gabalis and other colleagues from Center of Physical Sciences and Technology for advice, support and joyful working environment.

In addition, I would like to thank my parents and wife Akvile for continuous support and love.

NOTATIONS AND ABBREVIATIONS

Main notations

B - magnetic induction field
β - beta wave vector
c - speed of light
D - electric field displacement
d_{wr} - distance from waveguide to the ring
E - electric field
h - height
H - magnetic field
J - electric charge current density
k - coupling constant
l_{cavity} - cavity length
$L_{round\ trip}$ - roundtrip length
m - mode order
n - *refractive index*
n_{eff} - effective refractive index
n_g - group index
R - reflectivity
R_{TE}, R_{TM} - Fresnel reflection coefficients
r - radius
S - sensitivity
t - time
w - width
ϵ - dielectric permittivity
θ - incidence angle
Λ - period
λ - wavelength
μ - permeability
ρ - charge density
$\Delta\lambda$ - wavelength shift
Δn - refractive index change
Δx - step size in x
Δy - step size in y
Δz - step size in z
$\Delta\nu$ - width of FSR
ω - frequency

Abbreviations

Cases

INTRODUCTION

Optical biosensors, which provide detection and quantification of bio analytes, have emerged as a field of great interest because of the tremendous needs in early-stage disease diagnosis, pharmaceuticals, security, food quality control and environmental testing [1] as well as currently vital virus detection [2]. The optical biosensor is a compact device that contains biometric sensing elements integrated with an optical transducer system. The purpose of the optical biosensor is to generate a signal proportional to the concentration of the substance (analyte) being measured. Optical biosensors can use a variety of biological materials as biological recognition elements, including enzymes, antibodies, antigens, receptors, nucleic acids, tissues, and whole cells. Surface plasmon resonance (SPR), integrated resonators, gratings, refractometers, evanescent wave fluorescence, and optical waveguide interferometry use the evanescent field near the surface of the biosensor to detect the interaction of the biometric element with the analyte. Among the various optical bio sensing devices, effective refractive index sensors have appeared as a promising technology in the last few years. With these devices, the average refractive index change associated with binding of the sensing object is monitored [3]. Refractive index sensors allow label-free, real time and direct detection of the molecular interaction at a dielectric interface.

Although there are many different refractive index sensors [4], high quality factor optical sensors based on multiple-photon-passage microstructures constitute one of the most sensitive and promising class of label-free sensors. The quality factor of a given device is a measure of the photon lifetime within the structure. Larger quality factor means longer lifetime. The major advantages of the high-quality factor include the multiple-pass interaction of propagating electromagnetic radiation with the respective analyte within the vicinity of an optical device and narrow resonance linewidth, allowing resolving small resonance wavelength shifts due to the small change of the refractive index induced by the analytes.

Among the high quality factor optical sensors, due to their practicality optical microring resonators have become a topic of great interest for devising wavelength selective filters [5, 6], switches [7], modulators [8], low-threshold semiconductor lasers [9, 10] as well as for sensing applications in early-stage disease diagnosis, security, and environmental monitoring [3, 5, 11, 12], where high-sensitivity label-free sensors based on optical resonators are among the most promising in the field [13]. They

provide low insertion loss, single transversal mode operation and small size (~ 3 μm, low footprint).

The simplest microring resonator consists of a bus waveguide and ring structure (all pass resonator [14]). The optical mode from a bus waveguide couples into the microring through the evanescent field. The wave, after propagating a full round trip and gaining some phase, couples back to the bus waveguide and interferes with the transmitted wave. At resonance, the phase gain is such that the waves destructively interfere [15]. Sensory properties of such resonators emerge from the mode field interaction with the surrounding medium. The change in refractive index of a surrounding medium induces change in the propagation constant of the mode, which then causes the change in resonance conditions. This effect can be observed by monitoring the shift in the resonance wavelength position [16].

Studied microring resonator sensors are based on silicon-on-insulator microring resonators [16, 17]. The state-of-the-art silicon-on-insulator platform represents a cornerstone of contemporary telecommunications photonics and is among the most popular technologies for optical sensors. It is attractive due to its compatibility with the well-established complementary metal oxide semiconductor process as well as a high refractive index contrast that enables strong mode field confinement and small waveguide bending radii [5].

However, the high mode field confinement produces a disadvantage in sensing applications due to the relatively small overlap between cladding material and mode evanescent field. The exceptionally rapid decay of the evanescent field around Si waveguide elements, estimated to decrease by a factor of 1/e at a distance of 63 nm [18], is useful for surface bio-sensing of water-borne analytes, as it allows higher specificity due to the signal being dominated by contributions from the functionalized surface layer. In this field functionalization is often achieved by applying various cladding materials, such as spray-coating triphenylene-ketal receptor for TNT detection [19], drop-casting ZnO nanoparticles for ethanol sensing [20], or dip-coating Pt-doped tungsten oxide in a sol-gel solution for H_2 detection via catalytic combustion [21-23], deposited at thickness values ranging from 150 nm to multiple micrometers.

However, strong confinement is detrimental when bulk sensitivity is required such as in gas sensing. It is possible to increase the bulk sensitivity by utilizing the Vernier effect [24, 25]. The latter requires using a system of two or more rings with slightly different radii, and the radius of each ring must be relatively large (on the order of several tens of microns), such that

the free spectral range would be quite small. Several other strategies have been proposed to overcome this limitation, including ultra-thin SOI microring resonators [26], slotted waveguide microring resonators [13, 27, 28], by adding a polymer layer at the resonator surface [29], introduction of subwavelength grating structures [30-32] and photonic crystals inside the microring cavity [**Error! Reference source not found.**, 33-37], and a microring with periodically arranged metal nanodisks [P2, 38]. Another way to enhance the light in the cladding material is via the introduction of average refractive index modulation. Several microring geometries based on this strategy have been reported: the slotted microring resonator [39, 40, 41] (sensitivity up to 350 nm/RIU), and the SNOW microring resonator [42] (theoretical sensitivity up to 350nm/RIU).

Another problem arising from high refractive index contrast, especially for relatively large radius microring resonators, is the free spectral range (spectral spacing between nearby resonances), which imposes a limit on the measurable extent of variations in analyte concentration. A resonance wavelength shift that exceeds the free spectral range becomes indistinguishable from a nearby resonance. Hence, to increase the measurement range it has been suggested to employ nearby mode suppression [35, P2] and to use microring resonators with embedded asymmetric Mach–Zehnder interferometers [43].

This doctoral thesis is dedicated to address low bulk sensitivity and poor referencing capabilities of microring resonators. To overcome the latter various microring resonator geometries and concepts are investigated to increase the light and matter interactions. In this work numerical simulations of novel microring resonator geometries, based on modulation of the effective refractive index in the core material are presented. Here, subwavelength hollow core defects are introduced inside the core material to increase the surface area of the resonator and the light–matter interaction. In addition, to address devices where resonance shifts are too large to observe and absorbing materials are used, novel microring resonators with no free spectral range as well as resonators working with highly absorbing materials such as metals are shown. Finally, to simplify the detection mechanism, self-referencing sensors are processed and shown.

OBJECTIVES

The objectives of this doctoral thesis were to explore and develop novel optical microring sensors with different approaches such as introduction of

effective refractive index modulation, 1D Bragg gratings and absorbing metal nanostructures. The main contribution of this thesis was the demonstration of bulk sensitivity control using lossy perforations as well as realization of self-referencing optical microring resonators. In particular, the focus was put on the investigation of:

- integrated optical microring sensors having introduced fully etched subwavelength perforations in the core to increase the light-matter interaction. In addition, to show that the bulk sensitivity of perforated microring resonators can be enhanced;

- a sensor which has a limited free spectral range, meaning that if the shift of the resonances is higher than the free spectral range, the detection becomes impossible. The study on an optical silicon-on-insulator microring resonator patterned with periodically arranged set of gold nanodisks, which could remove the longitudinal multi-mode behavior;

- processing and analysis of a fabricated microring resonator with an integrated one-dimensional photonic crystal. In addition, investigation of microring resonator with Bragg grating which operates in both air and dielectric photonic bands to understand how the resonances on both edges of the bandgap contribute to the sensitivity of microring resonators;

- 3D perforations which might have enhanced sensitivity and measurement range. Focus was put on partially etched rectangular perforations;

- specifically tailored gratings, which are placed on the inner side wall of the microring resonator. Moreover, the development of a self-referenced sensor that is immune to the changes in ambient temperature.

TASKS TO ACHIEVE THE OBJECTIVES:

- to set up an optical characterization lab and setup, which can measure integrated optical devices. This includes identification and acquisition of suitable optical equipment;

- to design an integrated optical circuit with all the coupling elements such as grating couplers, optical waveguides, mode converters and microring resonators;

- to design all the integrated optical elements, which adhere to processing requirements infringed by the global foundries;

- to design all the integrated optical elements, which are compatible with several step electron beam lithography;

- to design grating couplers, which operate in the right frequency range of the microring resonators;

- to design and simulate optical microring resonators, which are coupled to the bus waveguides;

- to design and simulate microring resonators with 1D perforations for enhanced bulk sensitivity;

- to design and simulate microring resonators with gold nanodisks for self-referencing and more sensitive surface and bulk refraction index sensing;

- to perform processing of the microring resonators using state-of-the-art cleanroom facilities;

- to design, simulate and process microring resonators with integrated 3D perforations;

- to design, simulate and process microring resonators with integrated gratings on the inner side wall and demonstrate the self-referencing capabilities;

- to conduct optical measurements of all the different devices, which were designed for specific experiments.

SCIENTIFIC NOVELTY AND PRATICAL VALUE

The experimental optical studies performed in the present doctoral thesis are in a field of an emerging technology of integrated optical biological and gas sensing applications.

The main novelty of this study lies in a demonstration of an optical microring resonator structure with low dielectric constant material defects for enhanced optical sensing. It is shown that proposed refractive index sensor based on a microring resonator outperforms ordinary microring resonators. The perforated microring resonator enables variation of the quality factor and the sensitivity, making it applicable in many optical areas. It is possible not only to achieve high sensitivity, which is deduced from resonance wavelength shifts due to the small change of the effective refractive index induced by the analytes, but also to increase the total area of the interface between the microring resonator and the surrounding medium, which increases the light–matter interaction with aqueous media and gases.

It has been shown that implementation of gold nanodisk arrays on a microring resonator creates a novel ultra-wide free spectral range sensor platform. The latter stems from filtering of the unsupported or highly absorbed modes. The only limiting factor is the bandwidth of the waveguide, which is defined by the geometry and material of the waveguide. A 2-fold improvement over the unmodified analogue is demonstrated.

The practical realization of the sensor with one-dimensional photonic crystal, formed by partially etched cylindrical perforations, was studied. It is shown that the field of higher mode localizes inside the holes of photonic crystal, the air band, and has higher bulk refractive index sensitivity.

It has been demonstrated that a microring resonator with an integrated 1D photonic crystal having a 3D geometry has enhanced sensitivity and measurement range. The partial perforation-induced photonic bandgap can be used as a spectral reference to overcome limitations imposed by the FSR. Moreover, the limit of detection can be minimized, depending on considerations of the leading factor determining sensor resolution.

To complement the studies of the microring resonator with gold nanodisks, microrings with dielectric 2nd order grating were implemented. The latter have enhanced quality factors and sensitivity to external cladding environment. These loss-modified microring resonators with second order Bragg grating filter out photonic non-matching modes of a silicon on insulator microring, enhance sensitivity and free spectral range of the sensor

(like gold nanodisks), which is useful for development of self-referenced bio and gas sensors.

This work is valuable for devices, which rely on the light-matter interactions. For example, optical sensors, which need to detect small amount of material, require strong light-matter interactions. Introduction of proposed perforations increases the electromagnetic field overlap with the surrounding medium in turn increasing the sensitivity to the smaller density of material inside the surrounding medium.

Proposed self-referencing devices allow large ring resonators to be used as sensors. The increase of ring resonator radius reduces the free spectral range (could easily be below 1 nm). The latter implies that the position of the ring resonators resonances changes by more than the free spectral range of the ring resonator and makes the tracking of the resonance shifts ambiguous. The self-referencing mechanism eliminates this drawback and allows to use ring resonators spanning over large area. This is particularly useful for gas sensors, which need to detect low density materials.

SCIENTIFIC STATEMENTS

- The integrated microring resonators with perforated 1D dimensional defects enhance the electromagnetic field interaction with surrounding material and outperform regular microring resonators while preserving high quality factor. Moreover, different air and dielectric modes supported by the 1D periodic structure allow to trap the electromagnetic field maxima in the low dielectric material increasing the light-matter interaction.

- The introduced metal nanodisks grating on top of microring resonator or 2^{nd} order Bragg grating on the inner side wall of the microring resonator filter the unsupported longitudinal and transversal modes and enable single mode operations.

- The modified integrated microring resonators have specific optical responses. i.e. single mode operation or bandgaps, which can be used for self-referencing devices.

STRUCTURE OF THE DISSERTATION

Chapter 1 presents the literature survey of light guiding on a chip, which includes total internal reflection and effective index guiding, optical micro resonators and microring resonators as well as principal of integrated photonic sensors.

Chapter 2 defines methods and materials used. Finite-difference time-domain as well as definite-frequency eigenstate simulations are described. In addition, sample fabrication, which includes top-down processing (consisting of electron beam lithography, ultraviolet lithography and etching), is presented. Finally, in this chapter experimental setup used is explained.

Chapter 3 presents main results, discussions and conclusions.

AUTHOR CONTRIBUTION

The author of the dissertation performed design, simulations, fabrication, experiments of the devices as well as participated in the analysis of the results, data presentation, manuscript preparation and reviewing process. Also, took a great part in setting up of the nanophotonics laboratory at the Center for Physical Sciences and Technology as well as suggested most of the ideas for the presented results.

In 3.1, 3.2 the author came up with the idea, designed and simulated as well as characterized the devices. In 3.3 the author designed, simulated, and fabricated the devices. In 3.4 the author supervised the work and performed analysis of the results. In 3.5 the author came up with the idea, designed and simulated the devices.

LIST OF PUBLICATIONS

Publications pertaining to the thesis:

P1. M. Gabalis, **D. Urbonas**, R Petruskevicius, ”A perforated microring resonator for optical sensing applications,” *J. Opt.* 16 (10), 105003 (2014).

P2. **D. Urbonas**, A. Balčytis, M. Gabalis, K.Vaškevičius, G. Naujokaitė, S. Juodkazis, R. Petruškevicius, ”Ultra-wide free spectral range, enhanced sensitivity and removed mode splitting SOI optical ring resonator with dispersive metal nanodisks,” *Opt. Lett.* 40 (13), 2977-2980 (2015).

P3. **D. Urbonas**, A. Balčytis, K. Vaškevičius, M. Gabalis, R. Petruškevičius, ”Air and dielectric bands photonic crystal microringresonator for refractive index sensing,” *Opt. Lett.* 41 (15), 3655-3658 (2016).

P4. K. Vaškevičius, M. Gabalis**, D. Urbonas**, A. Balčytis, R. Petruškevičius, ”Enhanced sensitivity and measurement range SOI microring resonator with integrated one-dimensional photonic crystal,” *JOSA B* 34 (4), 750-755 (2017).

P5. R. Petruškevičius, A. Balčytis, **D. Urbonas** , K. Vaškevičius , S. Juodkazis, „Microring resonators with circular element inner-wall gratings for enhanced sensing“, *JJAP*, 59, SOOD02-1-7 (2020).

OTHER PUBLICATIONS

P6. D. Urbonas, M. Gabalis and R. Petruškevičius, ”Numerical Simulation of Microring Resonator Biosensor with FDTD Algorithms Based on GPU B-CALM and CPU Meep,” *Opt. Quantum Electron.* 46 (8), 1021-1026 (2014).

P7. T. Tamulevičius, I. Gražulevičiūtė, D. Urbonas, M. Gabalis, R. Petruškevičius, S. Tamulevičius, ”Numerical and experimental analysis of optical responds of sub-wavelength period structure in carbonaceous film for refractive index sensing,” *Opt. Express* 22(22), 27462-27475 (2014).

P8. A. Balčytis, D. Hakobyan, M. Gabalis, A. Žukauskas, D. Urbonas, M. Malinauskas, R. Petruškevičius, E. Brasselet, S. Juodkazis,

”Hybrid curved nano-structured micro-optical elements,” *Opt. expres*s 24 (15), 16988-16998 (2018).

INTERNATIONAL CONFERENCES

C1. **D. Urbonas**, M. Gabalis, S. Malaguti, A. Parini, G. Bellanca, R. Petruskevicius, ”Modeling of microring resonators with high dispersion induced by a one dimensional photonic crystal,” in Abstr. XXII Intern. Workshop on Optical Wave & Waveguide Theory and Numerical Modelling (OWTNM 2014), 27-28 June, 2014, Nice, France, 40p. (oral).

C2. **D. Urbonas**, M. Gabalis, R. Petruskevicius, ”Numerical Simulation of resonance structures with FDTD Algorithms Based on GPU B-CALM and CPU Meep,” in Abstr. XXII Intern. Workshop on Optical Wave & Waveguide Theory and Numerical Modelling (OWTNM 2014), 27-28 June, 2014, Nice, France, 46p. (poster).

C3**. D. Urbonas**, M. Gabalis, K. Vaskevicius, A. Balcytis, R. Petruskevicius, ”Hybrid Plasmonic Modes in Gold Nanocup Sensors,” in Abstr. COST MP1205 General Meeting, 24-25 April, 2014, Dublin, Ireland, 31pp. (poster).

C4. **A. Balcytis**, G. Seniutinas, D. Urbonas, M. Gabalis, K. Vaskevicius. R. Petruskevicius, G. Molis, G. Valusis, S. Juodkazis, "High precision fabrication of antennas and sensors", SPIE Proc. **9446**, 9th Inter. Symp. on Precision Engineering Measurements and Instrumentation , 94461G (March 6, 2015).

C5. **R. Petruškevičius**, A. Balčytis, D. Urbonas , K. Vaškevičius , S. Juodkazis, "Perforated Micro-Ring Resonators for Enhanced Sensing", IEEE Proc. in International. Conference "24th Microoptics Conference (MOC2019)", November 17-20, 2019, Toyama, Japan, 2p.

LOCAL CONFERENCES

C6. **D. Urbonas**, A. Balcytis, M. Gabalis, K. Vaškevičius, G. Naujokaitė, S. Juodkazis, R. Petruškevicius, ”Ultra-wide free spectral range, enhanced sensitivity and removed mode splitting SOI optical ring resonator with

dispersive nanodisks," in Abstr. 41th Lithuanian National Conference on Physics, June 17-19, 2015, Vilnius, Lithuania (oral).

1. FUNDAMENTALS

1.1 Guiding of light and an integrated optical waveguide

Guiding of light is one of the essentials ways to steer the light and is mainly used in optical fibers and integrated optics. Main principal of light guiding relies on total internal reflection (TIR) (TIR, section 1.1.1) and effective index guiding (section 1.1.2) [44]. In this thesis integrated optical waveguides were used (***Figure 1***). Optical waveguide consists of a high refractive index core (indicated in cyan color), which confines the light, low refractive index (compared to the core) substrate (grey color) and low refractive index (compared to the core) cladding. Depending on the dimensions of the waveguide either TIR or effective index dominates.

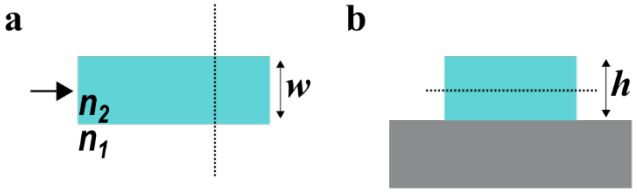

Figure 1. Optical waveguide. a, Top view of an optical waveguide. **b**, Cross section of an optical waveguide. Dashed line indicates the cross section shown in **b** and **a**, n_1 and n_2 depict refractive indexes of low and high refractive materials (cyan color) respectively, grey — substrate layer (also named as box layer, where SiO_2 is used). w — width of the waveguide and h — height of the waveguide and arrow in **a** shows the mode propagation directions.

1.1.1 Total internal reflection

TIR is an optical phenomenon which occurs when light is incident from a high refractive index material to a low refractive index medium (**Figure 2**). At the interface of two materials the light refracts, if the incidence angle θ_1 is higher than the critical angle, the TIR takes place. The critical angle is met if the angle of refraction $\theta_2 = 90°$. From Snell's law it can be expressed as:

$$\theta_1 = arcsin\left(\frac{n_1}{n_2}\right) \quad (1)$$

Since $n_1 < n_2$, equation will always produce imaginary values. This means that no light can be transmitted, and it is completely reflected. The latter can be understood from Huygens's principal, which states that every point on a wave front is itself the source of spherical wavelets, and the secondary wavelets emanating from different points mutually interfere. The

sum of these spherical wavelets forms the wavefront. If the critical angle is met, at the interface of high and low refractive index materials the wavelets build up a phase difference leading to a destructive interface for the refracted (transmitted light) and a constructive interference condition for the reflected light. Additionally, as the light has both particle and wave propagation features, the light from the wavelets extends into the low refractive index material leading to a light penetration into the low refractive index region (**Figure 3**). This penetration depth, which is on the order of few wavelengths, is typically called the evanescent field.

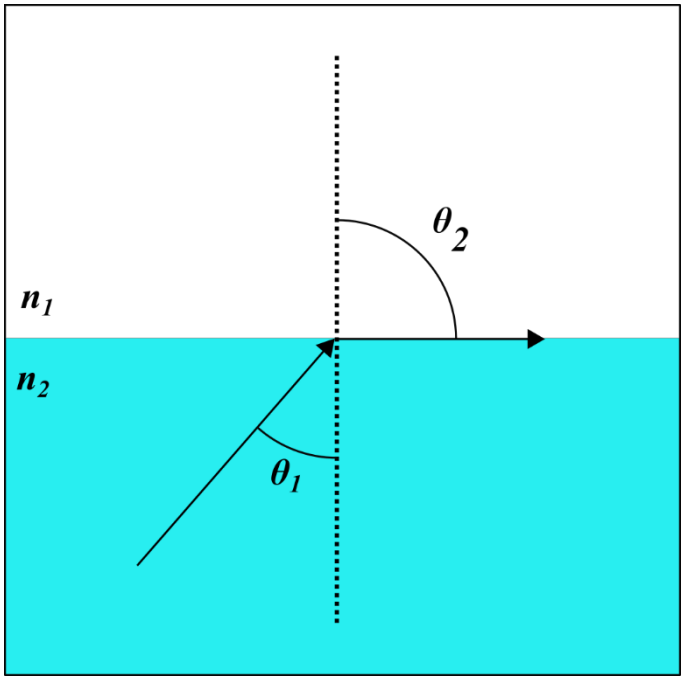

Figure 2. TIR. TIR at the interface of two dielectrics. Θ_1 — angle of refraction incidence, Θ_2 — angle of refraction. Dashed line depicts the normal to the interface of two dielectrics, arrows indicate the propagation of light.

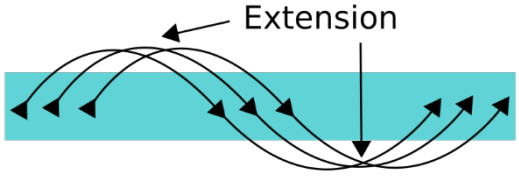

Figure 3. Electromagnetic field propagation inside optical waveguide. Sketch indicates top view of an optical waveguide with electromagnetic field (indicated by wavy black lines) propagating inside the optical waveguide. Black arrows depict electromagnetic extension into surrounding cladding medium.

The reflection intensity for transverse electric (TE) and magnetic (TM) polarizations can be described by Fresnel equations [45]:

$$R_{TE} = \left| \frac{n_2 \cos\theta_1 - n_1 \sqrt{1 - \left(\frac{n_2}{n_1}\sin\theta_1\right)^2}}{n_2 \cos\theta_1 + n_1 \sqrt{1 - \left(\frac{n_2}{n_1}\sin\theta_1\right)^2}} \right|^2 \quad (2)$$

$$R_{TM} = \left| \frac{n_2 \sqrt{1 - \left(\frac{n_2}{n_1}sin\theta_1\right)^2} - n_1 \cos\theta_1}{n_2 \sqrt{1 - \left(\frac{n_2}{n_1}sin\theta_1\right)^2} + n_1 \cos\theta_1} \right|^2 \quad (3)$$

Equations are plotted in **Figure 4**. As the angle incidence increases the reflection goes up and at a critical angle reaches unity reflection. Here $n_1 = 1$ and $n_2 = 1.33$ were used.

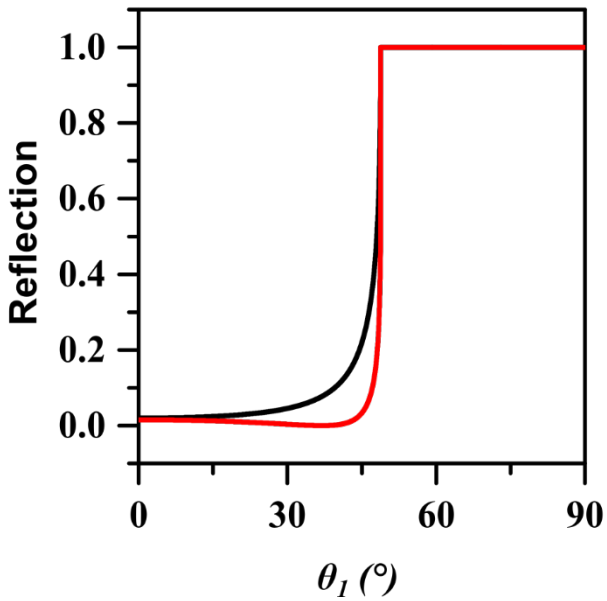

Figure 4. Fresnel reflection. Angle dependent reflection from the interface of two dielectrics when light is incident from high refractive index material side (Figure **2**). Red color denotes TM polarization and black — TE.

Optical waveguides having dimensions, which are higher than few wavelengths of the guided mode, operate in TIR regime. To ensure that, cladding and substrate both have refractive indexes lower than core's. In this case the optical mode is tightly confined inside the core and little light leaks out of the waveguide. If the dimensions of the waveguide reach wavelength of the propagating light, the waveguide enters effective index guiding regime.

1.1.2 Effective index

The wavenumber (phase change per unit length) for plane waves in the homogeneous media is defined by the refractive index. The wavenumber is n times larger than it would be in vacuum. The effective refractive index ($n_{eff.}$ has the analogous meaning for light propagation in a waveguide with restricted transversal dimension. The $n_{eff.}$ is dependent not only on the wavelength but also on the guided mode, whose shape is highly influenced by the geometry of the waveguide.

As an example, we can look at an optical waveguide consisting of periodic blocks (**Figure 5**). Despite waveguide being chopped, the light propagates with record low losses [46]. This is because the period Λ and duty cycle η (defines the thickness of the blocks) are set such that the deformations are much smaller than the wavelength. In other words, wave function of the mode extends over these blocks leading to a specific shape of the mode and $n_{eff.}$. With the decrease of the waveguide width or thickness, the $n_{eff.}$ decreases till the mode completely leaks out into the surrounding media. The lower the $n_{eff.}$, the more the mode leaks out into the surrounding media. This effect enables optical sensing (section 1.3).

Figure 5. Effective index waveguide. Λ depicts period of high refractive index blocks. Arrow shows the mode propagation directions.

1.2 Optical micro resonators

In this work integrated 1D (1 dimensional) and 2D (two dimensional) integrated optical micro resonators were used. To understand the operation

of the 1D resonator we first look at a more common 1D vertical cavities. The key element of the latter is the distributed Bragg reflectors (DBR) [47]. They are composed out of alternating high and low refractive index layers forming a stack defined by total number of DBR pairs (**Figure 6**). The principal of DBRs rely on interference. As the incident light goes through the material it picks up phase. When it reaches the interface, it gets partially reflected. If the incident light is in phase with partially reflected light a constructive interference condition is reached at the reflection side and destructive interference is achieved on the transmission side. The thicknesses for the different layers can be expressed as:

$$h_{n_{low}} = \frac{\lambda}{4n_{low}} \tag{4}$$

$$h_{n_{high}} = \frac{\lambda}{4n_{high}} \tag{5}$$

here n_{low} and n_{high} are wavelength dependent high and low refractive indexes and λ is the center wavelength of the DBR.

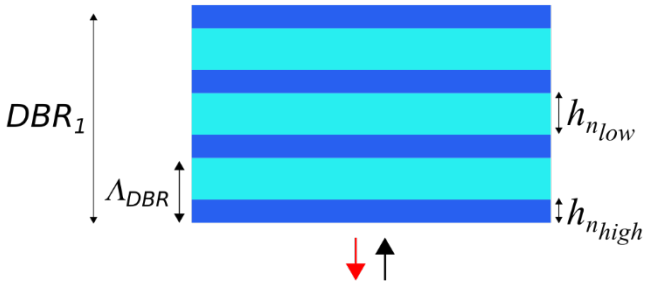

Figure 6. 3.5-layer DBR. An optical reflector composed of high (dark blue) and low (cyan) refractive index layers. Here Λ_{DBR} depicts the total thickness of a single DBR layer, $h_{n_{high}}$ — thickness of high refractive index material, $h_{n_{low}}$ — thickness of low refractive index material and DBR_1 — total DBR. Red and black arrows indicate reflected and incident light, respectively.

The higher the number of layers, the higher the reflection from the DBR (**Figure 7**). As the light is partially reflected at every interface, increasing the number helps to increase the reflectivity and the width of the reflection stopband. However, increasing number of DBRs leads to extension of electromagnetic field into the DBR which could result in losses if the DBRs are not perfect.

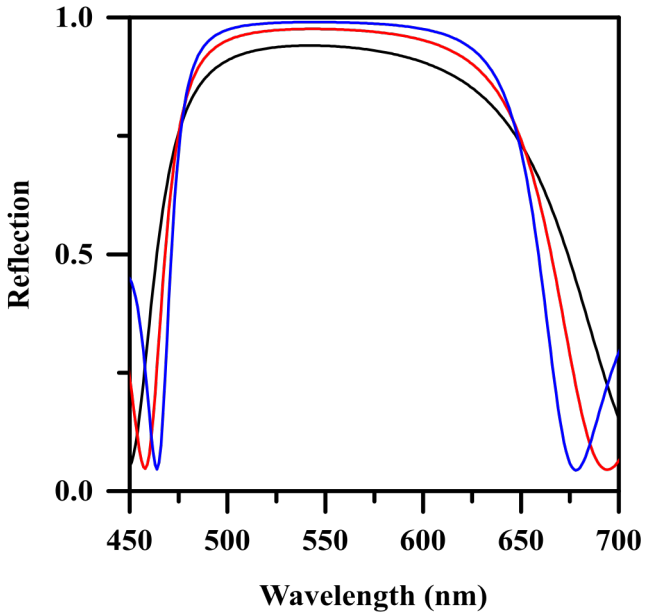

Figure 7. Reflection from a DBR. Black, red, and blue lines show reflection from 3.5, 5.5 and 7.5 DBR layers respectively.

To create an optical cavity two DBRs are brought in front of each other with a spacer in between (**Figure 8**). The thickness of the spacer can be expressed as:

$$h_{n_{cavity}} = \frac{\lambda m}{2n_{cavity}} \tag{6}$$

here n_{cavity} is the refractive of the center spacer (cavity defect layer) and m is the order of the longitudinal mode. The $h_{n_{cavity}}$ is set such that a standing wave phase condition is reached (equal number of half wavelengths).

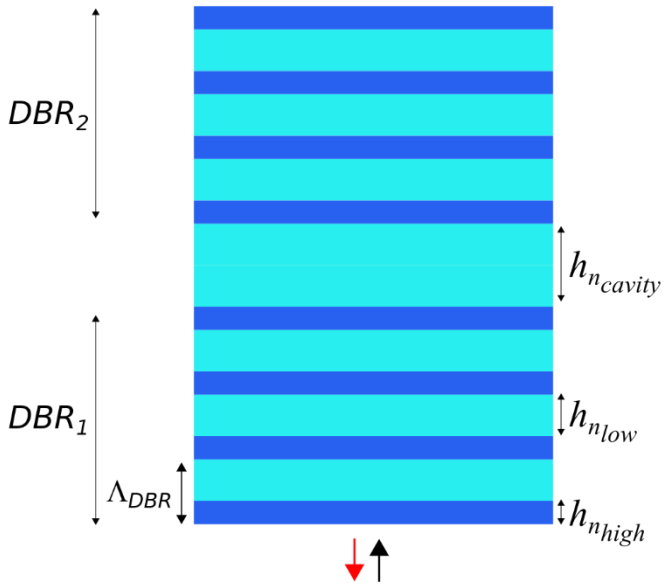

Figure 8. Vertical DBR cavity. Schematic of 1D vertical cavity consisting of DBR_1 and DBR_2 and centre cavity defect having thickness $h_{n_{cavity}}$.

The higher number of DBRs, the higher the quality factor Q:

$$Q = \frac{\lambda}{\Delta\lambda} \tag{7}$$

here $\Delta\lambda$ denotes the full-width half-maximum (FWHM) of the Lorentzian shape resonances (**Figure 9**). Quality factor defines how long the photon lives inside an optical cavity. The higher the Q factor, the higher the electromagnetic field confinement and the higher intensity is reached inside the optical cavity. Lorentzian shape comes from the decay of photons in time. Due to the exponential decay out of the cavity the shape in energy (wavelength) is Lorentzian.

Another important factor that characterizes the optical resonator is the modal volume V. Modal volume defines how strong is the electromagnetic field confinement inside the cavity and can be expressed as:

$$\mathrm{V} = \frac{\int \varepsilon \mathrm{E}^2 \mathrm{dV}}{\max\left(\varepsilon \mathrm{E}^2\right)} \tag{8}$$

here E depicts the electromagnetic field and ε — dielectric permittivity. High modal volume means that electromagnetic field is strongly localized in the

specific spot. This, however, does not work properly for cavities which have multiple electromagnetic field maxima.

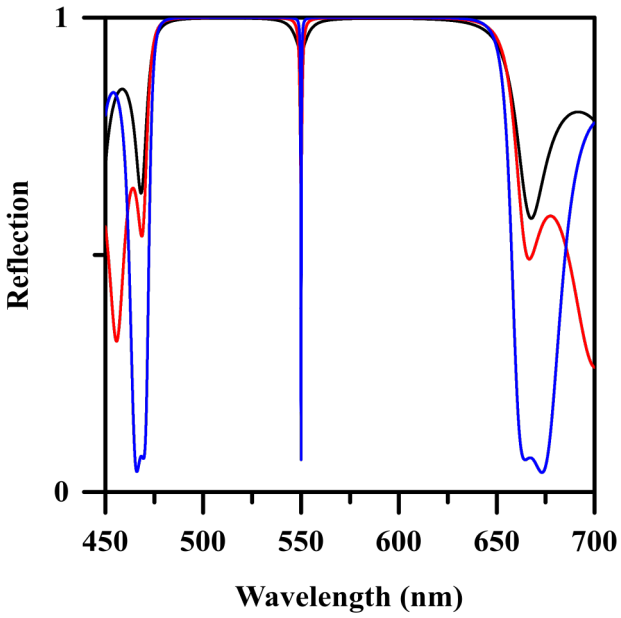

Figure 9. Reflection from 1D cavity. Reflectivity from vertical cavity consisting of two DBRs and a center defect. Black, red and blue peaks at 550 nm show resonances of 1D optical cavities having 3.5, 5.5 and 7.5 DBR layers on both sides of the center defect respectively. $h_{n_{cavity}}$ is set to match 550 nm central wavelength.

In **Figure 10** we can see a zoom in of the **Figure 9** which shows how the quality factor of the resonances depend on the number of DBR layers. As the number of DBR layers increases, the quality factor goes up but the central wavelength stays the same. In **Figure 11** quality factor is plotted versus the number of DBR layers. The quality factor will not increase till infinity, at some point the penetration into the DBR becomes so small that the increasing number of the layers does not have any effect.

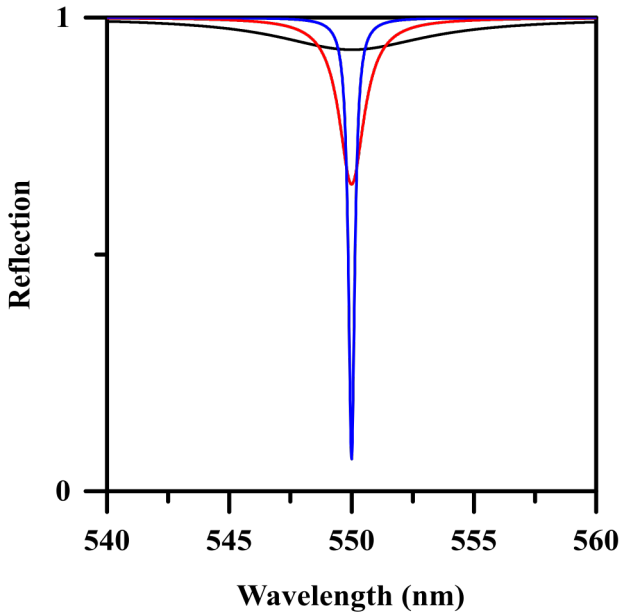

Figure 10. Cavity modes. Zoom in of resonances in **Fig. Figure 9**.

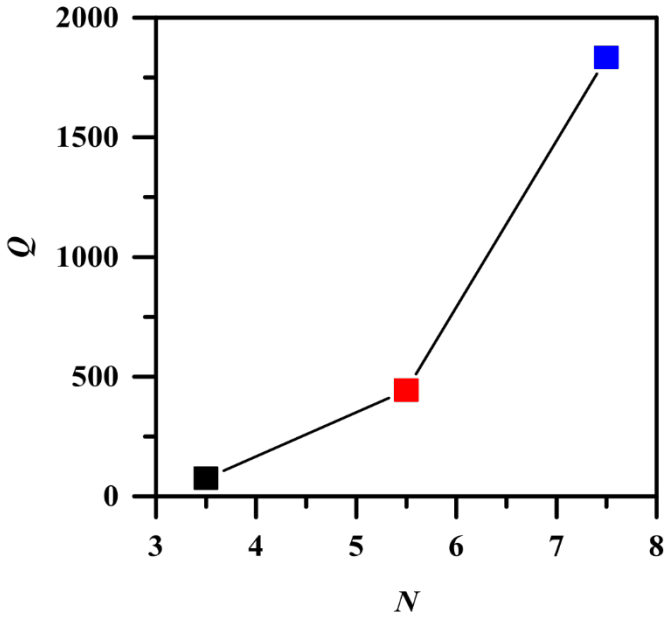

Figure 11. Quality factor dependence on number of DBRs. Black, red and blue points represent quality factor of 1D optical cavities having 3.5, 5.5 and 7.5 DBR layers on both sides of the center defect respectively.

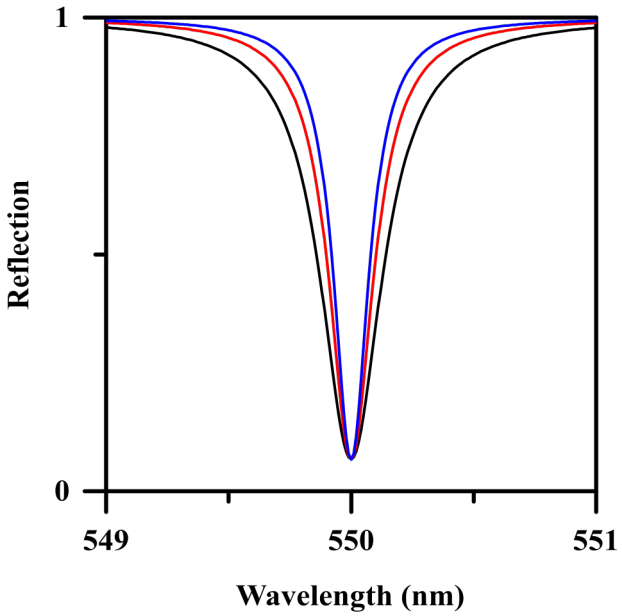

Figure 12. Reflection dependence on cavity length. Black, red and blue colored lines denote optical modes of 1D optical cavities having $h_{n_{cavity}}$, $2h_{n_{cavity}}$ and $3h_{n_{cavity}}$ center defect length, respectively.

With the increase of cavity center defect length, the quality factor (**Figure 12** and **Figure 13**) as well as the number longitudinal modes goes up. The longer the cavity defect, the more longitudinal modes meet the standing wave phase condition.

One more important factor that defines optical cavities is the phase of the reflected light. It depends on the light field coupling to the cavity modes. The coupling condition can be changed with the number of DBRs on the reflection side. If the number of DBR is low, the cavity is in the over coupled regime. In this case the internal cavity losses are much lower than coupling to the outside continuum of modes. In this case the reflected resonance has a phase change of 2π ranging across the resonance (**Figure 14**, blue line). If the coupling to the cavity is equal to the internal cavity loss, the cavity is in critical coupling condition and highest quality factor is achieved. If the coupling to the outside continuum of modes is lower than the internal cavity loss, the cavity is in over coupled regime. In this case less light is coupled into the cavity compared to the previous cases. The latter allows to control the in coupling of light into the optical microcavities.

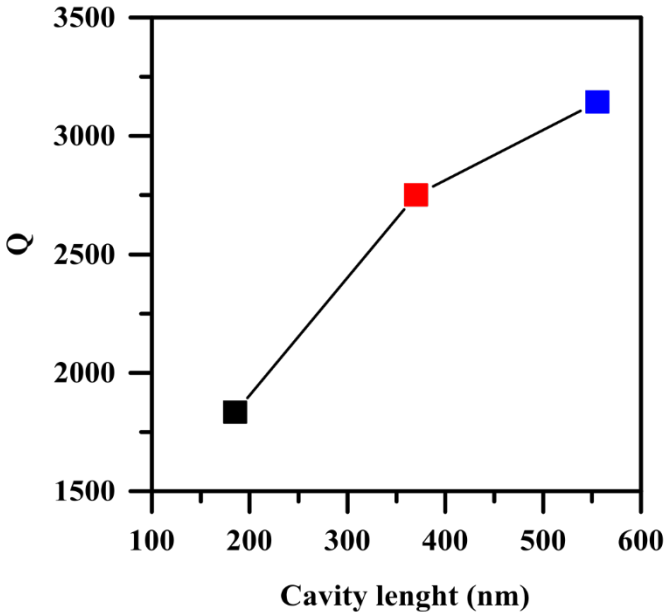

Figure 13. Quality factor dependence on cavity length. Black, red and blue colored points denote optical modes of 1D optical cavities having $h_{n_{cavity}}$, $2h_{n_{cavity}}$ and $3h_{n_{cavity}}$ center defect length, respectively.

In previous examples center cavity length was set to have lengths where $m = 1, 2, 3$. If we set the cavity length such that for two modes having $m = 2, 3$ have their resonance condition fulfilled, multiple modes can be seen inside the spectrum (**Figure 15**). Multiple resonance peaks here are different longitudinal modes. The distance between those modes can be controlled with the length of the defect. The longer the defect, the higher the number of longitudinal modes and the lower the spacing between them. The spacing is called Free Spectral Range (FSR) and can be expressed as:

$$\Delta\upsilon = \frac{c}{2n_g h} \tag{9}$$

where c is speed of light, h is the cavity thickness and n_g is the group index (group refractive index).

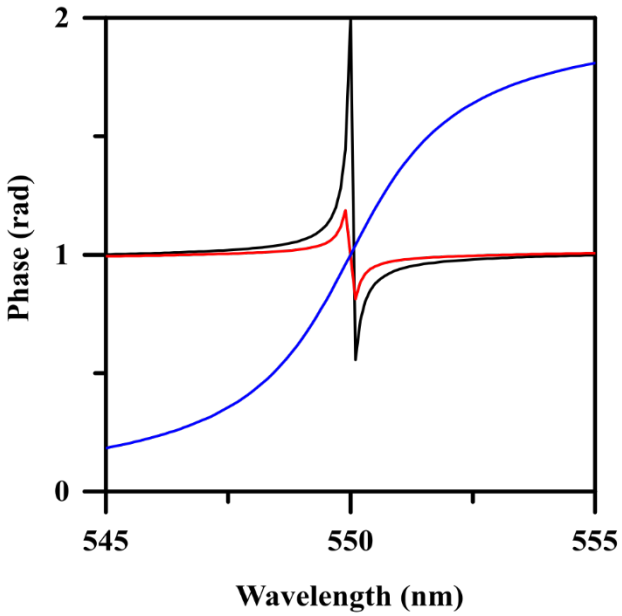

Figure 14. Phase of light reflected from 1D optical cavity. Black, red and blue colored lines depict optical cavities having 3.5, 6.5 and 7.5 number DBR_1 layers.

In the integrated optics case optical 1D cavity is planar (**Figure 16**). Here an optical waveguide is perforated with some holes, which form a periodic structure operating as the DBRs in 1D vertical case. The main difference is the change in modal confinement. In 1D vertical case the mode is not confined laterally. Here due to introduced lateral confinement the mode and the refractive index change. The resonance condition can be written as:

$$l_{cavity} = \frac{\lambda m}{2n_{eff.}} \tag{10}$$

$n_{eff.}$ is now influenced not only by the geometry but also by the surrounding media. This effect is used for optical sensors (section 1.3).

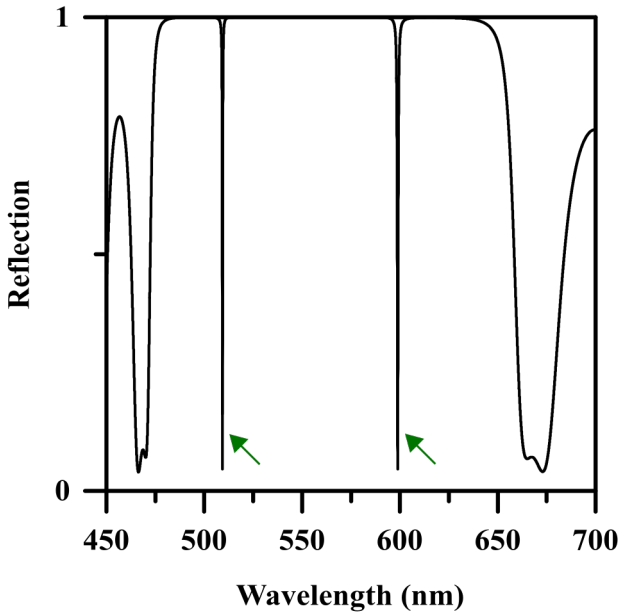

Figure 15. Reflection from the cavity having resonances of $\mathbf{m = 2, 3}$. Green arrows indicate the resonance peaks showing multiple longitudinal modes supported by 1D optical cavity.

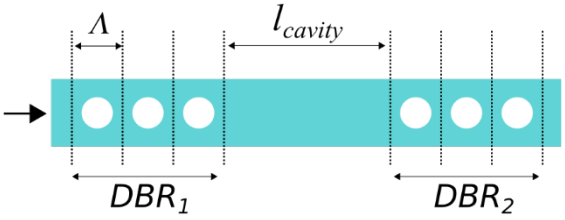

Figure 16. Integrated photonic 1D cavity. Top view of an integrated 1D optical cavity. Here Λ indicates the period of the 1D DBR, l_{cavity} depicts the center cavity length. which is equivalent to $h_{n_{cavity_{eff.}}}$ having $n_{cavity_{eff.}}$.White holes depict the (section 2.2.4) holes etched into the optical waveguide (Fig. Figure ***1***).

1.2.1 Microring resonators

Optical micro ring resonator [48] is formed out of two waveguides, one forming a ring (**Figure 17**). The main difference to the 1D cavities is the absence of the mirrors, which make the processing of them easier and allows to reach higher quality factors. . In this case, a fully dielectric structure is

used, resulting in narrow lines compared to surface plasmon resonances (SPR). But the sensitivity depends not only on the narrowness of the line but also on the overlap. SPR lines, although broad, have a good overlap with the material under investigation. With perforations we improve overlap and sensitivity. The light is propagating inside the bus waveguide till it reaches the coupling region and is coupled to the microring resonator. The coupling takes place via the evanescent field (**Figure 3**) when the mode is close enough to the microring resonator some of the light leaks into the microring resonator. The modes which are in-phase with the transmitted modes of the bus waveguide are excited (constructive interference effect creates a comb of microring resonances). Only the light, which matches the resonance condition is coupled into the ring:

$$\lambda_m = \frac{2\pi r n_{eff.}}{m} \tag{11}$$

where λ_m is the resonance wavelength and r is the radius of the ring. The equation means that for light to interfere constructively inside the ring resonator, the circumference of the ring must be an integer multiple of the wavelength of the light. Thus, the mode number must be a positive integer for resonance to take places. The rest of the light which does not match the resonance condition goes through. In contrast to 1D resonator, here no standing waves are formed. It is a traveling wave resonator, meaning that the electromagnetic mode is propagating inside the ring.

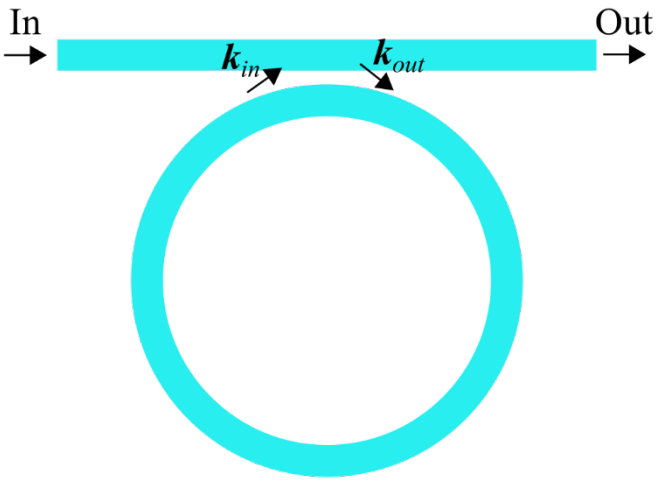

Figure 17. Integrated optical microring resonator. Top view of an integrated optical microring resonator having a bus waveguide and ring-shaped waveguide, which forms an optical microring. “In” and “Out” show

the coupling and outcoupling of the light. k_{in} and k_{out} show the coupling constants.

An example a 2D Finite-Difference Time-Domain (FDTD, more in section 2.1 simulation of electromagnetic field propagation inside an optical microring resonator is shown in **Figure 18**. As the optical mode reaches the microring resonator it evanescently couples into it (as seen from red and green blobs, which extend into the ring resonator). The light, which matches the resonance condition, couples into the ring (red and green colors inside the ring) and the light that does not continues to propagate.

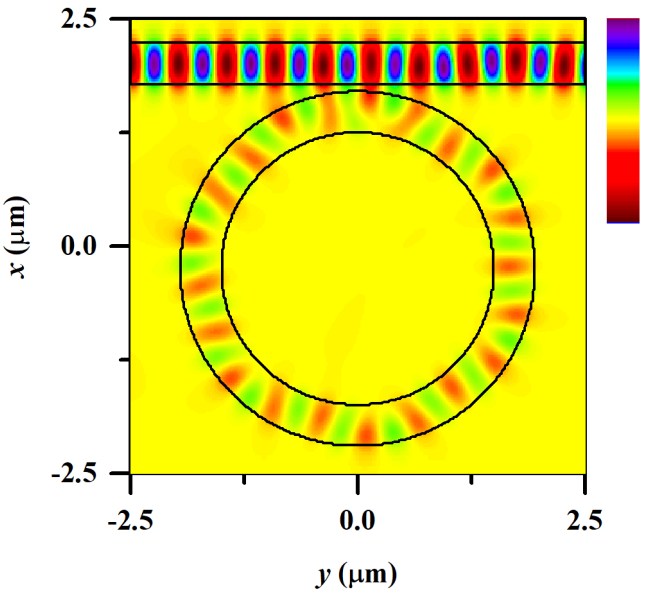

Figure 18. Electromagnetic field distribution inside microring resonator. 2D FDTD simulation of TM polarized mode propagating inside the optical microring resonator (Fig. Figure **17**). Black lines indicate boundaries between high and low refractive index media, blue and red colored blobs indicate propagating electromagnetic field. Linear color scale on the right indicates electromagnetic field amplitude ranging from -1 to 1. Bus waveguide width is 450 nm, inner radius of the ring is 1500nm, outer radius of the ring is 1950 nm, Si was used as high refractive index material and air was set as a cladding.

The ring resonator in the example of a Silicon On Insulator (SOI) based device, meaning that ring resonator and the bus waveguide are made out of Si and very sharp bends are possible. The higher the bends, the higher the

electromagnetic field extension out of the ring resonator as visible from red and green blobs extending through the outer ring resonator radius.
Other effects which apply to 1D optical cavities also apply for the ring resonator. The FSR for the ring resonator can be expressed as:

$$\mathrm{FSR} = \frac{\lambda^2}{n_g L} \tag{12}$$

where L is the roundtrip length (**Figure 19**). As for 1D cavity case the coupling to the optical resonator can be modified. Here it is altered by modifying the distance between the ring resonator and the bus waveguide. The shorter the distance, the more over coupled the ring resonator is to the bus waveguide and the further the distance, the more under coupled the ring resonator is. If the distance is too large, the light will not couple from the bus waveguide to the ring resonator

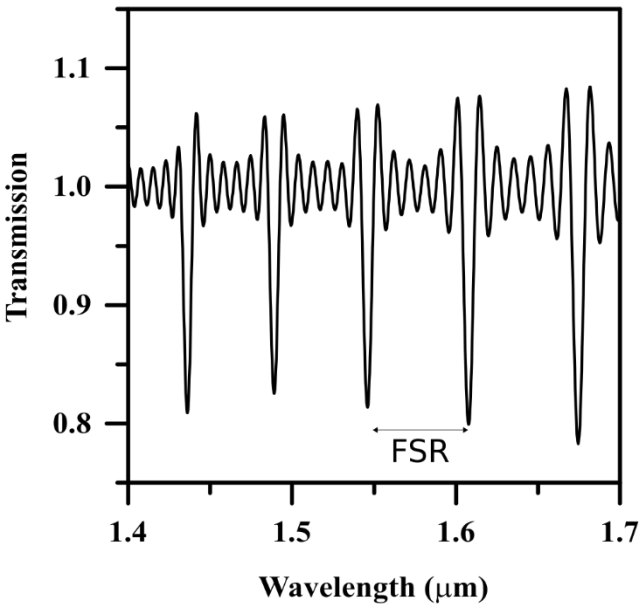

Figure 19. Transmission spectra of optical microring resonator. Transmission of TM polarized light captured at the output ("OUT") of the bus waveguide. Dips in transmission represent the longitudinal modes guided in the ring resonator. Noise, close to unity transmission, stems from low simulation resolution.
Similarly, the phase of the resonance frequencies can also be changed (**Figure 20**) by modifying the coupling or modulating the ring resonator. The

latter can be interesting for devices such as lidar [49] or optical sensors (section 1.3).

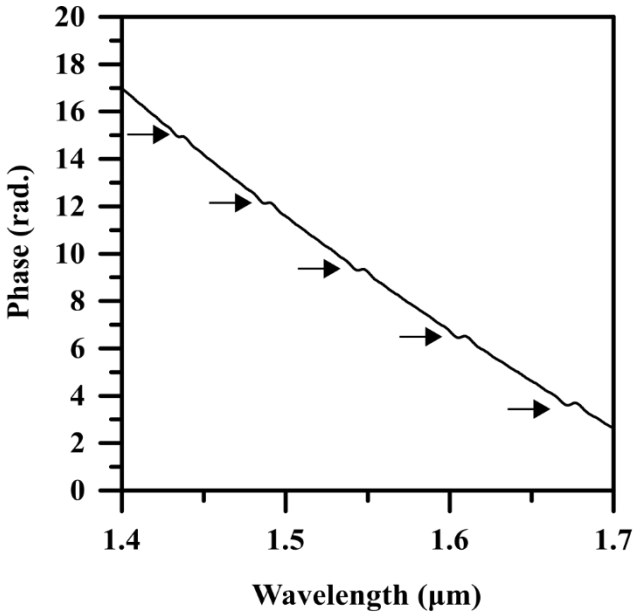

Figure 20. Phase of optical resonances. Phase change at the resonance peaks. Arrows indicate optical resonances.

1.3 Principal of integrated photonic sensors

The main principle of an integrated photonic sensor relies on the $n_{eff.}$. Due to the evanescent field (**Figure 21** indicated by black lines) which extends into surrounding media the guided optical mode is sensitive to the any change of conditions (i.e. particles present in the vicinity of the waveguide or cladding material change).

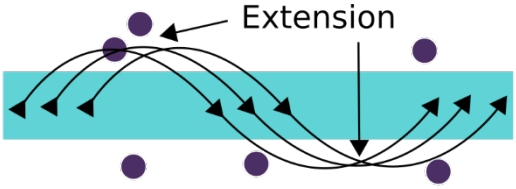

Figure 21. Principal of optical sensing. Sketch of an optical sensing where particles (indicated as violet circles) change the effective refractive index influencing propagating optical mode.

To boost the sensitivity of to the outside media, optical resonators are used. Due to circulating (ring resonators) or standing (1D resonators), light the effective interaction length is increased giving light the chance to interact multiple times with the same media. **Figure 22** shows an example of a ring resonator covered with particles. The particles induce $n_{eff.}$ change and lead to the resonance frequency shift (equation 11). The resonance frequency shift is shown in **Figure 23**. Due to addition of the particles the resonance shifts by 0.4 nm. This means that a very precise detector having a resolution on the order of few pm is necessary. Other approach is to use a tunable laser with a very sharp linewidth and scan with it over the region of interest (section 2.3).

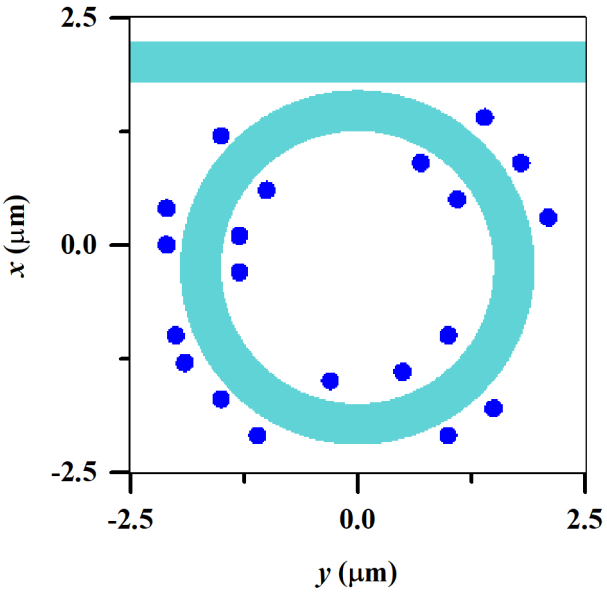

Figure 22. Sensing using microring resonator. Sensing scheme, where blue colored particles are placed in the vicinity of the microring resonator. Particles have refractive index of 4 and diameter of 100 nm.

To induce a higher change, more particles can be used or even the full top cladding can be changed. **Figure 24** shows a transmission spectrum of a microring resonator when the cladding was changed from air ($n = 1$) to water ($n = 1.33$). The resonance peak shifts by 3 nm. Here the sensitivity is:

$$S = \frac{\Delta\lambda}{\Delta n} \tag{13}$$

where $\Delta\lambda$ is the resonance peak position change and Δn is the refractive index change giving us a sensitivity of $S = 9$ nm/RIU (RIU — refractive index unit). This is a very low value and can be improved by designing a resonator having a better overlap with the surrounding medium (i.e. making a waveguide thinner, increasing the Q, etc.).

In general, photonic sensors [16, 17] involve microfluidic channels on top of the resonator array (section 2.3). They deliver the analytes to the resonators. To effectively detect the analytes the resonators are first functionalized [50]. The functionalization is performed using the same microfluidic channel which is later used to transport the analytes (i.e. blood cells). It is possible to remove the attached materials, however the cleaning process is not always possible.

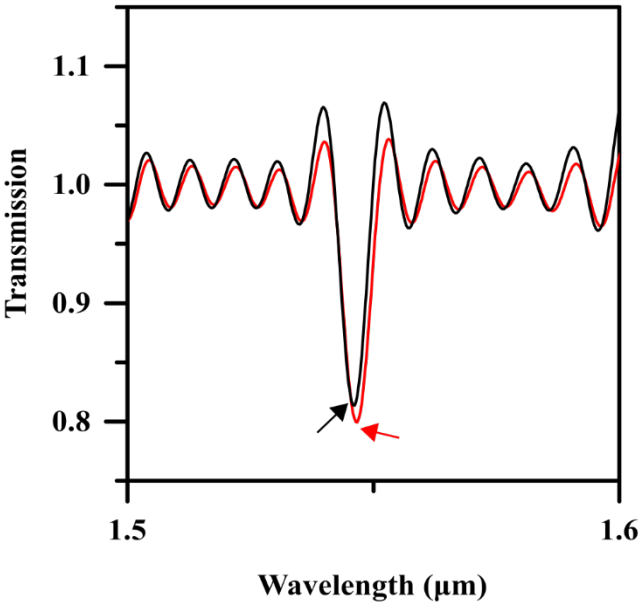

Figure 23. Transmission shift due to particles. Transmission shift induced by dielectric particles within the evanescent field of a microring resonator. Black curve indicates transmission with no particles and red — with particles. Black and red arrows indicate resonance peaks without and with particles respectively.

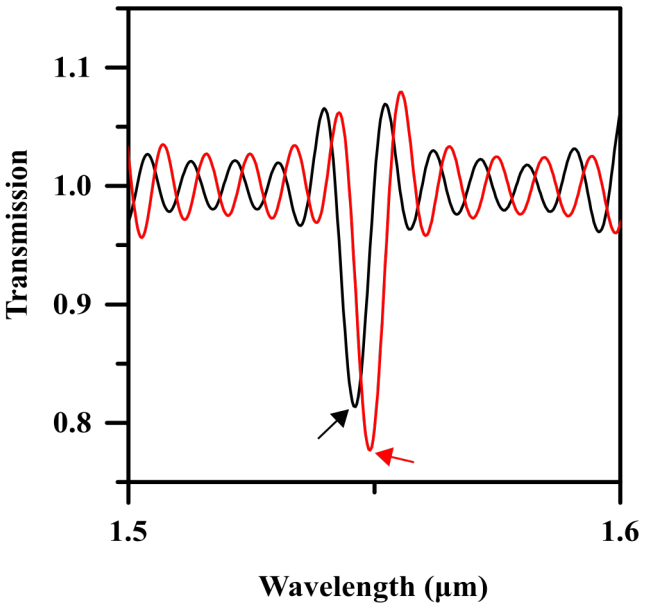

Figure 24. Transmission shift due to cladding change. Transmission shift induced by the cladding medium. Black curve denotes air as cladding and red — water (n = 1.33). Black and red arrows indicate resonance peaks with air and water cladding respectively.

2. METHODS AND MATERIALS

2.1 Simulations

In this chapter, an overview of used simulation techniques will be given. First a FDTD method will be defined. Secondly, an explanation of definite-frequency eigenstate solving technique will be given.

2.1.1 Finite-difference time-domain

To simulate electromagnetic waves propagating in photonic structures FDTD algorithm is commonly used. The principle of the algorithm is based on dividing the space and time into square cells and calculating the temporal evolution of Maxwell's equation in each cell. To understand the FDTD algorithm we first start with time dependent Maxwell's equations in differential form. First equation is Ampere's law:

$$\frac{\partial \boldsymbol{D}(t)}{\partial t} = \nabla \times \boldsymbol{H}(t) - \boldsymbol{J}(t) \tag{14}$$

here $\boldsymbol{D}(t)$ is the electric field displacement field, $\boldsymbol{H}$ is the magnetic field, t is time and $\boldsymbol{J}$ is the electric charge current density. This expression means that the total magnetic field is proportional to the electric current passing through the loop. The next equation is Gauss's law:

$$\nabla \cdot D = \rho \tag{15}$$

where ρ is the charge density. Gauss law states that the electric flux through any close surface is proportional to the total electric charge enclosed withing a finite surface. The third law is Faraday's law:

$$\frac{\partial \boldsymbol{B}(t)}{\partial t} = -\nabla \times \boldsymbol{E}(t) \tag{16}$$

here $\boldsymbol{B}(t)$ is the magnetic induction field and $\boldsymbol{E}(t)$ is the electric field. Faraday's law says that the change of magnetic field creates a voltage. The fourth law is Gauss's law for magnetism:

$$\nabla \cdot B = 0 \tag{17}$$

Gauss's law for magnetism states that there are no magnetic monopoles. Here we can also write some simplifications. If linear, nondispersive dielectric materials are used $\boldsymbol{D} = \varepsilon \boldsymbol{E}$ and $\boldsymbol{B} = \mu \boldsymbol{H}$, where μ is the permeability of the medium.

In this thesis an open source FDTD solve MEEP [51] was used. MEEP defines the interaction of magnetic and electric field with matter and electromagnetic sources. Via wavelength dependent ε and $\boldsymbol{E}$ material

properties and nonlinearities are introduced into the simulation. If needed the solver can have gain and losses introduced.

The total space, which is calculated by MEEP, is called a computational cell. The whole computational cell is combined out of many small cubes, which form a grid. This grid is called a Yee lattice and is show in **Figure 25**a. The FDTD algorithm stores different components for different grid locations on different grid points. The positions where ***H*** is calculated are shifted by half of the lattice spacing from where ***E*** is calculated. The latter originates from Ampere's and Faraday's laws where the temporal evolution of the fields are related to their spatial evolution. To perform such simulations, values are interpolated by taking adjacent values. In time, for the following iterations (i.e. at t_{0+1}) values from the previous timestep t_0 are taken (**Figure 25**b).

To initialize the simulation, an electric current is introduced, which gives rise for electromagnetic fields. The electromagnetic field propagates inside the defined structure and couples to the structure supported modes or is radiated away and absorbed by absorbing boundary conditions. Absorbing boundary conditions are artificial materials such as perfect electric conductor (PEC, behaves as metallic mirrors) or perfectly matched layers (PML, PECs with absorbing material in front). They are required to avoid computational artefacts. To further reduce the numerical errors fine steps are used: Δx, Δy, Δz are set to approximately $\frac{\lambda}{10}$. The temporal resolution is also related to the spatial resolution:

$$\Delta t = \frac{C}{\sqrt{\frac{1}{\Delta x^2}+\frac{1}{\Delta y^2}+\frac{1}{\Delta z^2}}} \tag{18}$$

here $C \approx 0.9$ is the Courant factor and defines the convergence for solving partial differential equations.

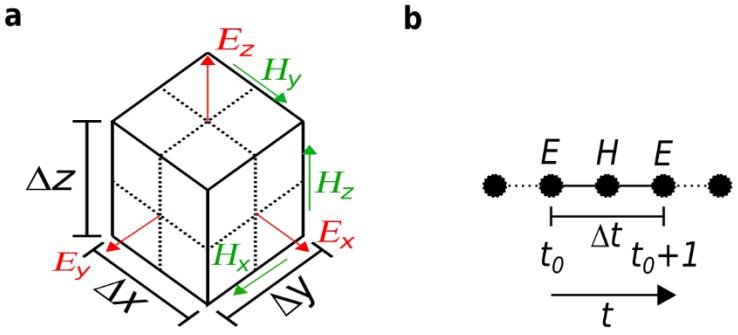

Figure 25. FDTD simulation principal. a, Schematic of the Yee lattice in space domain. **b**, Schematic of the Yee lattice in time domain. Red arrows indicate electric field components ($E_{x,y,z}$), green — magnetic field components ($H_{x,y,z}$), dashed lines — Yee grid with cell size defined by $\Delta x, \Delta y, \Delta z$. In **b** Δt depicts the timestep, t_0 — initial start time, t_{0+1} — time at the next step, t — time (increasing time denoted by black arrow) and black circles — different timesteps.

2.1.2 Definite-frequency eigenstates

In order to simulate definite-frequency eigenstates or modes which are supported by periodic structures of interest (i.e. a DBR), the freely available MIT Photonics Bandgap (MPB) solver was used [52]. It can simulate not only optical eigenstates but also dispersion relations.
MPB solves eigenvalue problem, which can be written as:

$$\nabla \times \frac{1}{\varepsilon} \nabla \times \boldsymbol{H} = \frac{\omega^2}{c^2} \boldsymbol{H} \tag{19}$$

where ω is the frequency. $\boldsymbol{H}$ is such that $\nabla \cdot \boldsymbol{H} = 0$. In order to find a solution of this equation a guess solution having an exponential form is used:

$$\boldsymbol{H} = \boldsymbol{H_k}(x) e^{ikx} \tag{20}$$

where $\boldsymbol{k}$ is the Bloch wavevector and $\boldsymbol{H_k}$ is the Bloch envelope, which defines a periodic function, leading to a solution of a set of modes forming photonic bands at specific wavevectors $\boldsymbol{k}$. The computational cell is then divided in discrete bins (number of points) to numerically solve the problem and a periodic part of the field is evolved as a sum of planewaves.

Since MPB solves only periodic problems, periodic boundary conditions are used, which prevent simulations with nonlinearities or absorbing media.

2.2 Sample fabrication

In order to fabricate the samples used in these thesis, various lithographical techniques were used. Thus, in the following sections a general approach of top-down (section 2.2.1) will be introduced. Then electron beam lithography (EBL, section 2.2.2) will be introduced. Thirdly, ultraviolet lithography will be explained (UVL, section 2.2.3). Finally, etching of the samples will be defined in section 2.2.4.

2.2.1 Top-down

Top-down is a subtractive process where materials are removed to introduce features of interest. As such, the technique relies on lithography and etching processes. The sketch of top-down is shown in **Figure 26**. First, a thin and smooth layer of resist is spin-coated [53] on the sample which will be later processed (**Figure 26**a). After that, the specific structure is exposed in the resist. The exposure is done either by EBL or UVL. The high energy electrons and photons alter the chemical structure of the resist (depending on the resist) making it resistant to the developer (**Figure 26**b). The developer then removes either unexposed or exposed resist leaving areas where the material is unprotected (**Figure 26**c) and forming a lithographical mask directly on the surface of the sample. Later the sample is introduced to high power Reactive Ion Etching (RIE, section 2.2.4), which removes the unprotected material (**Figure 26**d). If the mask of the resist is still present (not removed by etching) it is typically stripped using wet chemistry.

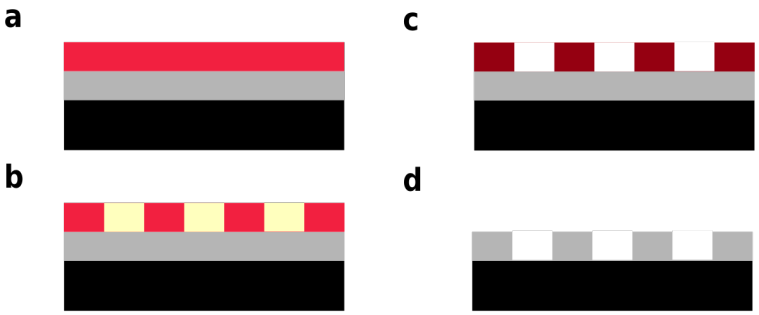

Figure 26. Top-down processing. a, Substrate is covered with resists. **b**, Desired structure is exposed either with e-beam (section 2.2.2) or UV lithography (section 2.2.3). **c**, Development of the resist. **d**, Etching (section 2.2.4) of the sample. Red color denotes the spin coated resist, gray color — material to be etched, black — substrate, yellow — exposed resist.

2.2.2 Electron Beam Lithography

One of the techniques to expose spin-coated resists is the EBL. EBL exposes the resist in raster fashion (step by step). Typical resolution of a 100kV EBL is 10 nm. This kind of accuracy is used to resolve most state-of-the-art devices. The basic process of EBL is show in **Figure 28**. A beam of high energy electrons is focused on the sample and exposes the resist (**Figure 28**a). By switching off and on or blanking the beam multiple spots are exposed (**Figure 28**b) forming an optical mask, which can be developed using a developer. The drawback of the EBL is possible damage to the surface of the material. Due to high energy electrons penetrate the sample and charge the surface. Moreover, secondary electrons could be emitted. This could cause some secondary effects such as rounding of exposed features. To prevent that, calibration runs are performed to adjust the shapes and dimensions of the lithographical masks. The other obvious errors are the stitching errors. Due to limited beam steering via magnetic field mechanical stages must be used. The latter could introduce displacement errors on the order of 100 nm. This is a problem for long waveguides (they could be completely misaligned). To overcome these issues, adiabatic tapers or specific alignment markers are used.

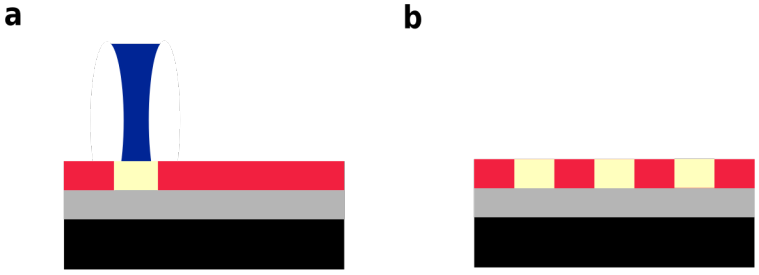

Figure 27. E-beam lithography process. a, Exposure with electron beam. **b**, Exposed desired structure. Blue color denotes electron beam.

2.2.3 Ultraviolet lithography

UVL is a similar technique to EBL, however, here the ultraviolet light (≈ 130 nm) is used to expose the optical mask (**Figure 29**a). The later steps are the same as for EBL (**Figure 29**b). The main difference here is the resolution. It is limited by the wavelength and is also on the order of 130 nm minimal feature size (Interuniversity Microelectronics Centre, IMEC). The position of the exposure is controlled using a metal mask, which shields the desired areas from the UV. The metal mask is typically formed on UV

transparent medium using EBL. The advantage of this method is the possibility to perform multiple expositions. This is the main method used in fabs for mass production of optical chips, electronics, etc

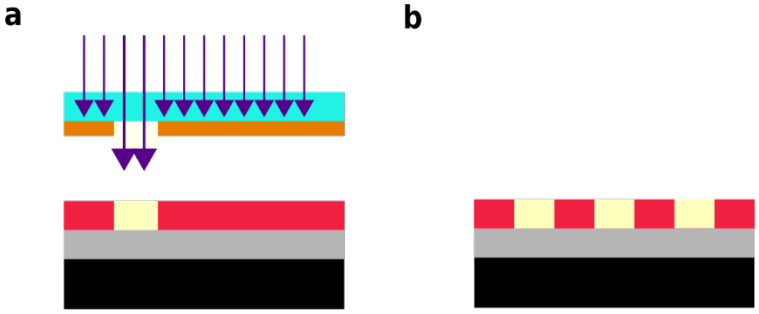

Figure 28. Ultraviolet lithography process. a, Optical resist is exposed through a mask. **b**, Exposed desired structure. Violet arrows indicate incident ultraviolet light, orange color depict optical metal mask deposited on ultraviolet transparent material (quartz).

2.2.4Etching

Etching is a technique used to remove the unprotected material. In such a way a pattern is transferred into the layer of interest. There are three types of etching: physical removal via momentum transfer (RIE), reactive plasma (Inductively Coupled Plasma, ICP) or chemical removal via gasses. In this work mainly RIE was used (**Figure 29**).

RIE is a process where material is removed by ion bombardment. The process is initiated by a radio frequency source, which creates an oscillating electromagnetic field, and ignites the plasma from a gas, which is injected into the vacuum chamber. Ions are then attracted by the electrode, on which the sample is positioned, and bombard the sample and etch the material via the momentum transfer. The areas, which are protected by the mask, are not etched unless the mask is etched away (selectivity is too low). Because of that, masks, which are resistant to these processes, are being heavily developed.

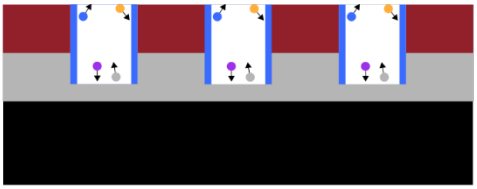

Figure 29. RIE etching process. Schematic of etching process. Violet circles denote the ions with kinetic energy, gray circles depict removed material, orange circles — other gasses, which contribute to sidewall passivation, red circles — material etched from passivated layer and arrows, which are connected to colored circles, denote the approximate direction.

In more detail, as the accelerated ions (violet color in **Figure 29**) bombard the unprotected material, other gasses are introduced in the chamber (yellow circles) to passivate (protect it from etching by forming an etch resistant surface) the sidewalls (indicated by blue color). The passivated layer can also be etched (blue circles) by the incident ions or etched particles (grey circles). After such a process the vacuum chamber of the tool is contaminated with various chemistry. To clean it several pump and purge cycles are performed.

2.3 Experimental setup

To characterize the samples an optical measurement setup was constructed. However, before that the coupling of light into the optical chip will be discussed. As the devices are exceedingly small (on the order of several microns) it is very hard to couple them to an optical fiber. To do that an optical 2nd order Bragg grating is used (grating coupler, **Figure 30**a). The general form of a Bragg condition is:

$$\beta - k = m \cdot K \tag{21}$$

where $\beta = 2\pi n_{eff.}/\lambda$ is the wavevector of the input wave (**Figure 30**b propagating inside the waveguiding having thickness h and width w), $k = 2\pi n/\lambda$ depicts the component of the wavevector of the diffracted wave in the direction of incident wave (projection of the incident wave on the grating) and $K = 2\pi/\Lambda_{2\text{nd. }Bragg}$, which denotes grating diffraction condition. As such, equation 21 can be simplified to:

$$n_{eff.} \cdot \Lambda - n \cdot sin(\theta) \cdot \Lambda = m \cdot \lambda \tag{22}$$

If the conditions are set right the light launched from the Lensed fiber (a fiber with tapered end, which is around 100 nm in diameter) couples into the grating coupler which then directs the light into the adiabatic converter (trapezoid shaped part in between the grating coupler and the waveguide), which slowly decreases the size of the mode such that it matches the waveguides mode. This is needed to reduce the optical losses of system. The mode then propagates until it reaches the optical resonator (**Figure 17**). After that mode is sent back to the same grating coupler and is outcoupled into the fiber using identical lensed fiber (**Figure 30**c).
The whole optical sensor is composed on a small chip (**Figure 31**, $\approx 20{:}\,20\ mm$). The samples are designed to be exposed by materials of interest (the one that will be used for sensing). This is achieved by forming a Polydimethylsiloxane (PDMS, [54]) microfluidic channel on top of chip. PDMS is glued on the chip in such a way that the grating couplers are not covered. This enables easy positioning of the lensed fibers and protects the grating coupler from the possible contamination.

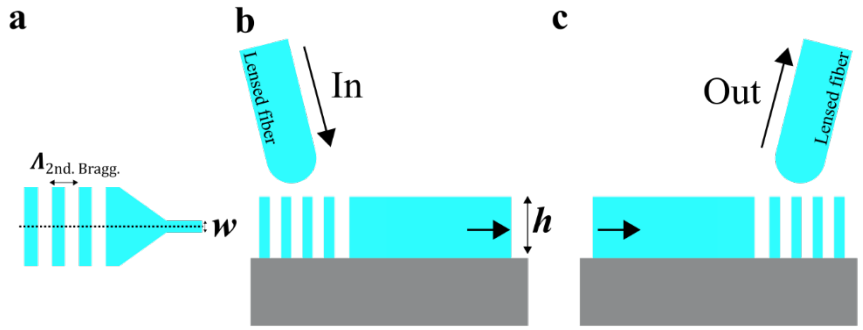

Figure 30. Coupling scheme. a, Top view of a grating coupler. **b**, Cross section of the grating coupler in in-coupling scheme. **c**, Cross section of the grating coupler in out-coupling scheme. Dashed line in **a** depicts the cross section in **b** and **c**, $\Lambda_{2\text{nd. Bragg}}$ — period of the 2$^{\text{nd}}$ order integrated Bragg grating, lensed fiber depicts the fiber, which adiabatically converts the propagating mode into a different sized mode and in/out couples the light to the next element.

PDMS channel has two ports (injection, where liquid is injected, and aspiration, where the liquid is removed, from the sample). These ports are coupled with a buried channel (**Figure 31**, indicated by dashed blue line).

The tubes from the syringes are connected to the injection and aspiration channel forming a sealed flow channel.

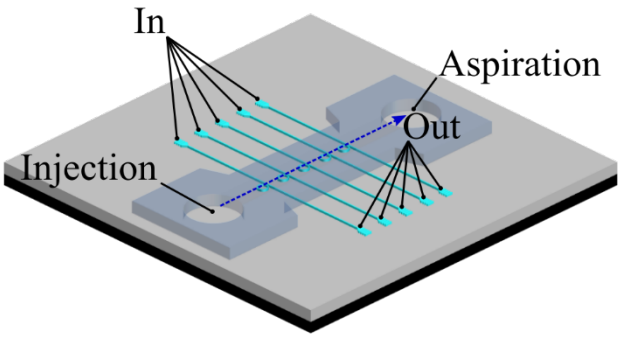

Figure 31. Microring resonator array with microfluidic channel. Microring resonators are positioned in the center of the chip and coupled to the grating couplers, which are used to couple the light in and out. The array is covered with PDMS channel to inject and aspirate the fluid with analytes.

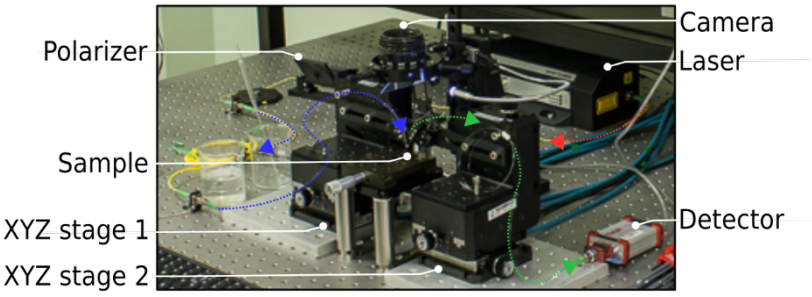

Figure 32. Experimental setup. Computer controlled optical setup. Red dashed line indicates output light, which goes to the in-line polarizer, from the fiber coupled laser, blue dashed line — light coming from the polarizer to the sample, green dashed line — light coming from the sample to the detector. Arrows indicate the propagation direction.

To excite optically and to probe the sample an optical setup is built (**Figure 32Figure 33**). A light is fiber coupled from a narrowband tunable laser (Thorlabs Intun TL1550 B) operating in C-band (1530 to 1565 nm) into a single mode fiber (indicated by red dashed arrow), which couples the light into the polarizer, required to match the polarization of the polarization

dependent grating coupler. The light is then coupled back into the angled single mode fiber, which is then coupled to the polarizing lensed fiber. The latter removes the reflections from the facets of the fiber in turn reducing the chance of possible standing waves. The mode from the lensed fiber is sent onto the grating coupler where it is coupled into the on-chip optical waveguide (**Figure 33**). The light is then collected by the lensed fiber and directed to a photodiode ().

A principal scheme is shown in **Figure 34**. To position the lensed fibers, two XYZ positioners (Newport) having a resolution of 10 nm are used. These are necessary as the alignment is critical for the grating couplers. Additionally, the angles of the lensed fibers are controlled using manual rotational positioners (Standa). These are required to match the proper angle of the grating couplers, which are designed for the specific chips. The whole setup is positioned on an air suspended table to reduce the vibrations, which could lead to noise sources as the lensed fibers could vibrate and create alternating standing wave patterns in the measured spectra. This is crucial for this setup since the measurement is performed by sweeping the laser source and integrating the outcoupled light with the photodetector.

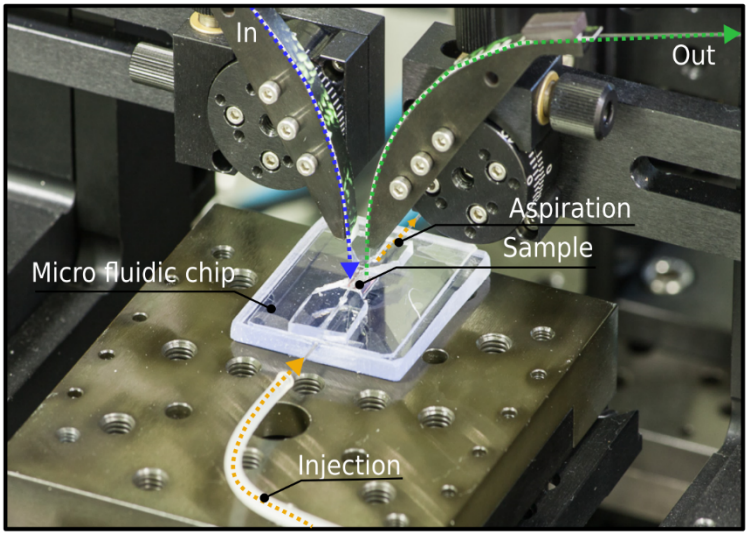

Figure 33. Zoom in of the microfluidic chip. Blue dashed line indicates the in coupling lensed optical fiber, green dashed line — out coupling lensed optical fiber, orange dashed line — injection and aspiration channels in and from PDMS based microfluidic channel.

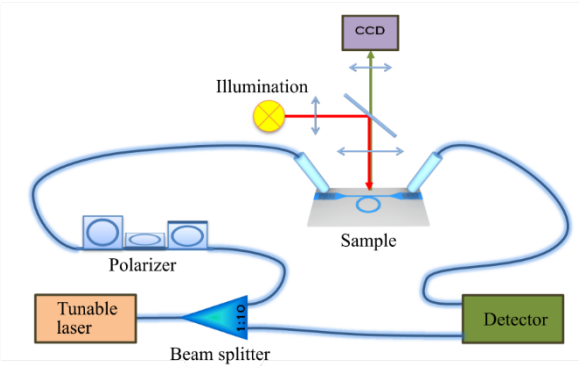

Figure 34. Sketch of optical setup. Light is coupled from the tunable laser into an optical fiber and split using the 1:10 beam splitter into two channels: sample (goes to the polarizer) and reference (goes to the detector). The polarizer allows to adjust the polarization which is required to optimize the coupling to the grating coupler. After the sample, the light is collected with the lensed fiber and sent to the detector. To position the sample, it is illuminated with the light source and imaged by the CCD.

3. RESULTS

3.1 A perforated microring resonator for optical sensing applications

The following chapter is based on article:
DOI: 10.1088/2040-8978/16/10/105003
© IOP Publishing. Reproduced with permission. All rights reserved

Previously in section 1.3 we discussed a general principal of a photonic sensor. To increase that effect various approaches can be used. In the following section numerical simulations of a refractive index sensor based on a perforated optical microring resonator are presented. It is shown that the introduction of subwavelength perforations in the microring resonator increases the light–matter interaction and the sensitivity of the microring resonator. The sensor performance is analyzed in two sensing schemes: bulk sensing and dielectric particle sensing. In both applications the perforated microring resonator sensor outperforms an ordinary microring resonator sensor and maintains high Q. The simulations were performed using finite-difference time-domain (section 2.1.1) and finite-element methods.

3.1.1 The perforated microring resonator and simulation methods

A schematic diagram of a four-port device based on a perforated microring resonator is presented in **Figure 35**a. The resonator consists of a ring with outer radius R_{out}, inner radius R_{in}, and refractive index n_c. The ring contains a total number N_d of low dielectric constant material (refractive index $n_c < n_s$) hollow core defects. The detailed geometry of the defects is shown in **Figure *35***b.

The resonator is coupled to two identical straight waveguides with width wg_w and refractive index n_c. The entire device is embedded in a host material with refractive index n_s. The computational window is surrounded with PML.

Defects are made from two connected cylinders. The radius of the inner cylinder is r_1 and the radius of the outer cylinder is r_2. The distance from the middle of the ring (defined as $(R_1 + R_2)/2$) to the center of the inner cylinder is d_1, and that to the center of the outer cylinder is d_2.

The angularly averaged refractive index for our structure would be a function of the radial coordinate. Different defect parameters would result in different average refractive index distributions. As such, in principle, an effect of the gradient refractive index like that obtained with grayscale lithography can be achieved [55]. As for the refractive index sensor,

perforations increase the area in which the propagating mode interacts with the surrounding medium. Also, due to the lower mode confinement inside the core material, the evanescent field extends further into the surroundings. Both effects increase the sensitivity of the refractive index sensor. It can be noted that one drawback of an ordinary microring resonator is that the evanescent field does not extend far from the core material. As such, the design overcomes this drawback.

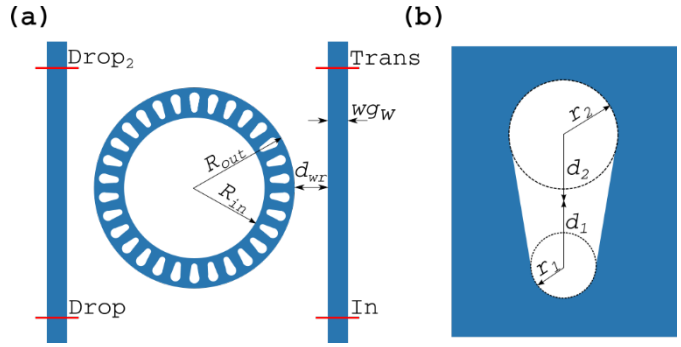

Figure 35. Geometry of microring resonator. a, Schematic diagram of a four-port device with two straight waveguides and a perforated microring resonator. **b**, Enlarged portion of the resonator, showing the detailed geometry of the defects.

To model the perforated microring resonator, 2D FDTD (with free software package MEEP [51]) and FEM (with the commercial Comsol Multiphysics software) simulations were performed. We mainly used FDTD to get drop port intensity spectra, since FDTD allows us to easily obtain the system response to a wide wavelength pulse. FEM was used to get steady state solutions at a particular excitation frequency, assuming an $e^{i\omega t}$ time dependence of the electromagnetic field, where i is the imaginary unit, ω is the angular frequency and t is the time. One advantage that FEM has over FDTD is its flexibility in using a non-uniform mesh. FEM was used to check the results obtained with the FDTD.

While the full three-dimensional simulations are necessary for determining parameters of the device, as intended for use in real world applications, two-dimensional simulations can also provide some insight into the structure of the resonator and its performance. Also, as the geometry of the structure becomes complicated, with finer details, a smaller grid step size is required. As such, simulations of a structure with fine details in 3D become time-consuming. Therefore, most of the results presented in this work came from 2D simulations. However, at the end of the chapter the

results of a few 3D simulations that show the possibility of getting the same performance in 3D as in 2D by changing some of the geometrical parameters of the structure are shown.

The measure of resonator performance is based on calculations of two parameters: the sensitivity (S) and the quality factor (Q). Basically, there are two sensing mechanisms that are commonly used: surface sensing and bulk (or volume) sensing [17, 16]. Bulk sensing is based on detecting the change of the average refractive index which is induced by the presence of analytes in the whole evanescent field region (**Figure *36***a). Surface sensing is based on the amount of analytes distributed in the vicinity of the microring resonator, which can be interpreted as a thin coating covering the core (**Figure *36***b). The shift of resonance wavelength which is induced by homogeneous distribution of analytes in aqueous cladding or deposition of analytes on the surface of a resonator is monitored. The main parameter describing the sensors performance is the sensitivity *S*. The smallest detectable wavelength shift does not depend on the resonance bandwidth or the resonance shape and should be determined by the resolution. However, noise can modify the resonance spectrum, so accurate detection of the resonance wavelength shift becomes difficult for a broad resonance line shape. To enhance the accuracy, a narrower resonance is required, which in turn means that a higher Q value of the resonator is required.

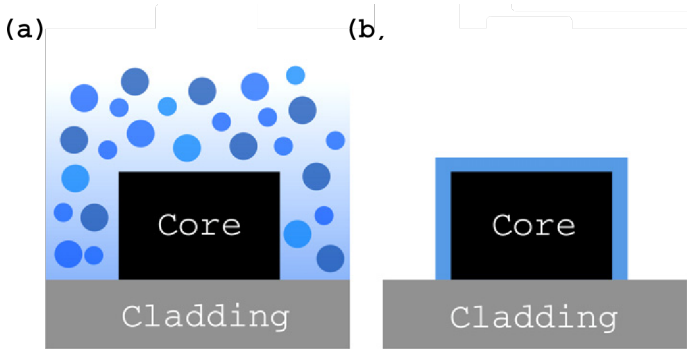

Figure 36. Sensing mechanisms. a, Homogeneous sensing. **b**, Surface sensing.

3.1.2Results and discussion

The defects used allow a wide range of different perforation geometries. For example, setting $d1 = d_2 = r_w$ and $r_1 = r_2$ layers of alternating low and high refractive indices are obtained. If $d_1 = d_2 = 0$ and $r_1 = r_2$ circular holes centered in the core material are achieved. In this work a focus on a design,

which has both a relatively high Q factor and a relatively high sensitivity, and has a resonance close to λ = 1.55 μm, is presented. After performing several simulations, it was observed that as the area of the defect gets larger, the Q factor decreases, and the sensitivity increases. The parameters of the waveguide and the ring itself were fixed to: R_{out} = 2.2 μm, R_{in} = 1.85 μm, wg_w = 0.25 μm, n_c = 3.46, n_s = 1.46. Defect parameters, with which high Q, high sensitivity and mode matching with the waveguide are obtained, are as follows: N_d = 80, r_1 = 0.03 μ μm, r_2 = 0.048 μm, d_1 = 0.0575 μm, d_2 = 0.0575 μm. The coupling gap (the distance between the waveguide and the ring) was set to 0.2 μm. A grid step size of 10 nm was found to be sufficient for FDTD simulations for wavelengths close to 1.55 μm. At first glance, a grid step size of 10 nm would seem to be too large, but MEEP has a material averaging feature, which helps to maintain second-order accuracy at the material interface and allows one to use a larger step size [56]. The resonance wavelength and Q factor obtained with a 5 nm grid step size differed only by 0.05 % and 1.64 % from the ones obtained with a 10 nm grid step size. FEM was also used to check the results from FDTD close to λ = 1.55 μm and the agreement was good. The mesh used in the FEM simulations is shown in **Figure 38**a.

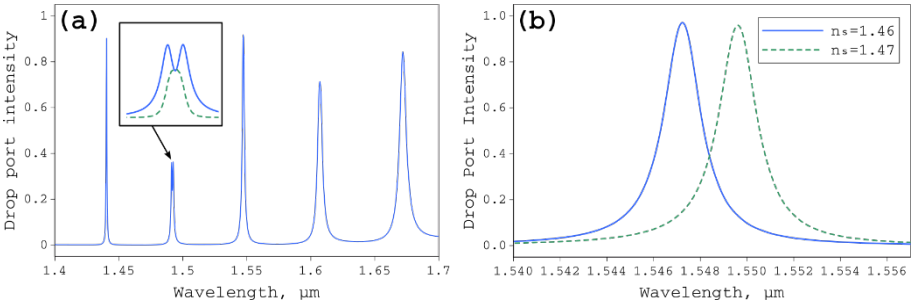

Figure 37. Transmission of the ring resonator. a, Normalized drop port intensity. The inset shows an enlarged portion of the figure at the wavelength 1.492 μm. In this inset, the solid line represents the drop port intensity, and the dashed line represents the drop2 port intensity. **b**, Shift in drop port intensity peak as the refractive index of the host material is altered from 1.46 to 1.47.

The placement of the defects is crucial to the total internal reflection effect. As the defects get closer to either the inner or the outer edges of the microring, the average refractive index of the core at that edge gets smaller. This change in average refractive index induces a change of the critical angle for total internal reflection. It is apparent from equation 1 that decrease of n_2

(n_{high}) decreases the number of wavevectors experiencing the total internal reflection effect inside the perforated microring resonator. Thus, the modulation of the average refractive index allows to pull the light towards and away from the resonator center and correspondingly change the light interaction with the surrounding medium. However, the defects should not touch the edges of the ring; otherwise, due to the loss of n_{high} near the edge of the ring resonator, the total internal reflection would be negligible and correspondingly strong scattering of the light and a decrease of Q would be inevitable.

FDTD was used to get drop port intensity versus wavelength data for resonator structure. Excitation with a sinusoidal pulse having a Gaussian envelope in time at the bus waveguide was used to cover the wavelength window from 1.4 μm to 1.7μm. The calculated normalized drop port intensity is shown in **Figure 37**a. The resonance peak corresponding to λ = 1.547 μm has a Q value of about 800.

Two close peaks at λ = 1.492 μm visible in **Figure 37**a are the result of mode splitting. The inset in **Figure 37**a shows drop and $drop_2$ port intensities at this wavelength. The peak in the $drop_2$ port intensity spectra occurs due to a counter-propagating mode. This counter-propagating mode can be the result of the discretization used in the simulation and/or the periodic nature of the structure. This effect is also observed in experiments with a microring resonator having no defects [5]. Its cause is surface roughness, which manifests itself in back scattering of the propagating field. In this case the back reflection is caused by the finite resolution of the rectangular grid used to describe the perforations. The simulation done with FEM reveals that there is no counter-propagating mode at this wavelength, because the device operates below the first-order Bragg bandgap.

To evaluate the bulk sensitivity of a resonator, the refractive index of the host material is slightly altered, on the assumption that the microring resonator is not strongly disrupt. Here n_s is altered from 1.46 to 1.47. The shift of the drop port intensity peak is presented in **Figure 37**b.

The FDTD and FEM simulations showed the same resonance wavelength shift of approximately 2.4 nm when the refractive index of the host material was increased by 0.01. The sensitivity S of 240 nm/RIU is achieved. In comparison, an ordinary microring resonator with the same spatial parameters and no perforations has a sensitivity S of 80nm/ RIU. The increase in the sensitivity by a factor of three must be attributed to the perforations. Not only do the perforations increase the total surface area of the resonator to about triple, but also they increase the total electromagnetic

field energy in a low dielectric constant material, which could be essential for applications in nonlinear optics. The field amplitude at the resonance wavelength of λ = 1.547 μ m is shown in **Figure 38**b.

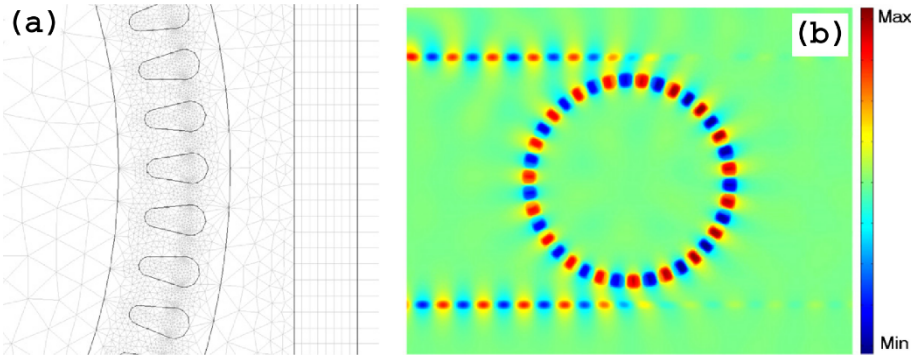

Figure 38 | Simulation geometry. **a**, Mesh used in FEM simulations. **b**, Field distribution at λ = μ 1.547 m.

Simulations show that the *Q* factor of the perforated microring structure can be increased while keeping the same sensitivity in a couple of ways: i.e. changing the coupling gap from 0.2 μm to 0.3μm increases the *Q* factor to 3054 (**Figure 39**a). However, a further increase of the coupling gap results in a lower amplitude of electromagnetic radiation circulating inside the resonator and hence a smaller resonance peak in either the drop port or the transmission port intensity spectra, thus complicating detection of the signal in real world applications. From **Figure 39**a we can see that with a coupling gap of 0.2 μm, the resonator is under coupled. For critical coupling, the coupling gap should be reduced to 0.1 μm and at this distance the normalized transmission port intensity is close to 0 while the drop port intensity is almost 1.

Figure 39b presents radiation losses per round trip versus the radius of the microring resonator. To get these results the time that it takes for a mode at λ = 1.547 μm to travel one full circle around the resonator, and the *Q* factor of that mode were calculated. This allows to calculate the loss per round trip. The same density of perforations was kept for all radii of the rings. A larger radius results in a smaller curvature of the ring. In turn this reduces the scattering from side walls. The radiation loss per round trip saturates (minimum losses) at a radius of 5 μm. This indicates that the main factor causing losses is the scattering of light from the perforations.

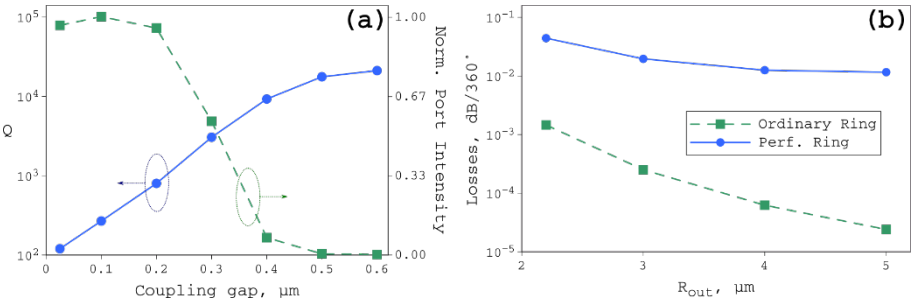

Figure 39. Quality factor and losses. a, Q factor and normalized drop port intensity versus coupling gap. **b**, Radiation losses for various outer radii of the perforated microring resonator. For comparison, the same losses are plotted for an ordinary ring resonator with the same geometrical parameters.

To evaluate the shift of the drop port intensity peak (surface sensing) which would be induced by dielectric particles distributed on top of the resonator, random distributions of various numbers of dielectric cylinders having radius of 30 nm with refractive index 1.5 were introduced near the surface of the resonator (**Figure 40**a). For this, the host refractive index was changed to 1.33 to mimic that of the water. Ten simulations with different random distributions of dielectric particles were performed. The results presented are their averages. It can be noted that the exact position of the dielectric particle (provided that it is small and does not have a refractive index much higher than that of the surrounding media) is not as crucial as it is in, for example, the case of gold particles [57]. The resonance peak shift for various distributions and amounts of particles is presented in **Figure 40**b. With dielectric particles inside the defects, the resonance peak shift is twice that for setups where dielectric particles are distributed on either the inner or the outer surfaces of the resonator: 0.285 nm versus 0.164 nm and 0.175 nm for 10 particles. When dielectric particles are distributed all over, the resonator shift of 0.592 nm results. This is almost the sum (the sum would be 0.623 nm) of the three previous cases. This result can be explained via the wavelength shift prediction based on a model from coupled mode theory [5]: $\Delta\lambda = \Delta n_{eff}\, \lambda_r / n_g$ where Δn_{eff} is the change in effective mode index caused by the change in surrounding media refractive index. The effective index of the propagating mode depends strongly on the refractive index of the surrounding material. When there is more material with higher refractive index (as in the case where a layer/particle s are distributed all over the resonator), the change in effective index is larger. And so is the change in resonance wavelength.

As the number of particles increases approaching the state of a homogeneous dielectric layer, the shift approaches the value of 26.748 nm. Calculations here show that even a small number of dielectric particles at the resonator surface have an observable effect on the drop port intensity spectrum shift, showing that inner defects (which can be customized for the different particles) allow to increase the sensitivity by increasing the total area of interface between the microring resonator and the surrounding medium.

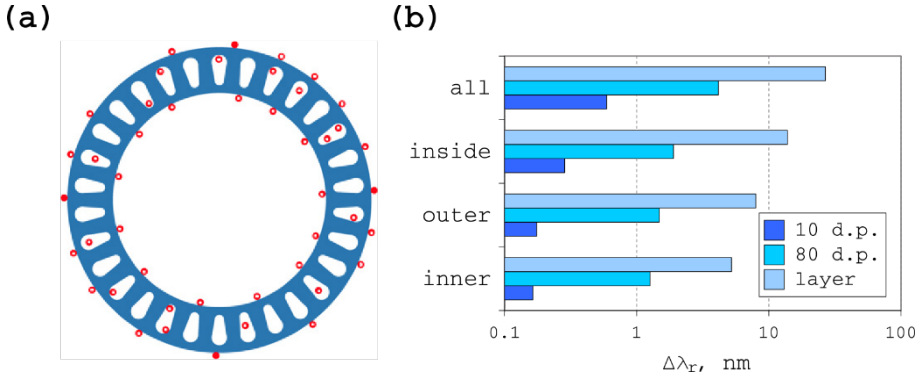

Figure 40. Distribution of dielectric particles. a, Random distribution of the dielectric particles (red color) around and inside the perforated microring resonator. **b**, The shift in the drop port intensity peak induced by 10, 80 and an infinite number (simulated as a layer) of dielectric particles covering the resonator when the dielectric particles are distributed: at the inner surface of the ring; at the outer surface of the ring; inside the defects; and on all surfaces.

Resonators have been also simulated in 3D to see how their performance changes when the radiation losses along the direction perpendicular to the structure are introduced. Using same parameters as in the 2D calculations sensitivities of 432 nm/RIU and a Q values of 370 at the resonance wavelength $\lambda = 1.52$ μm have been achieved. Increasing the outer radius of the resonator from 2.2 μm to 3μm and the number of defects from 80 to 118 resulted in a lower sensitivity (332nm/RIU) and a higher Q value (700).

3.1.3Conclusions

A novel microring resonator structure with low dielectric constant material defects has been proposed for refractive index sensing applications. Its performance in bulk and surface sensing schemes has been analyzed. It was shown that proposed refractive index sensor based on a microring resonator

outperforms ordinary microring resonators. The perforated microring resonator presented allows variation of the quality factor and the sensitivity, making it applicable in many optical areas. The design not only achieves high sensitivity, but also increases the total area of the interface between the microring resonator and the surrounding medium, which can increase the light–matter interaction with aqueous media and gases.

3.2 Ultra-wide free spectral range, enhanced sensitivity, and removed mode splitting SOI optical ring resonator with dispersive metal nanodisks

The chapter is based on article:
DOI: 10.1364/OL.40.002977
© The Optical Society. Reproduced with permission. All rights reserved

In the previous chapter we talked about a perforated microring resonator sensor. However, such a sensor is limited by the free spectral range, meaning that if the shift of the resonances is higher than the FSR (i.e. when the ambient material of a ring having a large radius, small FSR, is changed from air to water) the detection becomes impossible. To overcome that a refractive index sensor with a free spectral range that is unlimited by neighboring mode spacing (10-fold increase with respect to 20 nm of an unmodified ring), based on an optical silicon-on-insulator microring resonator patterned with periodically arranged set of gold nanodisks, is presented and numerically verified in this chapter. It is shown that the periodic arrangement of nanodisks selects a single resonance from a wide set of ring resonator modes and removes mode splitting. Extraction of the waveguided electromagnetic energy into evanescent plasmonic modes enhances light–analyte interaction and increases device sensitivity to variation of refractive index up to 176 nm/RIU (about 2-fold increase compared to the unmodified ring), which is useful for sensor applications. Proof of the concept is presented by finite-difference time-domain simulations of a design readily practicable by means of modern nanotechnology.

3.2.1 Introduction

As established previously [5, 3, 11, P1], optical ring resonators have numerous advantages such as a high quality factor (Q) and a narrow resonance line width, which allows detection of small spectral resonance shifts due to minute changes of refractive index induced by trace amounts of analytes. However, if an induced resonance shift is large enough to overlap with a neighboring resonant mode position, the refractive index variation driven line-shift can no longer be unambiguously determined. In other words, when a resonance shift exceeds the free spectral rang, sensor performance is compromised. This critically limits the applicability of very

narrow FSR resonances such as in optical microring resonators, in which large spectral shifts cannot be reliably determined.

How could an optical microring resonator be modified so that it would have a neighboring mode spacing unlimited FSR? Here, it is achieved by engineering waveguide dispersion using metal nanodisks (MNDs) periodically arranged on top of a silicon-on-insulator optical ring resonator thereby creating a second-order $m = 2$ Bragg grating: $m\lambda_R = 2n_{eff}\Lambda$, where Λ is the period of MNDs, and n_{eff} is the complex effective refractive index of a particular mode at Bragg resonance wavelength λ_R. Interference between light coupled into the ring resonator and the Bragg-reflected waves results in suppression of most of the resonances that would be otherwise supported by an unmodified microring.

3.2.2 Results and discussion

To show the proof of concept, 3D FDTD simulations for TE polarization were performed. The simulated test structure, sketched in **Figure 41**, is a SOI optical ring resonator with 4.2 μm outer and 3.8 μm inner radii and a height of 0.22 μm. The bus waveguide is 0.22 μm high and 0.45 μm wide. The distance between the optical ring resonator and the bus waveguide is 0.13 μm. An array of equally spaced gold nanodisks that are 30 nm high and have 87 nm radii is added on top of the ring. The ring resonator was operating in a dielectric environment with a refractive index n_{env} of 1.33, corresponding to water.

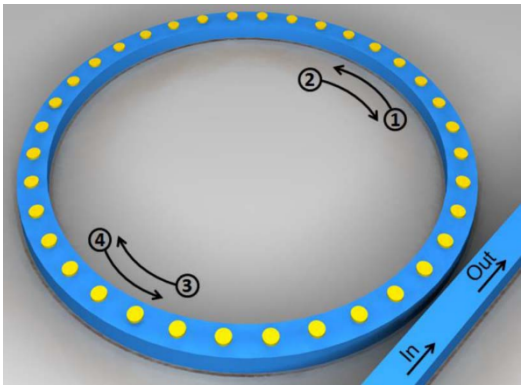

Figure 41. Visualization of SOI optical-ring resonator with implemented gold nanodisks. Directions 1 and 3 are launched wave, while 2 and 4 are counter-propagating waves (see text for details).

Numerical investigation of modal properties and sensor performance was conducted by first simulating a fully dielectric reference SOI microring with

shallow 2nd-order Bragg grating on the inner surface [58] without the MND array.

Light is coupled into the SOI optical ring resonator via a bus waveguide (port IN in **Figure 41**), and transmission spectra are measured at the OUT port. A typical transmission spectrum is shown in **Figure 42**. The structure supports multiple ring resonator modes at which resonant transmission dips occur. It is evident that resonant mode close to 1.575 μm is split into two (blue curve). This occurs due to a band-gap induced by the Bragg grating and is related to the appearance of even and odd standing-wave modes (E and O modes on **Figure 42**) as a symmetric and antisymmetric superposition of the counterpropagating traveling waves [59]. Addition of the gold MND array leads to formation of a single resonance dip, which coincides with the O-mode resonance peak of the unmodified ring. The O-mode survives due to having its intensity peaks localized between the MNDs and the resulting low overlap with the metal disks. Conversely, the E-mode is strongly suppressed due to the introduction of MNDs because its intensity peaks are localized directly underneath them. Other resonances that are supported by an unmodified resonator also dissipate while propagating through the microring due to scattering losses as observed for dielectric micro gear and micro flower disk resonators [60-62]. In the case of a MND decorated microring, this dissipation effect is further enhanced by excitation of surface plasmons and the resulting dissipation in the metal. In other words the device operates as a perfect filter — only a single ring resonator mode, which matches the MND introduced second-order Bragg condition [60, 62], (O-mode) is preserved, and mode splitting is removed.

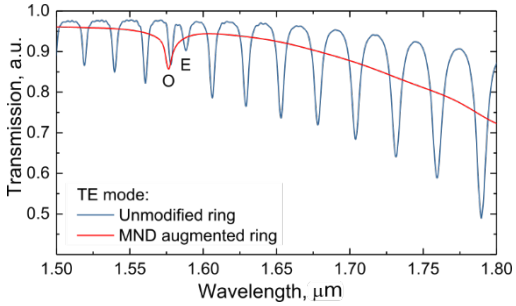

Figure 42. Transmission spectra. Transmission spectra of unmodified and Au MND-augmented SOI optical ring resonators at OUT port for TE polarization.

Position of the resonant peak depends on both the number of gold nanodisks (period of arrangement) and the overall perimeter of the ring resonator. In **Figure 43**, shifts of the solitary resonance peak with respect to the number of nanodisks (period) are illustrated. The real part of the n_{eff} for the resonant mode can be determined, which is shown to monotonically blue-shift and become narrower for a larger number of MNDs (the circumference of the ring resonator is kept fixed for all simulations). This blue-shift is the result of the 2nd-order Bragg grating period change, which in turn influences the phase matching conditions.

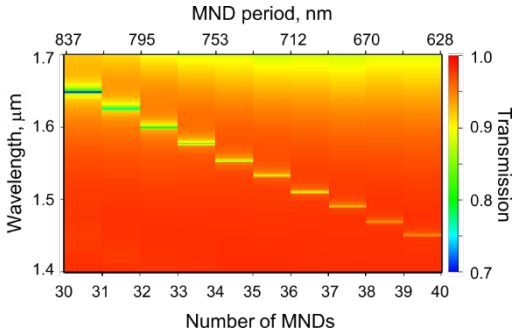

Figure 43. Dependence of the resonant frequency on the number (period) of gold nanodisks. Color represents transmission intensity.

The electric-field-intensity distribution of a resonant mode in a simulated optical ring resonator is shown in **Figure 44**a. It is evident that this mode is supported by the modified ring resonator, whereas off resonance (+10 nm), it is strongly suppressed (**Figure 44**b) and is unable to offset the damping due to excitation of localized plasmonic mode [63].

Light coupled into the ring (arrow 1 in **Figure 41** and **Figure 44**b) gets scattered due to interaction with the periodic MND array and gives rise to a counter-propagating wave (CPW) (arrow 2). Some of this reflected light is decoupled out of the ring back into to the bus waveguide and propagates toward the IN port. The remainder of the reflected electromagnetic radiation propagates counterclockwise (arrow 3), generating further reflections (arrow 4) along the way, which in turn can be decoupled back in to the bus waveguide as well as scattered out of the device plane by MNDs. As the cycle is repeated, the waveguided reflections interfere with the originally launched wave. If this interference is constructive, a resonant stationary O-mode with a periodic pattern of electric field intensity maxima localized between the MNDs is established.

In principle, the approach presented here would also work with a first-order m = 1 Bragg grating. The only difference is that a first-order Bragg grating creates a CPW only, whereas the second-order Bragg grating creates CPWs and scatters the light in a perpendicular out-of-plane fashion. However, a gold nanodisk-derived first-order Bragg grating configuration is less efficient at single-frequency filtering due to proximity-driven coupling between neighboring MNDs giving rise to a propagating plasmonic mode [64, 65].

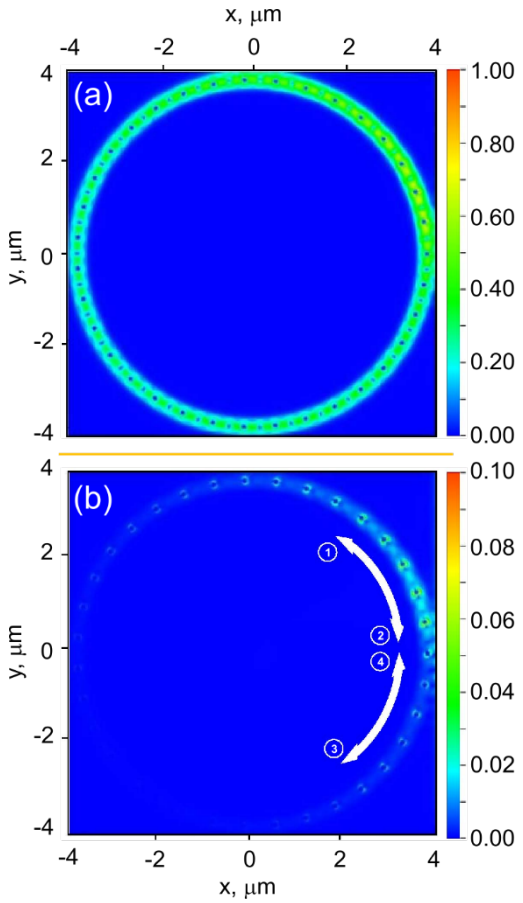

Figure 44. Electromagnetic field propagation. a, TE intensity at resonant frequency (35 gold nanodisks). **b**, TE intensity +10 nm off-resonant wavelength. The arrows 1 and 3 denote launched waves, and arrows 2 and 4 represent counter-propagating waves. The field profiles were taken in the XY plane at half height of gold nanodisks. Color represents intensity. The bus waveguide is vertical (light propagates along y-axis) and is at the right-side of the maps.

The size of the nanodisks is another key factor in determining the single-resonant frequency of the device. Simulation results presented in **Figure 45** indicate that when gold nanodisks have a 40 nm radius the device still works as an ordinary ring resonator; however, when the radii exceed ~70 nm, all other resonances become suppressed. This size-dependent effect is caused by the frequency shift of localized plasmonic modes supported by MNDs (which are recognizable around the edges of the disks in **Figure 44**). An instructive, although simplified, way of considering this plasmonic contribution is to describe it as a decrease of the real and an increase of the imaginary parts of the effective refractive index as the plasmonic resonance is shifted by changing MND geometry [66].

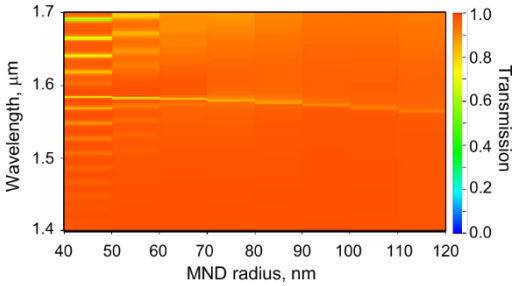

Figure 45. Dependence of the resonant frequencies and the appearance of ultra-wide FSR operation regime in an MND-decorated microring resonator as the gold nanodisk radii are increased (35 gold nanoparticles). Color represents transmission intensity.

Capability for the proposed device to operate even at extremely variable sensing environments was tested by simulating resonance shift with respect to the change of refractive index of the surrounding medium (bulk sensitivity). When refractive index is altered from $n_{env} = 1$ to $n_{env} = 2.6$, the corresponding device transmission spectra are shown in **Figure 46**a. The FSR of the resonant mode is proven to be terminated only by the bandwidth of the waveguide (mode cut-off). The total FSR of the proposed device is roughly ~200 nm, whereas for the corresponding unmodified microring with the same parameters, the FSR is only~20 nm. Furthermore, the MND-augmented ring resonator does not sacrifice sensitivity. As shown in **Figure 46**b, at moderate refractive index changes $n_{env} = 1.33$, typical for sensing waterborne analytes, resonator response shows excellent linearity. The simulated sensitivity of the proposed ring resonator device was found to be around 110 nm/RIU. At higher refractive indices in **Figure 46**c, $n_{env} = 2.32$,

the sensitivity is 242 nm/RIU due to the mode approaching the cut-off and delocalization of the mode field extending to external medium. The ultra-wide FSR average sensitivity is about 176 nm/RIU, which is a substantial increase (about 2-fold) over the value of~70 nm/RIU for an unmodified microring resonator. This sensitivity enhancement is attributed to the extraction of the electromagnetic energy from confinement in the high-index SOI waveguide into evanescent plasmonic modes supported by the nanodisks, where it can interact with the analytes more strongly.

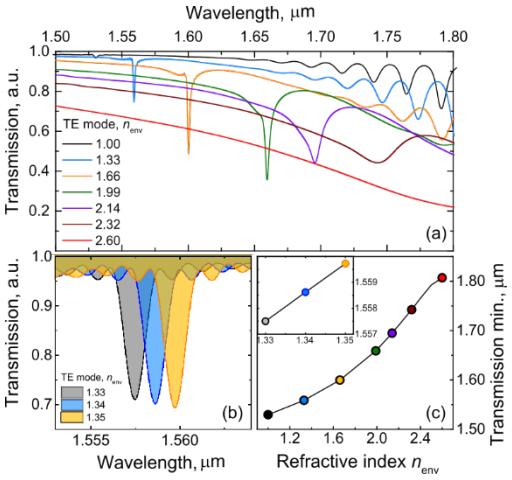

Figure 46 | Optical properties of ring resonator. a, The resonant mode shift due to large changes in refractive index of the surrounding medium (ring decorated with 35 gold nanoparticles). **b**, Resonant transmission dip shifts due to moderate n_{env} = 1.33 refractive-index modifications of the surrounding environment, typical when sensing water-soluble analytes. **c**, Spectral position dependence of the resonant transmission dip on the refractive index of the surrounding medium extracted from panel **a**. Inset displays an analogous sensitivity plot for panel **b**.

The simulated quality factor of a resonance at 1.577 μm was at $Q \approx 500$ for the unmodified microring, and decreases to $Q \approx 300$ after the addition of MNDs. However, even this increased linewidth is considerably narrower in comparison with plasmonic sensors whose extinction spectra are known to have excessively broad bands [67]. In addition, due to the efficient E-mode damping by MNDs [62], the mode splitting, which often introduces false-positive or negative bio-detection, is removed. This method is considerably simpler than some other proposed interferometric techniques [59].

3.2.3 Conclusions

In conclusion, systematic numerical study verifies the conjecture that MND arrays on a microring resonator create a novel ultra-wide FSR (increased by one order of magnitude) sensor platform; it is only limited by the bandwidth of the waveguide. Average sensitivity of the device is around ~176 nm/RIU with removed mode splitting in ultra-wide FSR and offers 2-fold improvement over the value of ~70 nm/RIU exhibited by an unmodified analogue. Filtering qualities of the resulting dispersive grating can be fine-tuned by varying the parameters of both, the ring, and of the nanodisk chain. Increasing the radii of the nanodisks was shown to blue-shift and attenuate the resonant mode.

Practical realization of this sensor is viable using current state-of-the-art electron and ion beam lithography for waveguide definition and a subsequent pattern overlay for MND fabrication via a lift-off [68]. Au nano-disks are an established bio-medical functionalization platform that makes the proposed design of a highly selective sensor auspicious for real life applications. Also, the proposed principle offers a novel approach for realization of broad-band spectral filters and, especially, for development of single-mode microring lasers operating in the ultra-wide mode hopping free range.

3.3 Air and dielectric bands photonic crystal microring resonator for refractive index sensing

The following chapter is based on article:
DOI: 10.1364/OL.41.003655
© The Optical Society. Reproduced with permission. All rights reserved

In previous two chapters theoretical results were shown. In this chapter experimental and numerical analysis of a fabricated microring resonator with an integrated one-dimensional photonic crystal fabricated on a silicon-on-insulator platform is presented and its applicability in bulk refractive index sensing is shown. The photonic crystal is formed by periodically patterned, partially etched cylindrical perforations, whose induced photonic bandgap is narrower than the range of measurable wavelengths (1520–1620 nm). Of interest is that the microring operates in both air and dielectric bands, and the sensitivities of the resonances on both edges of the bandgap were investigated. It is shown that a higher field localization inside the volume of the perforations for the air band mode lead to an increase in sensitivity.

3.3.1 Introduction

As a way of increasing the volume of interaction between the microring resonator mode field and the environmental medium it was suggested to introduce a one-dimensional photonic crystal inside the ring waveguide [13, 33]. The resulting reduction in Si volume and mode field confinement may lead to a lower quality factor (Q-factor) of the resonances. However, as it was shown in [69] and later in [70], introducing high dispersion inside the cavity material via photonic crystal may lead to a dramatic increase in Q-factor of the cavity resonance. For wavelengths close to the edge of the photonic bandgap group velocity approaches zero and spectral narrowing of resonance lines occurs.

The photonic bands above and below the photonic bandgap can be distinguished by where the energy of their modes is concentrated: in the low or high refractive index regions. Correspondingly, the modes on the respective sides of the bandgap are usually denoted as air band (higher frequency) and dielectric band (lower frequency) [71].

Recently the applicability of microring resonators with integrated one-dimensional photonic crystals (MRR-PhCs) was shown in applications such

as localized strain sensing [72], optical filtering [73], narrow-band mirror [74], lasers [75], and optical vortex generation [58].

Here, a SOI MRR-PhC applied in bulk refractive index sensing is presented. The operation of the previously reported MRR-PhC was limited exclusively to the dielectric or air band [13, 76, 77]. The novelty of this design is that it operates in both bands and can simultaneously measure sensitivities of resonance modes on both edges of the bandgap. It is shown that due to higher field localization inside the perforations, sensitivity of the air band mode to variations in surrounding refractive index is higher than for the dielectric band mode.

While the results presented in this work are for bulk refractive index sensing, in which the extension of analyte material is larger than the extension of the guided-mode evanescent field, the device could potentially be used in other applications. Different sensitivities of air and dielectric band modes could be employed in surface sensing to simultaneously monitor surface layer thickness and refractive index, or simultaneous bulk refractive index and temperature measurements, where previously dual-polarization (TE and TM) ring resonators were used in order to associate two unknown quantities with two measurement results (resonance line shifts for TE and TM polarizations) [78, 79]. Thus, eliminating the need for dual polarization excitation and discrimination between TE and TM resonance lines in the measured transmission spectra.

Another attractive feature of the presented sensor is that the photonic bandgap could provide a reference point for sensing refractive index changes whose induced resonance wavelength shift exceeded spectral spacing between resonances [P2], as it helps to identify and follow MRR-PhC resonance modes during sensor operation.

3.3.2 Results and discussion

The geometry of the MRR-PhC under investigation is shown in **Figure 47**. Five holes of the same size and periodicity as the holes forming the one-dimensional photonic crystal inside the microring were added to the bus waveguide to ensure good evanescent coupling between the bus waveguide and the microring resonator. The scanning electron microscopy image of a lithographically fabricated representative MRR-PhC is shown in **Figure 48**. The geometrical parameters of the microring resonator structure are summarized in **Table 1**.

The one-dimensional photonic crystal was integrated onto a 4000 nm radius microring resonator structure constructed of a waveguide with width

and height of 400 nm and 240 nm, respectively. The one-dimensional photonic crystal was formed by periodically placing cylindrical perforations. The device was fabricated at ePIXfab (Imec, Leuven) using a standard complementary metaloxide semiconductor process [P2], with the possibility of having three silicon etch depth levels: 240, 150, or 70 nm. The characterization setup allowed to measure transmission spectra in the wavelength window ranging from 1520 to 1620 nm. Therefore, the photonic crystal design was chosen so that it would form a photonic bandgap bounded within this wavelength region. Thereby the number of cylinders was fixed to 72, resulting in the period Λ = 350 nm, for which the first order Bragg wavelength is equal to 1550 nm.

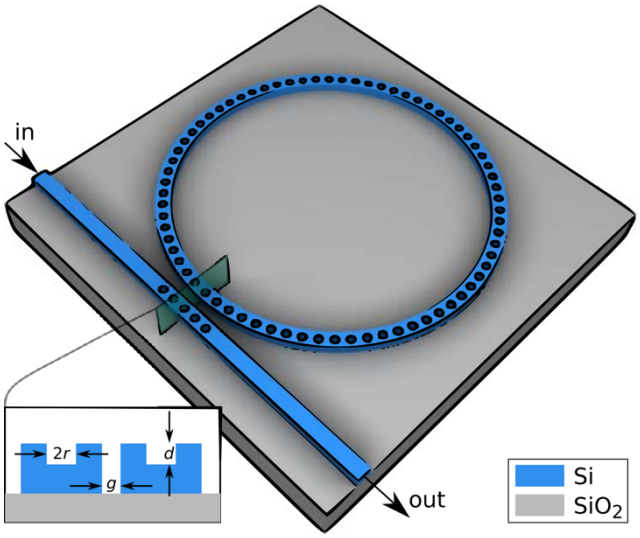

Figure 47. Geometry of the microring resonator with an integrated photonic crystal (MRR-PhC). Inset shows cross section of the evanescent coupling region. In the inset r denotes hole radius; d, hole depth; and g, coupling gap.

Parameter	Numerical Value
Middle radius	4000 nm
Ring waveguide width	400 nm
Hole radius r	70 nm
Hole depth d	70 nm
Number of holes	72
Hole periodicity Λ	350 nm
Bus waveguide width	400 nm
Coupling gap (g)	180 nm
Silicon thickness	240 nm

Table 1. Geometrical parameters of MRR-PhC.

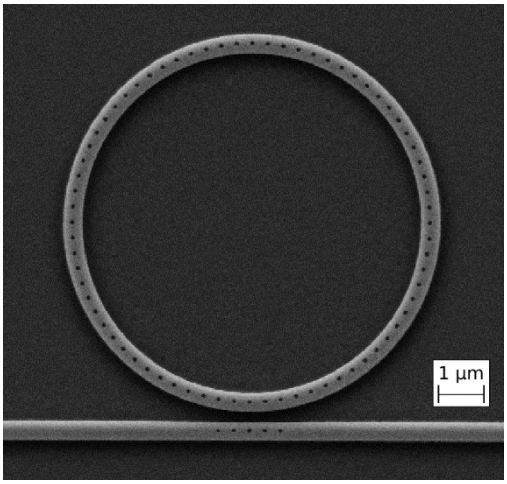

Figure 48. Scanning electron microscopy image of a fabricated MRR-PhC.

Numerical simulations were conducted using a free finite difference time-domain Maxwell's equation solver software package MEEP [51]. MEEP was used for both whole structure and photonic band structure simulations. For band structure simulations a transformation optics approach was used to convert a single-period segment of the microring from a bent to a straight one by correspondingly altering the material properties [80]. To increase the accuracy of numerical simulations subpixel smoothing, available in MEEP [81], was used for full ring simulations (10 nm grid step size). In all simulations and experimental measurements TE-polarized light (electric field parallel to the device plane) was used.

Simulation results for bandgap width as a function of hole radius at various hole depth values are presented in **Figure 49**. As the air fraction introduced by the holes increases, so does the photonic bandgap width. However, the decrease in the bandgap width visible in **Figure 49** for hole radius values more than 120 nm is a result of the structure geometry approaching that of a conventional waveguide, but with a smaller waveguide height. The experimentally attainable range of wavelengths for the characterization setup is 100 nm. To have at least one resonance on one side of the photonic bandgap and several on the other side the maximum width of the photonic bandgap was limited to 45 nm or less. Therefore, for a hole depth of 70 nm the range of hole radii is <80 nm. When the hole depth is 150 nm their radius should be <50 nm, and for 240 nm depth it should be < 45

nm. However, a small hole radius can result in poor sensor performance due to the analyte's inability to expel the air trapped within and fill them [40]. Therefore, an optimal hole radius of 70 nm at a hole depth of 70 nm was chosen. For theoretical analysis and custom fabrication conditions different values could be considered, with shallower holes making analyte accommodation easier, however, at the cost of to some extent losing the benefit from reduced mode field confinement.

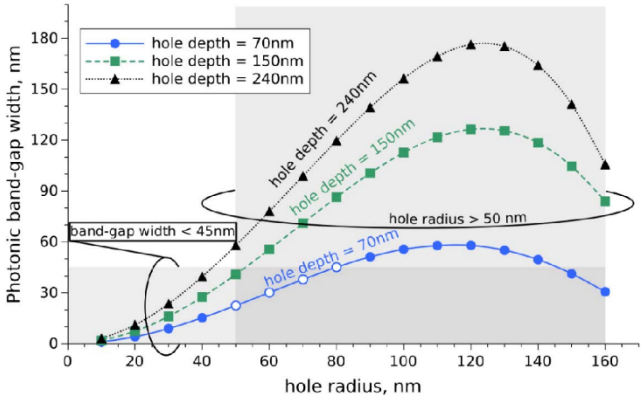

Figure 49. Photonic bandgap width as a function of the hole radius for three-hole depth values: 70, 150, and 240 nm. Gray area represents limitations imposed by fabrication process and measurement setup. Hole radius must exceed 50 nm and bandgap width must be thinner than 45 nm. Intersection of two areas are the available designs: hole depth of 70 nm and hole radius in the range 50–80 nm.

The simulated band diagram of the photonic crystal inside the microring resonator is presented in **Figure 50Figure *49***. The bandgap extends from roughly 1520 to 1560 nm. An additional bandgap is also established in the wavelength region from 1110 to 1120 nm. The electric field energy density distributions of each mode presented in the mode diagram are also shown in **Figure 50**. It is evident that energy of the air band is mostly confined inside the hole region (region 2 in **Figure 50**), in stark contrast to the dielectric band modes mostly confined in Si (region 1 in **Figure 50**). The fraction of mode energy inside the environmental medium for the air band mode is 0.110, whereas for the dielectric band mode it is 0.104. However, as we move away from the bandgap edge, from slow light to traveling wave regime, the mode having larger wavelength (lower frequency) becomes less confined and more sensitive to environmental changes.

Transmission spectra of the microring resonator were measured by exposing the device to four different environmental materials: methanol (n =

1.3174), ethanol (n = 1.3522), isopropanol (n = 1.3661), and glycerol (n = 1.4571). Refractive index values at the free-space wavelength of 1550 nm are taken from [82]. Silicon n used in simulation was 3.476 [83], whereas the n of the underlying SiO2 was assumed to be 1.444 [84]. The measurements are carried out on a temperature stabilized setup like [85] excited with TE polarization using vertical fiber grating couplers. Measurements for air environment were not included since the coupling gap (**Figure 47**) was specifically chosen for environment with n = 1.3 or higher, thus resulting in low coupling efficiency and low extinction ratio in air environment. The two quantities of interest in bulk refractive index sensing applications are sensitivity (S) and Q.

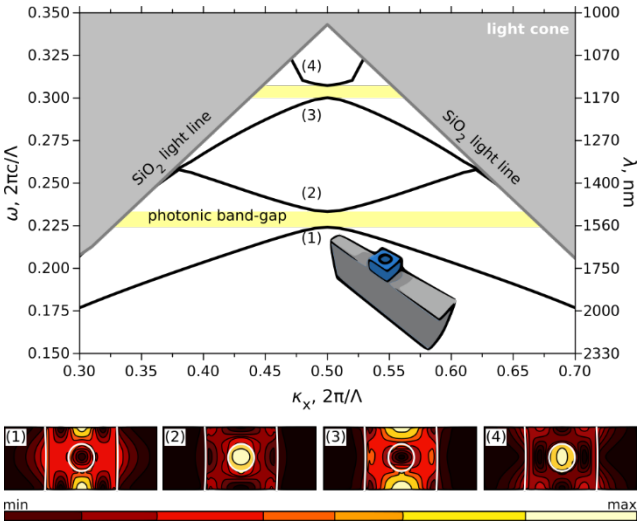

Figure 50. Band diagram of holey bend waveguide. (1) and (3) denote dielectric bands, (2) and (4) denote air bands. The bottom panels show the distribution of electric field energy density of all four bands at $k_x = 0.49$.

The numerical simulations of the full microring structure with different environmental materials showed that the expected sensitivity of the dielectric band mode closest to the bandgap edge is 94.9 nm/RIU, and the sensitivity of the air band mode closest to the bandgap edge is 99.7 nm/RIU, 5.2 nm/RIU higher than that of the dielectric band mode. It is also worth mentioning that bulk refractive index sensitivity generally increases with longer wavelengths, and here the effect of mode field localization inside the holes overcomes this effect. Measured transmission spectra of the device are shown in **Figure 51**. A bandgap approximately 35 nm in width is clearly

visible in the transmission spectra, replicating that of the numerical simulations in both its width and position with good accuracy.

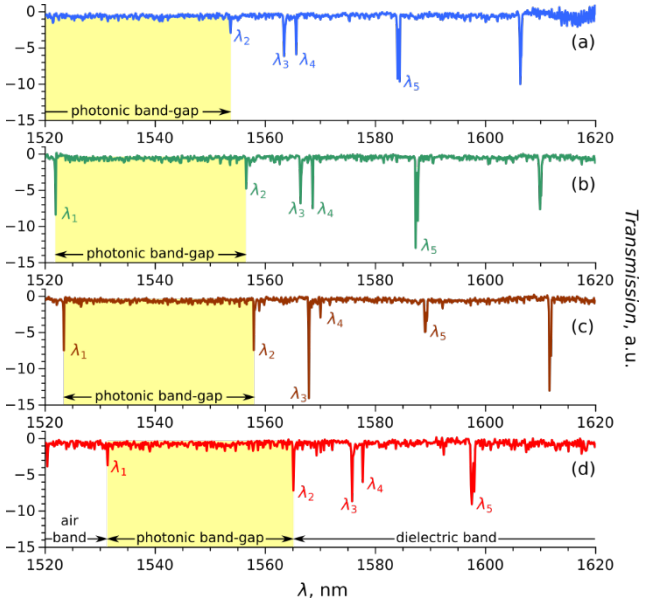

Figure 51. Measured MRR-PhC transmission spectra for different environmental mediums. a, Methanol, n_{env} = 1.31. **b**, Ethanol, n_{env} = 1.35. **c**, Isopropanol, n_{env} = 1.36. **d**, glycerol, n_{env} = 1.45. The photonic crystal induced bandgap extends from λ_1 to λ_2. λ_1 is the resonance in the air band: λ_2, λ_3, λ_4, and λ_5 are resonances in the dielectric band.

Resonance wavelength positions obtained with different environmental materials are summarized graphically in **Figure 52** from both experimental measurements and numerical simulations.

We can see that experimentally observed resonance shifts associated with changes in the refractive index of the surrounding material are 10nm/RIU lower than predicted by numerical simulations. To investigate this further several numerical simulations were performed in which a given fraction of the microring surface was left unexposed to the analyte material. It was determined that a sensitivity decrease of 10 nm/RIU results when about 25% of the microring surface is not covered with analyte material. However, deviation of the geometry of the fabricated device from the ideal one could also lead to a similar discrepancy.

Measured Q factors of the resonances were as follows (in the spectra shown in **Figure 51**d): 10432 for λ_1, 11325 for λ_2, 7124 for λ_3, 13085 for λ_4, and 7200 for λ_5.

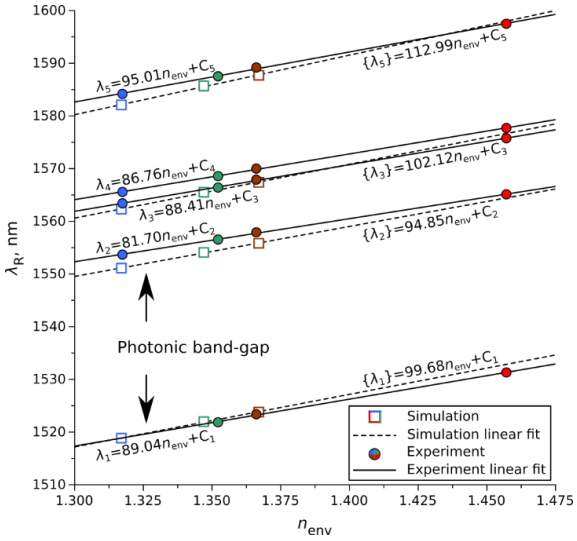

Figure 52. Positions of the MRR-PhC resonances as a function of environmental refractive index. Line equations obtained via linear least-squares fit, for experimental measurements denoted as λ_i, numerical simulation results as λ_i. The slope of each line corresponds to the sensitivity in (nm/RIU) units.

The experimentally measured transmission spectra show a couple of resonant mode splittings: λ_3 and $\lambda 4$ correspond to the same mode; furthermore, the resonance dip of $\lambda 5$ mode is likewise split (**Figure 51**). The causes of this splitting can be numerous: reflections in the coupling region from the bus waveguide, surface roughness of the microring resonator, slightly different periodicity, and size of the holes — all of which result in backscattering of propagating waves [86]. Thus, a coupled mode system of clockwise and counterclockwise propagating modes is formed, manifesting itself in the transmission spectra as mode splitting [28].

3.3.3 Conclusions

In summary, a novel microring resonator with an integrated one-dimensional photonic crystal, formed by partially etched cylindrical perforations, was demonstrated. It was shown that due to the higher mode field localization inside the hole region of photonic crystal, the air band has higher bulk refractive index sensitivity.

3.4 Enhanced sensitivity and measurement range SOI microring resonator with integrated one-dimensional photonic crystal

The following chapter is based on article:
DOI: 10.1364/JOSAB.34.000750
© The Optical Society. Reproduced with permission. All rights reserved

In previous chapter fully through Si etched perforations, which are rather easy to process due to circular nature, and micro ring resonators with gold nanodisks, which require two lithographical steps to make, were demonstrated. The latter, however, are 2D modifications. In this chapter a silicon-on-insulator microring resonator based refractive index sensor with 3D perforations having enhanced sensitivity and measurement range is presented. Both improvements are achieved by integrating a 1D photonic crystal inside the microring waveguide. A photonic crystal is formed by periodically patterning, partially etching the rectangular perforations. Sensor performance is numerically analyzed for various combinations of perforation depth and length, each of which maintains a constant resonance wavelength. Findings presented here show that, while deeper perforations result in a larger bulk refractive index sensitivity, the optimal design exhibiting the smallest limit of detection can be obtained at some intermediate value, depending on the leading term in sensor resolution. In addition to theoretical analysis, an experimental demonstration of a fabricated microring resonator with 120 nm height perforations is presented.

3.4.1 Introduction

In this work a microring resonator designed specifically to enhance sensitivity and increase the measurement range is presented. Both improvements are achieved via integration of a 1D photonic crystal inside the microring waveguide. The photonic crystal is formed by periodically patterned, partially etched rectangular perforations. It is designed to induce a photonic bandgap with an edge at the lower part of the measurable wavelength window (1520–1630 nm in our measurement setup). Thus, the position of the photonic bandgap can be used as a reference point during sensor operation, eliminating the limitation imposed by FSR.

Here, the analysis is limited to bulk (or volume/ homogeneous) refractive index sensitivity. In this sensing scheme, the volume of analyte material extends far beyond the range of the mode evanescent field. And, while the bulk refractive index sensitivity has been shown to increase with longer

perforations (or smaller duty cycle) [87], the effect of perforation depth on the interaction between mode evanescent field and surrounding medium, to the best of our knowledge, has not been previously analyzed. We note that the proposed structure could also be used in a surface sensing scheme, where effective mode index change is induced by the dielectric layer of thickness, which is comparable with that of evanescent field. While single mode operation provides a limited amount of information (thickness if the refractive index is known, or converse), several strategies have been proposed to measure both surface layer thickness and its refractive index [P3, 78, 88].

The possibility to fabricate waveguides with different perforation depths opens a new degree of freedom in device design. It was previously utilized in devising polarization splitters – rotators [89] and grating couplers [90]. Numerical simulations of microring resonators with 1D photonic crystals are performed for varying perforation depths to analyze how sensors characteristics are affected. It is shown that deeper perforations result in higher bulk refractive index sensitivity. However, another important characteristic of a sensor, limit of detection, can obtain its minimum at some intermediate value, dependent on which mechanism dominates the sensor resolution.

In addition to theoretical analysis, the measurement results of a fabricated SOI microring resonator sensor in which a photonic crystal is formed by 120 nm depth rectangular perforations are presented.

3.4.2 Structure design

The general structure of the analyzed SOI microring resonator is shown in **Figure 53**. The photonic crystal inside the microring resonator is formed by periodically patterned, partially etched rectangular perforations. The depth of the perforations is denoted by d and their length l. In all simulations, the microring radius (r_{Ring}) is set to 5100 nm, microring waveguide width (w_{Ring}) is 410 nm, bus waveguide width (w_{WG}) is 380 nm, coupling gap (g) is 120 nm, and total height of silicon (h_{Si}) is 240 nm. The chosen coupling gap ensures microring resonator operation close to critical coupling [5, P1]. All parameters are well within the limits of fabrication requirements. The number of perforations was chosen to be 80, which results in a period of 400 nm. A silicon n used in simulation was set to 3.4757 [83], SiO2 n was set to 1.4440 [84]. Excitation polarization in both theoretical model and manufactured structure is TE.

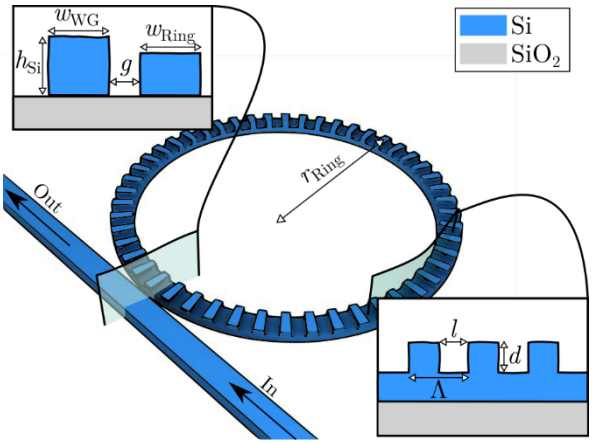

Figure 53. Geometry of the perforated microring resonator. h_{Si} denotes silicon thickness, w_{WG} — bus waveguide width, w_{Ring} — ring waveguide width, g — coupling gap, r_{Ring} — ring radius, d — perforation depth, l — perforation length and Λ — period.

Numerical simulations of a full microring structure were conducted using a fully 3D FDTD method implemented in a noncommercial software package Meep [51]. Band diagram calculations on a one period segment of a photonic crystal were modeled using a fully vectoral, open-access, eigen mode solver MPB [91]. The grid step size used in 3D FDTD simulations was 20 nm, and in-band diagram calculations were 10 nm. Also, to increase accuracy of numerical simulations, subpixel smoothing [81] was used.

Three quantities of interest in sensing applications were measured: bulk refractive index sensitivity ($S_b = \Delta\lambda_{res}/\Delta n_{clad}$ [92]), quality factor of the resonance Q, and the limit of detection (LoD).

The LoD is the minimal refractive index change that a sensor can detect [93], which can be expressed as LoD = R/S_b; (1) where R stands for sensors resolution. It can be expressed as $R = 3\sqrt{\sigma_{SNR}^2 + \sigma_{Temp}^2 + \sigma_{\lambda}^2}$, where the first term is a standard deviation of spectral location due to signal-to-noise ratio (SNR), the second term is a result of thermal fluctuations, and the third term depends on the available wavelength resolution. σ_{SNR} can be expressed as $\sigma_{SNR} = \frac{\lambda_{res}}{4.5QSNR^{0.25}}$ and σ_{Temp} as $\sigma_{Temp} = S_T\sigma_T$, where S_T is the thermal sensitivity and σ_T is the standard deviation of temperature.

Some authors define the limit of detection as $\lambda_{res}/(QS_b)$ [34, 92, 94]. However, this expression is simply proportional to LoD if only the σ_{SNR} term in resolution is considered. Another common practice is to include only σ_{λ}.

But, as stated in [95], one cannot simply assume that the sensor resolution is identical to the discretization limit of one of the components of the system. Thus, in this analysis all three terms are included.

We first analyze how perforation depth (d) and length (l) affect resonant wavelength position closest to the edge of the photonic crystal induced bandgap. For this we performed a series of MPB simulations to obtain dispersion curves, containing a relationship between the wave vector (κ) and angular frequency (ω). This relationship, together with the microring resonance condition $m\lambda_{res} = 2\pi R_{ring} n_{eff}$ [3], was used to obtain the resonance wavelength value. The resulting dependence of the resonance wavelength on d and l is shown in **Figure 54**.

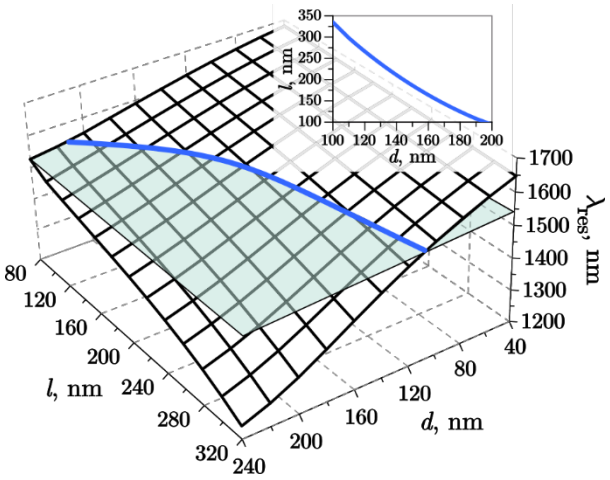

Figure 54. Resonance wavelength of mode closest to the photonic bandgap as a function of perforation length (l) and depth (d). Transparent plane cuts surface at λ_{res} = 1540 nm.

While waveguide bending was neglected in MPB simulations, comparison with full ring 3D FDTD simulations revealed that results are in satisfactory agreement. This in turn suggests that, for a 5100 nm radius microring, the effect of bending on resonance frequency position is small.

Assuming that resonance wavelength shift is toward longer wavelengths and that our measurement setup allows to measure in a 1520 — 1630 nm wavelength window, a resonance wavelength window is chosen close to the lower edge, 1540 nm. Thus, the photonic bandgap below 1540 nm can be used as a reference point during sensor operation, giving a measurement range of 80 nm. If the direction of the resonance wavelength shift is not known beforehand, then the bandgap edge should be chosen at the middle of

the measurable wavelength window (1575 nm). From the surface plot intersection with the plane λ_{res} = 1540 nm, the relationship between d and l, for which the resonance closest to the photonic bandgap edge is situated at 1540 nm, was obtained. This relationship was approximated using the exponential function $l(d) = 1223.4e^{-0.0127d}$.

The band diagram for one set of such values (for which the actual microring resonator was fabricated) is shown in **Figure 55**. The photonic bandgap can be seen to extend from 1480 to 1540 nm. The sensor depicted here operates in the lower frequency (or dielectric) band mode [P3].

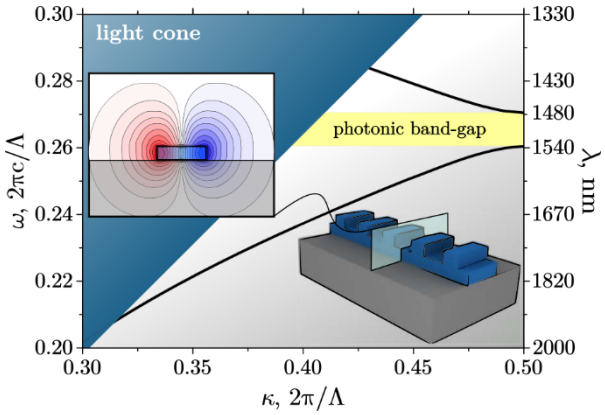

Figure 55. Band diagram of a periodic segment forming a 1D photonic crystal inside the microring resonator (d = 120 nm). Inset shows distribution of electric field vector component perpendicular to the direction of propagation.

Analysis of the sensor performance was performed only with respect to the perforation depth and length (**Figure 53**). Waveguide height is usually defined by the fabrication process and cannot be changed; width was chosen to correspond to single-mode quasi-TE operation. The period and coupling gap were fixed not alter the Q-factor and bulk refractive index sensitivity; consequently, the limit of detection would go well beyond the scope of this article [96, 15, 16].

3.4.3 Sensor performance

Next the microring resonator sensor performance dependence on perforation depth and length values were investigated, ensuring resonance positions at 1540 nm.

The bulk refractive index sensitivity (S_b) dependence on perforation depth is shown graphically in **Figure 56**a. It is visible that increasing the depth of

the perforations results in a higher S_b. This result can be explained by a larger mode field overlap with cladding material. The overlap dependence quite closely mimics the one of S_b. Hence, this is the evidence that the mode field overlaps more with the surrounding media in strongly perforated microrings.

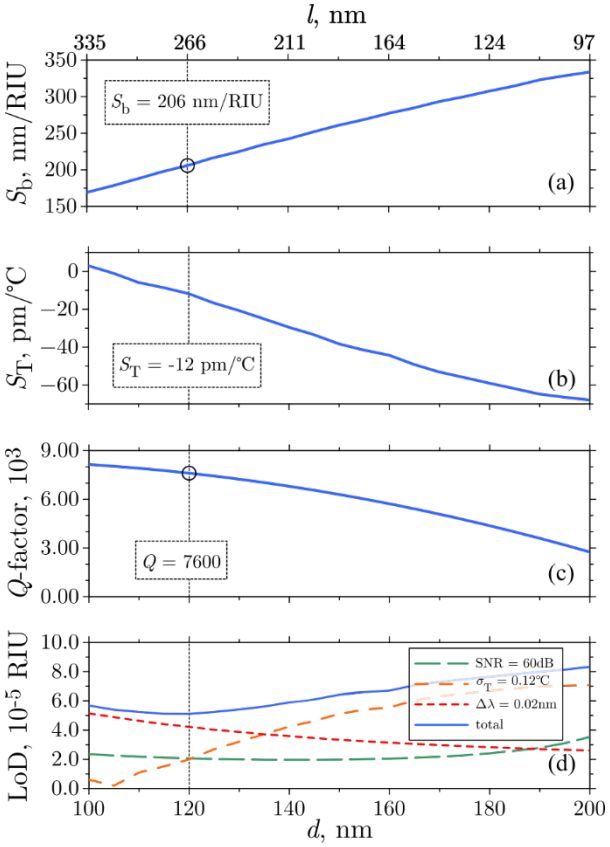

Figure 56. Perforation depth (with a corresponding perforation length to maintain the 1540 nm resonance position) dependences of key microring sensor parameters. a, Bulk refractive index sensitivity. **b**, Thermal sensitivity. **c**, Q-factor. **d**, Limit of detection, for different dominant factors: SNR of 60 dB, temperature variation of 0.12 deg, spectral resolution of 0.02 nm, and all together.

The spectral deviation due to thermal fluctuations was determined by simulating thermal sensitivity of the device and multiplying it by the assumed standard deviation in temperature. Thermal sensitivity was determined to increase with increasing perforation depth, as shown in Fig. **Figure 56**b, although it is negative because the thermo-optic coefficient of

liquid (ethanol used in simulations, but the same holds for water) is negative and larger than the thermo-optic coefficient of silicon in its absolute value [97]. It was observed that a thermal sensitivity of zero can be obtained for *d* of approximately 103 nm, which is an attractive feature for designing sensors with a focus on thermal stability. Due to further decrease of mode field overlap with cladding material at smaller values of perforation depth, the thermo-optic coefficient of silicon starts to dominate effective index change, and thermal sensitivity becomes positive.

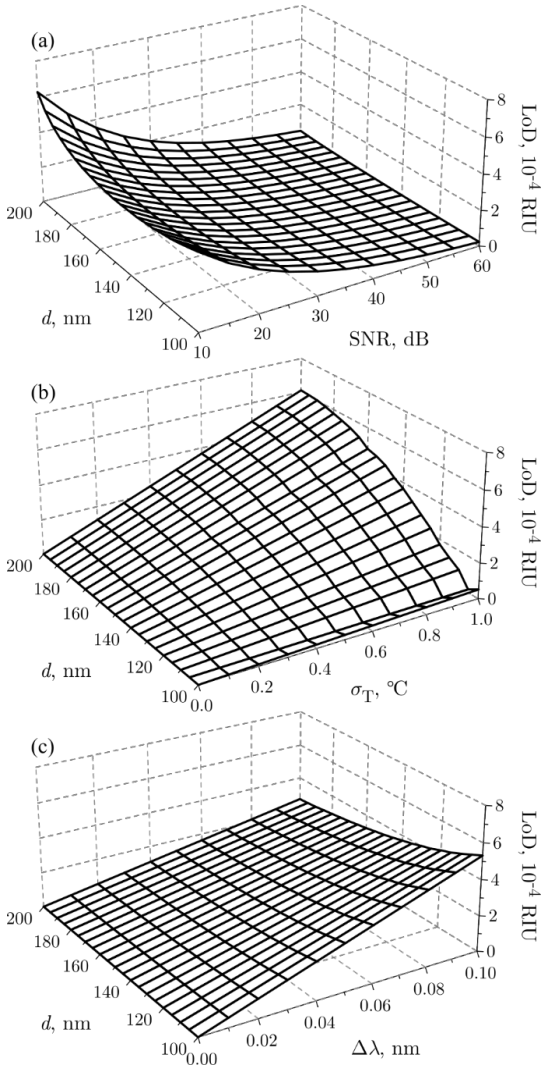

Figure 57. LoD from various contributions. a, SNR, varying from 10 to 60 dB. **b**, σT and **c**, Δλ.

The effect of a larger mode field extension into the cladding material results in lower Q factor values of deeper perforations, as shown in **Figure 56**c. The vertical lines at d = 120 nm denote the perforation depth value for which a microring resonator sensor was fabricated. Simulations suggest a S_b value of 206 nm/RIU (refractive index unit) and a Q factor of 7600. Contrary to the microring resonator sensor with partially etched cylindrical perforations [P3], the partially etched rectangular perforations show a two-fold increase in the bulk refractive index sensitivity (from 110 nm/RIU [P3] to 207 nm/RIU).

The limit of detection exhibits a more complex dependence (**Figure 56**d). Cases when only one term contributes to the LoD resolution are presented. And, when all three terms are considered, the smallest LoD value is obtained for d close to 120 nm.

However, the location of smallest LoD value depends on exact contribution from each term. To analyze this further, the LoD is calculated for each term in a range of their values. The results are presented graphically in **Figure 57**.

SNR influence on LoD depends on S_b and the Q factor. Because one increases with increasing d and the other decreases, minimal LoD lands somewhere at the intermediate value of perforation depth. This might be better observed in **Figure 56** d.

Last, $\Delta\lambda$ effect **Figure 57**c provides the least amount of new information, as it simply mirrors the dependence of S_b on perforation depth. Taken all together, we can summarize that, when considering LoD, some analysis must be performed to determine what form of perforation is most suited and which effect has the largest influence on a sensor's resolution.

3.4.4 Fabricated microring resonator sensor

A perforated microring resonator was fabricated on an SOI platform at ePIXfab (Imec, Leuven) using a standard CMOS process. Scanning electron microscopy images of the fabricated device are shown in **Figure 58**.

To test the sensor's performance, transmission spectra were measured with four different cladding materials: methanol (n = 1.3174), ethanol (n = 1.3522), isopropanol (n = 1.3661), and glycerol (n = 1.4571). Refractive index values at the free space wavelength of 1550 nm for all four materials are taken from [82]. Measured wavelength range was 1520–1630 nm. Refractive indices of all the materials were assumed to be uniform in this range.

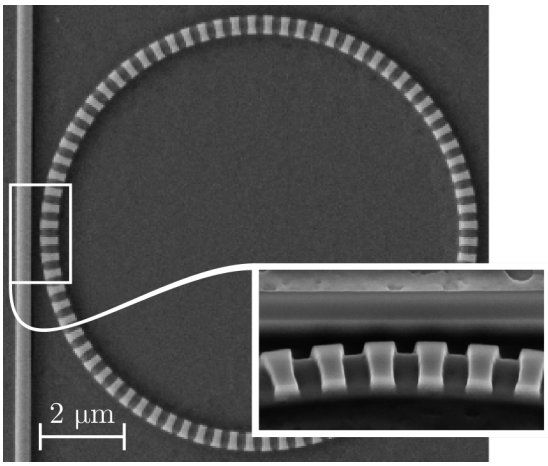

Figure 58. Scanning electron microscopy image of the fabricated microring resonator. Inset shows enlarged view of coupling region between bus and microring waveguides.

Measured resonance wavelength positions were fitted using linear least squares to a straight line in the form $\lambda_{res}(n_{clad}) = C + S_b n_{env}$, where the slope of the line is bulk refractive index sensitivity. Measured transmission spectra of the microring resonator are shown in **Figure 59**a. Compared with the plot shown in **Figure 59**b, which shows transmission spectra obtained via 3D FDTD simulations, we can conclude that a good agreement between measurements and simulation was obtained. However, resonances λ_2 and λ_4 from measurements do not correspond to any of the resonances in numerical simulation spectra. We expect those resonances to be a result of mode splitting [86, 98] due to ring waveguide sidewall roughness and/or imperfections in photonic crystal structure. Also, the extinction ratio (ER) in measurements was higher (19 dB) than in numerical simulations (12 dB). This disagreement can be accounted for by minute deviations in the coupling gap of the fabricated device (**Figure 53**). It should be noted that FSR compression from 22 to 7 nm near the bandgap is expected due to strong dispersion induced by the photonic crystal.

As the refractive index of the cladding material is increased by changing the surrounding medium, resonance wavelength positions shift toward longer wavelengths. This shifting for all measured surrounding mediums is summarized graphically in **Figure 59**c. Each line is given a fitted linear equation with bulk refractive index sensitivity values. An experimentally obtained S_b value of resonance closest to the photonic bandgap λ_0 is 207.7

nm/RIU, which is in good agreement with numerical simulations using MPB (206 nm/RIU, **Figure 56**a) and 3D FDTD (214 nm/RIU).

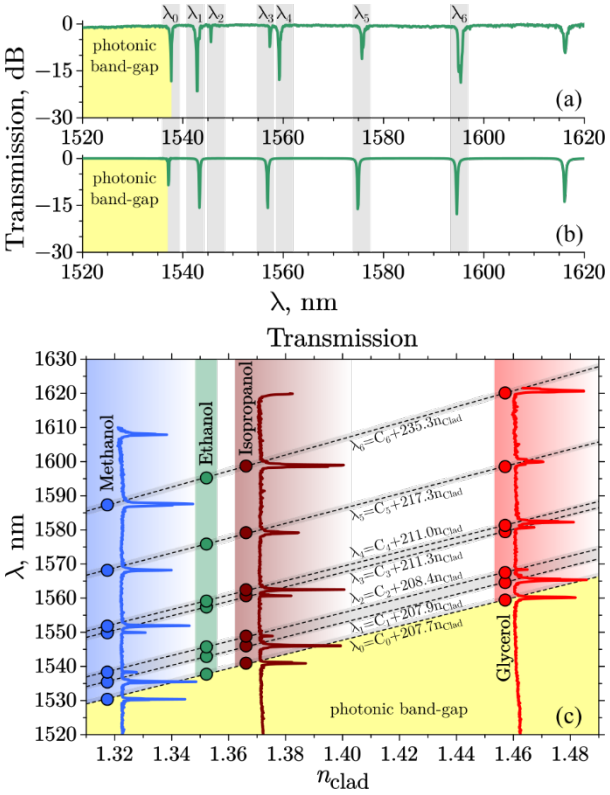

Figure 59. Transmission spectra of the microring resonator embedded in methanol. a, Experiment. **b**, Simulation. **c**, Resonance wavelength position and transmission spectra at various cladding materials.

The maximum resonance wavelength shift that can be measured with a fabricated resonator is 80 nm. With a bulk refractive index sensitivity of 207.7 nm/RIU, this gives a maximum measurable refractive index change of 0.385 RIU.

The quality factor of the resonances λ_0 shown in **Figure 59** is Q = 2600 based on measurement and Q = 7600 as deduced from 3D FDTD simulations (**Figure 56**c). The smaller value of a Q in measurement can be attributed to the same reasons as mode splitting (sidewall roughness and irregularities in photonic crystal) and additionally to the fact that, in numerical simulations, absorption of cladding material was not taken into account. Assuming an SNR of 30 dB and temperature deviation of 0.12 deg, the limit of detection of a fabricated microring resonator sensor is 4.5×10^{-4} RIU.

3.4.5Conclusions

In conclusion, we presented an analysis of a microring resonator with an integrated 1D photonic crystal for enhanced sensitivity and measurement range. The perforation-induced photonic bandgap can be used as a spectral reference to overcome limitations imposed by the FSR. Furthermore, we showed that, by adjusting perforation depth, the limit of detection can be minimized, depending on considerations of the leading factor determining sensor resolution. Numerical analysis was verified by experiment on a fabricated structure using organic solvents with different refractive indices. variable etch-depth features add an additional degree of freedom to the design and optimization of micro ring resonator sensor devices, as they can be used to control mode exposure to the surrounding medium as well as the total effective refractive index.

3.5 Microring resonator with perforated circular grating for enhanced sensing

The following chapter is based on article:
DOI: 10.35848/1347-4065/ab9232
© IOP Publishing. Reproduced with permission. All rights reserved

As discussed before, micro ring resonators can encounter some referencing issues. To overcome that gold nanodisks were suggested (section 3.2). However, due to difficult processing an alternative approach is shown.

In this chapter we suggest that implementation of circular second order Bragg grating into silicon-on-insulator microring resonators increases the light-matter interaction strength. Introduction of a specifically tailored grating changes the quality factor of a selected resonance and modulates the losses of the system, leading to the presence of only longitudinal resonant air and dielectric Bloch modes. This phenomenon can be harnessed for the development of a self-referenced sensor that is immune to the changes in ambient temperature. The recent results on numerical modeling, lithographic fabrication, and characterization of perforated microring resonators are presented.

3.5.1 Introduction

The possibility to fabricate microrings with different perforation depths and arrangements opens a new degree of freedom in device design. The loss-modified microring resonator can be created by integration of a second order Bragg grating that allows for control of leaky mode radiation losses, ejected out of the device plane. Modulation of a microring resonator by a periodic chain of Au nanodiscs thereby was able to filter out photonic modes of mismatched periodicity out of a SOI ring, enhancing sensitivity and free spectral range (FSR) of sensing performance [P2]. In this work, a fully dielectric microring resonator with a 2^{nd} order annular Bragg grating, designed specifically to enhance sensitivity and increase the FSR of measurements is presented. It exhibits similar effects as predicted in metal nanoparticle decorated designs [P2], however, here it is realized in SOI without introducing excessively lossy metals or performing multiple cumbersome lithography steps.

3.5.2 Methods

Numerical simulations of perforated microring structures were conducted using FEM [P1] and FDTD method [99, P6]. The perforated microring resonators were fabricated on SOI platform at ePIXfab (Imec, Leuven) using a standard CMOS process by deep ultraviolet (DUV) lithography and by electron beam lithography (EBL) at Melbourne Centre for Nanofabrication as well as at the Nanofabrication Facility at Swinburne University of Technology in Australia [100]. The experimental characterization of microrings was performed in the wavelength window 1520-1630 nm using a measurement setup (depicted in **Figure 34**) equipped with a TE polarized tunable telecom continuous wave laser coupled into the integrated SOI waveguide devices through vertical grating couplers via a lensed fiber [101]. The transmitted light is likewise collected through a fiber via grating couplers at the output ports and passed on to a telecom wavelength InGaAs detector. Alignment of coupling fibers is controlled by means of a microscope and a precision positioning stages.

3.5.3 Results

The structure under consideration is a loss-modified microring resonator with an integrated 2nd order Bragg grating (**Figure 60** a, b), introduced to increase the light-matter interaction with the surrounding medium and to attain control over the supported modes. The circular grating elements were placed asymmetrically, on the inner side of ring resonator, to reduce the modal overlap with confined radiation and thereby to attain more precise control of optical losses. Similarly, a circular shape of grating elements was chosen to minimize the introduced scattering losses. Changing the radii of the circular elements enables the tuning of evanescent field extension to the surrounding medium and control the losses of modes supported by the ring resonator. A 2nd order annular Bragg grating generates a vortex beam of light in the vertical direction to the ring surface [58]. This vertically propagating vortex beam corresponds to the zero-diffraction order and a 2nd order photonic band gap is induced. Due to this band gap, the modes are also expected to experience mode splitting as the introduced elements lead to counter propagating modes. The latter eliminates traveling modes and results in the buildup of two standing wave resonances. These resonances are related to the appearance of even and odd standing-wave modes (E and O modes in **Figure 60** [P2]) as a symmetric and anti-symmetric superposition of the counter-propagating traveling waves, which corresponds to air and dielectric Bloch modes [P3], predominately located either in the surrounding air of grooves and inside the dielectric material of microring waveguide.

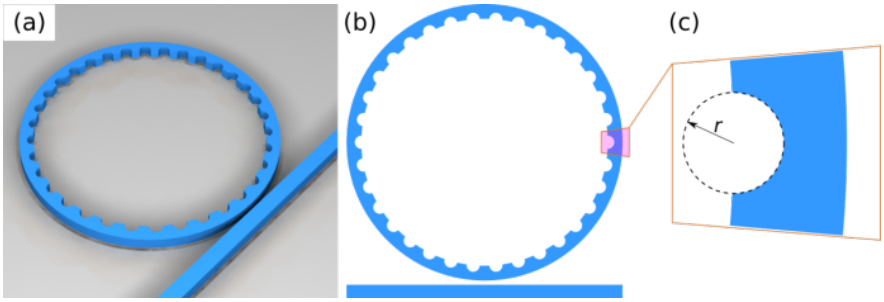

Figure 60. Microring resonator with a 2nd order annular Bragg grating. **a**, Sketch of the microring with a bus waveguide in isometric. **b**, Top-down view. **c**, Circular element of the 2nd order Bragg grating where r is the radius of the cylinder. White color indicates air (n = 1) and blue silicon (Si, n = 3.476), thickness of the silicon - 220 nm.

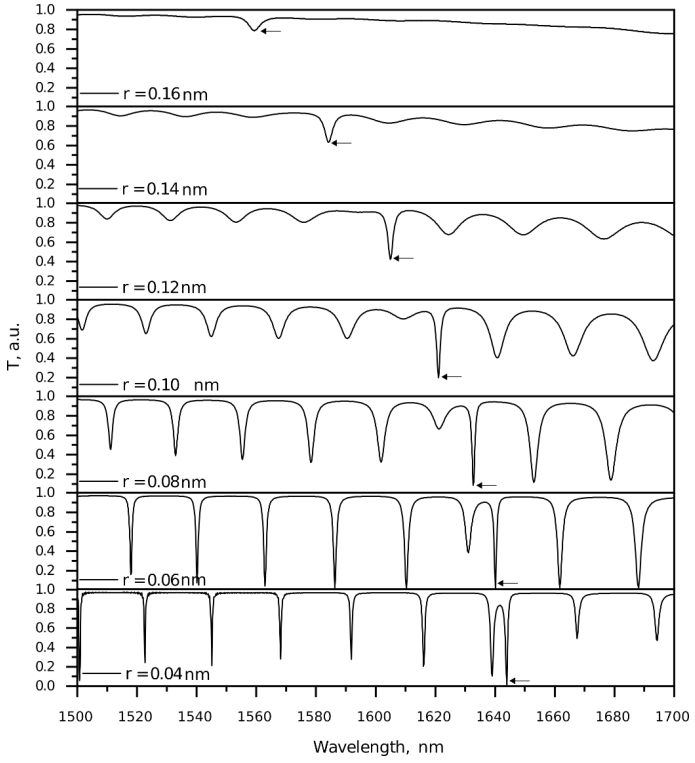

Figure 61. Theoretical transmission spectra. The transmission for different microring resonators with varying radii r of the circular 2nd order Bragg grating elements. Here r is given in nanometers, the grating period is 0.734 μm and surrounding medium is PMMA (Poly methyl methacrylate, n = 1.481). Arrow indicates the dielectric Bloch mode, where k = 0.

FEM and FDTD were used to numerically explore the effects introduced by periodic circular defects of increasing magnitude. The geometrical structure simulation parameters assume a microring middle-radius of 4 μm, microring waveguide widths of 0.45 μm and 0.4 μm for bus waveguides, respectively, and a coupling gap of 130 nm. The total number of 2nd order Bragg grating elements was 36. When the introduced periodic circular incisions are at or above r = 40 nm, pronounced mode splitting at a 1.64 μm wavelength is induced, which is accompanied by leaky mode radiation in the vertical direction to the microring surface at wavenumber $\boldsymbol{k}$ = 0, and, notably, the increase of the quality of factor of the split mode [59]. The arrows in **Figure 61** shows the high-Q dielectric Bloch mode of even symmetry. The air Bloch mode has a considerably lower Q-factor due to grating induced scattering losses. The field intensity plots of both split resonances, corresponding to air and dielectric Bloch modes, are presented in **Figure 62**.

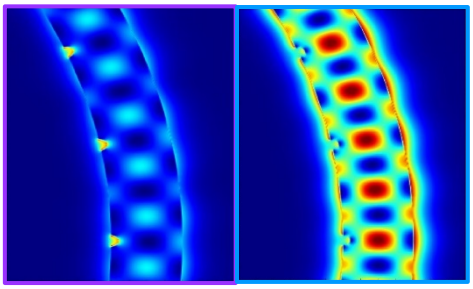

(a) (b)

Figure 62. FDTD simulated mode distribution at 2nd order photonic band gap in annular grating modified micro-ring resonator with groove radii r = 40 nm. The field intensity plots of modes for the 2nd order Bragg grating split resonances: **a**, Air Bloch mode. **b**, Dielectric Bloch mode.

As the grating element radii r are made larger, the scattering losses in the system increase until only a single resonance mode – the dielectric Bloch mode – which matches the second order Bragg condition and has the highest intrinsic quality factor, remains. This situation is opposite to the case studied in [P2], where microring decorated by plasmonic Au nanodics supports an air Bloch mode of odd symmetry and filters the dielectric Bloch mode via damping by losses in the metal disks. In general, such filtering mechanisms enable the precise identification of the effective index of the guided mode, making it ideal for sensing applications as free spectral range plays less of a role (since other modes are suppressed) and a large resonance shift can be

detected without ambiguity. The blueshift of all the spectral peaks (F) is related to an effective mode refractive index decrease due to increased volume fraction of the radial grating elements.

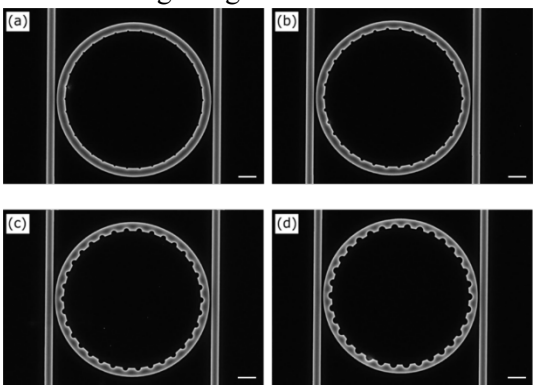

Figure 63. Scanning electron microscopy images of fabricated microring resonators equipped with 2nd order Bragg gratings with varying radii of the circular grating elements. a, r = 40nm. **b**, r = 80 nm. **c**, r = 120 nm. **d**, r = 160 nm. The white scale bar represents 1 μm.

EBL and DUV lithography were used to fabricate different microring resonators with 2nd order Bragg grating, which have varying radii *r* of the circular grating elements, varying from 0 nm to 160 nm in steps of 20 nm, with images of select examples given in **Figure 63**. Each microring was coupled to two bus waveguides in an add-drop configuration for measurement and characterization purposes. While it was numerically predicted that mode splitting would appear at 1,64 μm wavelength (**Figure 61**), in experiment it was observed at 1,62 μm (**Figure 64**). This mismatch between model and experiment can be attributed to variations in the Si device layer thickness and fabrication imperfections.

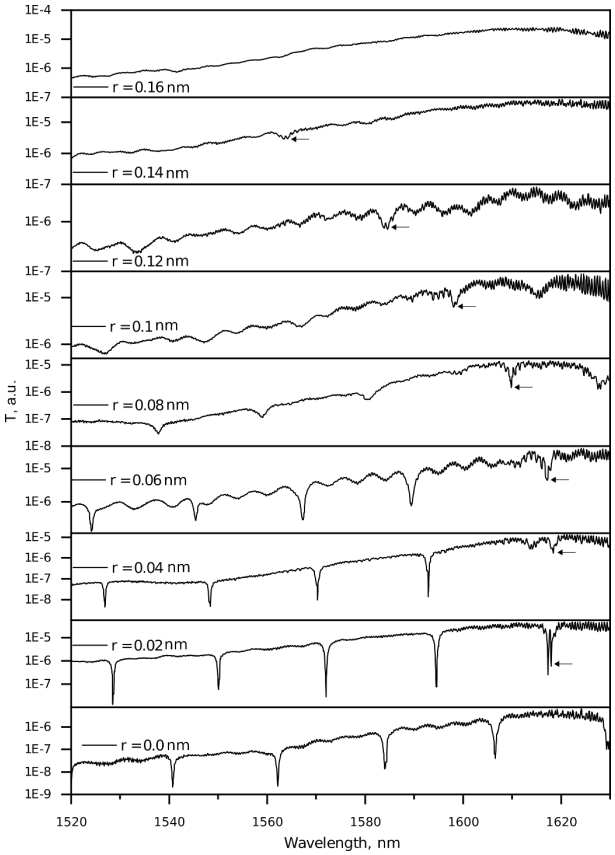

Figure 64. Experimental transmission spectra exhibited by different microring resonators with varying radii r of the circular 2nd order Bragg grating elements. Here r is given in nanometers, the grating period is 0.734 μm and surrounding medium is PMMA. Arrow indicates the dielectric Bloch mode, where k = 0.

To verify the viability of the microring resonator with an integrated 2nd order Bragg grating as a sensor the device was exposed to different refractive index surrounding media (**Figure 65**). Here, water (n =1.333) and 12% Glycerol water solution (n =1.348) were chosen as sensing materials. The measured sensitivity of such a resonator is approximately 73.5 nm/RIU for air Bloch mode and 73.4 nm/RIU for dielectric Bloch mode when circular grating element radii are r = 20 nm (**Figure 65**a). At this shallow microring resonator perforation depth, the device sensitivity is approximately equal to that of a conventional microring 70 nm/RIU [5]. When perforation depth is increased to r = 40 nm (**Figure 65**b), the measured sensitivity becomes 102.1 nm/RIU for air Bloch mode and 83.1

nm/RIU for dielectric Bloch mode. Hence, the experimental sensitivity of air Bloch mode is roughly 1.5 times larger than the sensitivity of an unmodified microring resonator. Despite higher optical losses and a lower Q-factor (**Figure 65**b) of air Bloch mode, this mode is more sensitive to the surrounding medium than the waveguide-confined dielectric Bloch mode. This peculiarity of mode splitting induced by a 2nd order Bragg grating can be used for the development of a self-referenced sensor that would be like that suggested in [102] based on coupled microcavities ("photonic molecules") or in [103] based on a single Au nano disk attached to a microring resonator. This self-referenced sensor could be immune to changes of the ambient parameters, such as temperature, and capable of discriminating between bulk index changes and specific/nonspecific surface binding events. This provides a significant advantage over conventional microring resonator sensors for drug discovery, point-of-care testing applications and sensing of gases [104]. Harnessing the feature of coherent perfect absorption of split Bloch modes [105-107], if the surrounding medium exhibits an absorption coefficient that is dependent on hydrogen gas concentration, such as Pd or WO_3 nano materials [20-22], it is possible to develop a hydrogen gas sensor based on excitation of an air Bloch mode that is immune to changes of temperature induced by exothermic catalyst burning reactions of Pd or WO_3 hydrides in ambient air conditions.

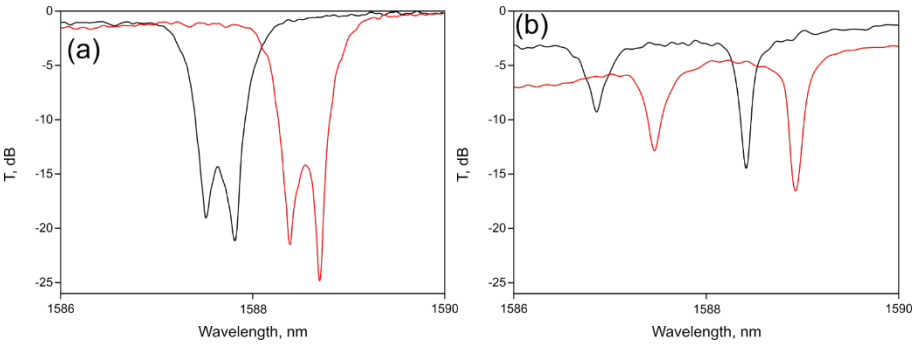

Figure 65. Transmission spectra of a microring resonator. a, Second order Bragg grating having the radius of the circular grating element r = 20 nm. **b**, r = 40 nm. Here black curve indicates the transmission spectrum when the surrounding material is water (n =1.333) and red - Glycerol 12% (n = 1.348).

3.5.4 Conclusions

It is established that microrings with implemented 2nd order gratings can have enhanced quality factors and sensitivity to external cladding environment. For loss-modified microring resonators with second order Bragg grating, the annular grooves filter out photonic non-matching modes of a SOI ring, enhance sensitivity and FSR of the sensor, which is useful for development of self-referenced bio and hydrogen gas sensors.

Main results and conclusions

- A state-of-the-art microring resonator structure having low refractive index material defects has been designed and proposed as an effective and bulk refractive index sensor. It is shown that the sensitivity of the proposed refractive index sensor is higher than the one of the ordinary microring resonator. The perforated microring resonator enables control of the quality factor and the sensitivity of the microring, enabling tuning and adaptation of sensor for specific use cases. The design not only achieves high sensitivity, but also increases the total area of the interface between the microring resonator and the surrounding medium, which can increase the light–matter interaction with aqueous media and gases.

- Metal nanodisk arrays on a microring resonator create a novel ultra-wide FSR sensor platform. Average sensitivity of the device is ∼176 nm/RIU which is 2-fold improvement over the value of ∼70 nm/RIU exhibited by an unmodified analogue.

- The sensors were realized using state-of-the-art electron and ion beam lithography for waveguide definition and a subsequent pattern overlay for metal nanodisk fabrication via a lift-off [68]. Au nano-disks offer a functionalization platform that makes the proposed design for a highly selective sensor.

- Microring resonator with an integrated one-dimensional photonic crystal shows that due to the higher mode field localization inside the hole region of photonic crystal, the air band has higher bulk refractive index sensitivity.

- Analysis of a microring resonator with a partially etched integrated 1D photonic crystal having a 3D geometry is a good alternative for enhanced sensitivity and measurement range. The perforation-induced photonic bandgap can be used as a spectral reference to overcome limitations imposed by the free spectral range. Limit of detection can be minimized using the geometrical parameters of the sensor. Partial etch features add an additional degree of freedom to the design and optimization of micro ring resonator sensor devices.

- Microrings with implemented 2nd order gratings have enhanced quality factor and sensitivity to external cladding environment. Loss-modified microring resonators filter out photonic non-matching modes of a SOI ring, reaching single mode operation, enhance sensitivity and enable for self-referenced sensors.

SANTRAUKA

TEMOS AKTUALUMAS

Optiniai biojutikliai, kuriais galima aptikti ir kiekybiškai įvertinti bio medžiagas, tapo labai įdomia tyrimų sritimi dėl didžiulio ankstyvosios ligų diagnostikos poreikio farmacijos, saugumo, maisto kokybės kontrolės ir aplinkos tyrimų srityse [1], taip pat dėl šiuo metu gyvybiškai svarbios virusų aptikimo srities [2]. Optinis biojutiklis - tai kompaktiškas prietaisas, kuriame biometriniai jutikliai integruoti su sistema keičiančia medžiagos poveikį į išmatuojamą optinį signalą. Optinio biojutiklio paskirtis - generuoti signalą, proporcingą matuojamos medžiagos (analitės) koncentracijai. Optiniuose biojutikliuose kaip biologiniai atpažinimo elementai gali būti naudojamos įvairios biologinės medžiagos, įskaitant fermentus, antikūnus, antigenus, receptorius, nukleorūgštis, audinius ir ištisas ląsteles. Paviršiaus plazmonų rezonansas (PPR), integruoti rezonatoriai, gardelės, lūžio rodiklio matavimo prietaisai, evanescencinių bangų fluorescencija ir optinė bangų interferometrija naudoja evanescencinį lauką prie biojutiklio paviršiaus tam kad nustatyti biometrinio elemento sąveikai su analite. Iš įvairių optinių jutiklių pastaraisiais metais būtent lūžio rodiklio jutikliai pasirodė kaip perspektyvi technologija. Naudojant šią technologiją stebimas vidutinis lūžio rodiklio pokytis, kuris kinta pakitus išoriniai terpei [3]. Lūžio rodiklio jutikliai leidžia be žymėjimo, realiame laike ir tiesiogiai aptikti molekulių sąveiką ties sąsaja tarp dviejų medžiagų.

Nors yra daug įvairių lūžio rodiklio jutiklių [4], optiniai jutikliai, kurie yra pagrįsti daugiakartinę fotonų sąveika su mikro struktūromis, pasižyminčiomis aukštu kokybės faktoriumi, yra viena jautriausių ir perspektyviausių bežymekliniai jutiklių klasių. Konkretaus įrenginio kokybės koeficientas yra fotonų gyvavimo trukmės struktūroje matas. Didesnis kokybės koeficientas reiškia ilgesnę gyvavimo trukmę. Pagrindiniai kokybės koeficiento privalumai yra daug kartų sklindančios elektromagnetinės spinduliuotės sąveika su prietaisą supančia medžiaga ir siauras rezonanso linijos plotis, leidžiantis išmatuoti nedidelius rezonanso bangos ilgio poslinkius, atsirandančius dėl nedidelio lūžio rodiklio pokyčio, kurį sukelia prisijungusios medžiagos.

Tarp optinių jutiklių su aukštu kokybės faktoriumi, optiniai žiediniai mikro rezonatoriai dėl savo praktiškumo tapo didelio susidomėjimo objektu kuriant bangos ilgio selektyvius filtrus [5, 6], jungiklius [7], moduliatorius [8], žemo generacijos slenksčio puslaidininkinius lazerius [9, 10], taip pat

naudojant juos jutikliams ankstyvosios ligų diagnostikos, saugumo ir aplinkos stebėsenos srityse [3, 5, 11, 12], kur optiniais rezonatoriais pagrįsti didelio jautrumo bežymekliniai jutikliai yra vieni perspektyviausių [13]. Jie pasižymi mažais sklaidos nuostoliais, veikia vienu skersinės modos režimu ir yra nedideli (~ 3 μm, mažas užimamas plotas).

Paprasčiausią žiedinį mikro rezonatorių sudaro magistralinis bangolaidis ir žiedinė struktūra (angl. all pass resonator [14]). Optinė moda iš bangolaidžio per jo paviršiuje sklindantį nespindulinį lauką patenka į žiedinį mikro rezonatorių. Banga, prasklidusi visą ratą ir įgijusi tam tikrą fazę, grįžta atgal į magistralinį bangolaidį ir interferuoja su perduodama banga. Esant rezonansui, fazės prieaugis yra toks, kad bangos destruktyviai interferuoja [15]. Tokių rezonatorių jutiminės savybės atsiranda dėl modų lauko sąveikos su aplinkine terpe. Aplinkinės terpės lūžio rodiklio pokytis sukelia modos sklidimo konstantos pokytį, kuris vėliau lemia rezonanso sąlygų pasikeitimą. Šį poveikį galima stebėti stebint rezonanso bangos ilgio padėties poslinkį [16].

Tirti žiedinių mikro rezonatorių optiniai jutikliai remiasi silicio ant izoliatoriaus žiediniais mikrorezonatoriais [16, 17]. Moderniausia silicio ant izoliatoriaus platforma yra šiuolaikinės telekomunikacinės fotonikos pagrindas ir viena populiariausių optinių jutiklių technologijų. Ji yra patraukli dėl suderinamumo su plačiai naudojamu CMOS puslaidininkių procesu, taip pat dėl didelio lūžio rodiklio kontrasto, leidžiančio užtikrinti stiprę modų lauko lokalizaciją ir mažą bangolaidžio išlinkimo spindulį [5].

Didelė modų lauko lokalizacija Silicije sukelia problemų jutiklių taikymuose dėl palyginti mažo persiklojimo tarp apvalkalo medžiagos ir modų nespindulinio lauko. Itin greitas nespindulinio lauko silpnėjimas aplink Silicio bangolaidžio elementus, kuris, kaip apskaičiuota, 63 nm atstumu sumažėja 1/e karto [18], yra naudingas paviršiniam vandenyje esančių analičių biologiniam jutimui, nes leidžia pasiekti didesnį specifiškumą, nes signale dominuoja funkcionalizuoto paviršinio sluoksnio įtaka. Šioje srityje funkcionalizavimas dažnai pasiekiamas naudojant įvairias dengiamąsias medžiagas, pavyzdžiui, aptikti purškiamąjį trifenileno-ketalo receptorių TNT [19], lašeliniu būdu liejamos ZnO nano dalelės etanolio jutimui [20] arba panardinant į Pt legiruoto volframo oksido solgelio tirpalą norint aptikti H_2 dujas katalizinio degimo būdu [21-23].

Tačiau stiprus modos lauko lokalizavimas yra žalingas, kai reikia didelio tūrinio jautrumo, pavyzdžiui, dujų jutiklio atveju. Tūrinį jautrumą galima padidinti panaudojant Vernierio efektą [24, 25]. Tam reikia naudoti dviejų ar daugiau žiedų, kurių spinduliai šiek tiek skiriasi, sistemą, o kiekvieno žiedo

spindulys turi būti palyginti didelis (kelių dešimčių mikronų), todėl laisvasis spektrinis diapazonas (atstumas tarp gretimų rezonansų) būtų gana mažas. Šiam apribojimui įveikti pasiūlyta keletas kitų strategijų, įskaitant itin plonus SOI žiedinius mikro rezonatorius [26], plyšinius bangolaidinius žiedinius mikro rezonatorius [13, 27, 28], pridedant polimero sluoksnį rezonatoriaus paviršiuje [29], įvedant subbangines gardelines struktūras [30-33] ir fotoninius kristalus žiedinio mikro rezonatoriaus viduje [P1, 34-40] ir mikro žiedą su periodiškai išdėstytais metalo nano diskeliais [P2, 42]. Kitas būdas sustiprinti šviesą apvalkalo medžiagoje - įvesti vidutinio lūžio rodiklio moduliaciją. Yra publikuota keletas šia strategija pagrįstų mikro tarpų geometrijų: plyšinis mikro tarpų rezonatorius [43, 44, 45] (jautrumas iki 350 nm/RIU) ir SNOW mikro tarpų rezonatorius [46] (teorinis jautrumas iki 350 nm/RIU).

Kita problema, kylanti dėl didelio lūžio rodiklio kontrasto, ypač santykinai didelio spindulio žiedinių mikro rezonatorių atveju, yra laisvasis spektrinis diapazonas , kuris riboja išmatuojamą tiriamos medžiagos koncentracijos pokyčių dydį. Rezonanso bangos ilgio poslinkis, viršijantis laisvąjį spektrinį diapazoną, tampa neatskiriamas nuo gretimo rezonanso. Todėl, siekiant padidinti matavimo diapazoną, buvo pasiūlyta taikyti gretimų modų slopinimą [37, P2,] ir naudoti žiedinius mikro rezonatorius su įterptu asimetriniu Macho-Zehnderio interferometru [47].

Ši daktaro disertacija skirta biojutiklių, paremtų fotoniniais mikro žiediniais rezonatoriais, kurie pasižymi mažu tūriniu jautrumu bei ribotu laisvu spektriniu diapazonu, tyrimui ir minėtų parametrų pagerinimui. Siekiant įveikti pastarąsias problemas, tiriamos įvairios mikro žiedinių rezonatorių geometrijos ir koncepcijos, kad būtų padidinta šviesos ir medžiagos sąveika. Šiame darbe pateikiamas naujų žiedinių mikro rezonatorių geometrijos, pagrįstos šerdies medžiagos efektyviojo lūžio rodiklio moduliavimu, skaitmeninis modeliavimas bei matavimai. Siekiant padidinti sensoriaus jautrumą, padidintas mikro rezonatoriaus paviršiaus plotas (tuo pačiu šviesos ir medžiagos sąveiką) šerdies medžiagoje įvedus mažesnius už bangos ilgį tuščiavidurius defektus. Be to, kad būtų galima nagrinėti mikro žiedinius rezonatorius, kuriuose rezonanso poslinkiai yra per dideli, ar naudojant mikro žiedinius rezonatorius su sugeriančiomis šviesą medžiagomis parodyti nauji žiediniai mikro rezonatoriai neturintys laisvo spektrinio diapazono apribojimo, bei mikro žiediniai rezonatoriai, veikiantys su šviesą sugeriančiomis medžiagomis. Galiausiai, siekiant supaprastinti aptikimo mechanizmą, pasiūlyti savaiminio kalibravimo jutikliai.

DARBO TIKSLAI

Šios disertacijos tikslas - ištirti ir sukurti naujus optinius mikro jutiklius, taikant skirtingus metodus, pavyzdžiui, efektyviosios lūžio rodiklio moduliacijos, 1D Brego gardelės ir absorbuojančios metalo nano struktūros. Pagrindinis šios disertacijos indėlis - pademonstruotas tūrinio jautrumo valdymas naudojant nuostolingas perforacijas, taip pat realizuoti savaiminiu kalibravimu pasižymintys optiniai jutikliai, pagrįsti mikro žiediniais rezonatoriais. Ypač daug dėmesio buvo skirta šių aspektų tyrimams:

- Tirti integruoti optiniai mikro jutikliai, kurių šerdyje išėsdintos subbanginės perforacijos, kad padidėtų šviesos ir medžiagos sąveika. Be to, parodyta, kad galima padidinti perforuotų mikro rezonatorių tūrinį jautrumą;
- Tirti jutiklį, kurio laisvasis spektrinis diapazonas yra ribotas, t. y. jei rezonansų poslinkis yra didesnis nei laisvasis spektris diapazonas, aptikti tiriamas medžiagas tampa neįmanoma. Atlikti optinio silicio ant izoliatoriaus žiedinio mikro rezonatoriaus, su periodiškai išdėstytais aukso nano diskais, kurie leidžia mikro rezonatoriuje sklisti tik vienai išilginei modai, tyrimą;
- Atlikti pagaminto žiedinio mikro rezonatoriaus su integruotu vienmačiu fotoniniu kristalu tyrimą. Be to, tiriamas mikro rezonatorius su Brego gardele, veikiantis ir oro, ir dielektriko fotoninėse juostose, siekiant suprasti, kaip abiejuose draustinės juostos tarpo kraštuose esantys rezonansai lemia žiedinių mikro rezonatorių jautrumą;
- Tirti 3D perforacijas, kurios gali padidinti jautrumą ir matavimo spektrinį diapazoną. Daugiausia dėmesio skirti iš dalies išgraviruotoms stačiakampėms perforacijoms;
- Tirti gardelės, esančios ant vidinės žiedinio mikro rezonatoriaus sienelės. Be to, sukurti savaiminiu kalibravimu pasižymintį jutiklį, atsparu aplinkos temperatūros pokyčiams.

DARBO UŽDAVINIAI

- įsteigti optinio charakterizavimo laboratoriją ir sistemą, kurioje būtų galima matuoti integruotus optinius prietaisus. Tai apima tinkamos optinės įrangos nustatymą ir įsigijimą;

- suprojektuoti integruotą optinę grandinę su visais jungiamaisiais elementais, tokiais kaip gardelės, optiniai bangolaidžiai, modų keitikliai ir žiediniai mikro rezonatoriai;
- - suprojektuoti visus integruotus optinius elementus, kurie atitinka pasaulinių lustų gamyklų keliamus apdirbimo reikalavimus;
- suprojektuoti visus integruotus optinius elementus, suderinamus su kelių pakopų elektronų pluošto litografija;
- suprojektuoti gardelės jungtuvus, kurie veiktų tinkamame žiedinių mikro rezonatorių dažnių diapazone;
- suprojektuoti ir modeliuoti optinius žiedinius mikro rezonatorius, kurie yra sujungti su magistraliniais bangolaidžiais;
- suprojektuoti ir sumodeliuoti žiediniai mikro rezonatorius su 1D perforacijomis, kad būtų padidintas tūrinis jautrumas;
- suprojektuoti ir sumodeliuoti žiedinius mikro rezonatorius su aukso nano diskeliais , kad būtų galima sukurti savaiminio kalibravimo bei jautresnius jutiklius paviršiaus ir tūrinio lūžio rodiklio pokyčiams. ;
- atlikti žiedinių mikro rezonatorių apdirbimą naudojant moderniausias švarias patalpas;
- suprojektuoti, sumodeliuoti ir apdoroti žiedinius mikro rezonatorius su integruotomis 3D deformacijomis;
- suprojektuoti, sumodeliuoti ir pagaminti žiedinius mikro rezonatorius su vidinėje šoninėje sienelėje integruotomis grotelėmis ir pademonstruoti savaiminio kalibravimo galimybes;
- atlikti visų skirtingų prietaisų, skirtų konkretiems eksperimentams, optinius matavimus.

MOKSLINIS NAUJUMAS IR PRAKTINĖ VERTĖ

Šioje disertacijoje atlikti eksperimentiniai optiniai tyrimai yra susiję su besiformuojančia integruotų optinių biologinių ir dujų jutiklių technologijų sritimi.

Pagrindinė šio tyrimo naujovė yra optinio žiedinio mikro rezonatoriaus su mažos dielektrinės skvarbos medžiagos defektais struktūros, skirtos

geresniam optiniam jutikliui, demonstravimas. Parodyta, kad pasiūlytas lūžio rodiklio jutiklis, pagrįstas žiediniu mikro rezonatoriumi su perforacijomis, yra pranašesnis už įprastus žiedinius mikro rezonatorius. Perforuotas žiedinis mikro rezonatorius leidžia keisti kokybės koeficientą ir jautrumą, todėl jį galima pritaikyti daugelyje optikos sričių. Galima ne tik pasiekti didelį jautrumą, kuris nustatomas iš rezonanso bangos ilgio poslinkio dėl nedidelio efektyviojo lūžio rodiklio pokyčio, kurį sukelia šalia prietaiso esančios analitės, bet ir padidinti bendrą žiedinio mikro rezonatoriaus ir jį supančios terpės sąveikos plotą, kuris lemia padidėjusią šviesos ir medžiagos sąveika, pavyzdžiui su vandeninėmis terpėmis ir dujomis.

Parodyta, kad žiedinis mikro rezonatorius su aukso nano diskais leidžia itin platų laisvąjį spektrinį diapazoną. Tai lemia nepalaikomų arba stipriai sugertų modų filtravimas. Vienintelis ribojantis veiksnys yra bangolaidžio juostos plotis, kurį apibrėžia bangolaidžio geometrija ir jam pagaminti naudojamos medžiagos.

Buvo ištirtas praktinis jutiklio su vienmačiu fotoniniu kristalu, suformuotu iš dalies išėsdintomis cilindrinėmis perforacijomis, įgyvendinimas. Parodyta, kad aukštesniosios modos laukas lokalizuojasi fotoninio kristalo skylučių viduje, oro juostoje, ir pasižymi didesniu tūriniu lūžio rodiklio jautrumu.

Parodyta, kad erdvinis mikro rezonatorius su integruotu 1D fotoniniu kristalu, turinčiu 3D geometriją, pasižymi didesniu jautrumu ir matavimo diapazonu. Dalinės perforacijos sukeltas fotoninis juostos tarpas gali būti naudojamas kaip spektrinis etalonas siekiant įveikti laisvojo spektrinio diapazono lemiamus apribojimus.

Siekiant papildyti žiedinio mikro rezonatoriaus su aukso nano diskeliais tyrimus, buvo įgyvendinti mikro žiedai su dielektrinėmis 2 eilės Brego gardelėmis. Pastarieji pasižymi geresniais kokybės faktoriais ir jautrumu išorinei apvalkalo aplinkai. Šie nuostoliais modifikuoti mikro jutikliniai rezonatoriai su antros eilės Brego gardelėmis filtruoja silicio ant izoliatoriaus mikro jutiklio fotonines nesuderintas modas, didina jutiklio jautrumą ir laisvąjį spektrinį diapazoną (kaip ir aukso nano diskeliai), o tai naudinga kuriant savaiminio kalibravimo biologinius ir dujų jutiklius.

Šis darbas vertingas prietaisams, kurių darbas priklauso nuo šviesos ir medžiagos sąveikos. Pavyzdžiui, optiniams jutikliams, kuriais reikia aptikti nedidelį medžiagos kiekį, reikia stiprios šviesos ir medžiagos sąveikos. Įvedus siūlomas perforacijas, padidėja elektromagnetinio lauko persidengimas su supančia terpe, tuo pačiu padidėja jautrumas mažesniam medžiagos tankiui supančioje terpėje.

Siūlomi savaiminiu kalibravimu pasižymintys rezonatoriai leidžia naudoti didelius žiedinius rezonatorius kaip jutiklius. Didinant žiedinio rezonatoriaus spindulį, mažėja laisvasis spektrinis diapazonas (jis lengvai gali būti mažesnis nei 1 nm). Tai reiškia, kad žiedinių rezonatorių rezonansų padėtis keičiasi daugiau nei laisvasis žiedinio rezonatoriaus spektrinis diapazonas, todėl rezonansų poslinkių sekimas tampa dviprasmiškas. Savaiminio kalibravimo mechanizmas pašalina šį trūkumą ir leidžia naudoti didelį plotą apimančius žiedinius rezonatorius. Tai ypač naudinga dujų jutikliuose, kuriuose reikia aptikti mažo tankio medžiagas.

GINAMIEJI TEIGINIAI

- Integruoti žiediniai mikro rezonatoriai su perforuotais 1D matmenų defektais sustiprina elektromagnetinio lauko sąveiką su jį supančia medžiaga ir, išlaikydami aukštą kokybės faktorių, pranoksta įprastus žiedinius mikro rezonatorius. Be to, 1D periodinės struktūros palaikomos skirtingos oro ir dielektriko modos leidžia užfiksuoti elektromagnetinio lauko maksimumus žemo lūžio rodiklio medžiagoje, taip padidinant šviesos ir medžiagos sąveiką.
- Įvesti metaliniai nano diskai žiedinio mikro rezonatoriaus viršuje arba 2 eilės Brego gardelės vidinėje žiedinio mikro rezonatoriaus sienelės pusėje filtruoja nepalaikomas išilgines ir skersines modas, todėl galima dirbti su viena moda.
- Modifikuoti integruoti žiediniai mikro rezonatoriai pasižymi specifiniu optiniu atsaku , t. y. vienos modos veikimu arba draustinėmis dažnių juostomis, kurios gali būti naudojamos savaiminio kalibravimo prietaisams.

DISERTACIJOS SANDARA

Disertacija parašyta anglų kalba, ją sudaro: įvadas, literatūros apžvalga, naudotos įrangos ir matavimo metodikų aprašymai, rezultatų apibendrinimas, išvados, cituotos literatūros sąrašas, trumpiniai ir pagrindiniai žymėjimai, santrauka lietuvių kalba.

AUTORIAUS ĮNAŠAS

Disertacijos autorius atliko prietaisų projektavimą, modeliavimą, gamybą, eksperimentus, taip pat dalyvavo analizuojant rezultatus, pateikiant

duomenis, rengiant ir recenzuojant rankraštį. Taip pat daug prisidėjo prie Fizinių ir Technologijos Mokslų Centro nanofotonikos laboratorijos kūrimo ir pasiūlė daugumą idėjų, susijusių su pateiktais rezultatais.

3.1, 3.2 dalyse autorius sugalvojo idėją, suprojektavo, sumodeliavo ir išmatavo bandinius. 3.3 dalyje autorius suprojektavo, sumodeliavo ir pagamino bandinius. 3.4 dalyje autorius prižiūrėjo darbui ir atliko rezultatų analizę. 3.5 dalyje autorius sugalvojo idėją, suprojektavo ir sumodeliavo prietaisus.

PAGRINDAI

Pirmame skyriuje pateikiamos pagrindinės žinios apie šviesos sklidimą integruotuose optiniuose bangolaidžiuose, kuriuos galima įsivaizduoti kaip mažus šviesolaidžius ant silicio dioksido plokštelės bei kurie yra vienas pagrindinių šiame darbe naudojamų elementų. Šiame skyriuje taip pat pateikiami visiškojo vidaus atspindžio bei efektyvaus lūžio rodiklio fizikiniai reiškiniai, kurie yra naudojami sutelkti šviesą bei valdyti šviesos sklidimą. Tam kad sukurti fotoninį bio sensorių reikalinga stipri šviesos ir medžiagos sąveika. Deja, norint tai pasiekti tik bangolaidžiais yra gana sudėtinga problema . Ši sąveika gali būti pagerinta naudojant optinius rezonatorius, kurie efektyviai prailgina šviesos ir medžiagos sąveiką apibrėžtame tūrio vienete. Tam, kad suprasti jų veikimo pagrindus, pateikiami darbe naudotų mikro rezonatorių, žiedinių mikro rezonatorių bei integruotų fotoninių sensorių veikimo mechanizmai.

1.1 poskyryje pateiktas integruotų optinių bangolaidžių veikimo pagrindas bei apibūdintas fizikinis šviesos sklidimo šiais bangolaidžiais reiškinys. 1.1.1 poskyryje aprašomas visiškas vidaus atspindys, kuris tinka apibūdinti šviesos sklidimą bangolaidyje. 1.1.2 poskyryje aprašomi subbanginiai bangolaidžiai, kurie veikia efektyvaus lūžio rodiklio principu. Terminas subbanginis reiškia, kad matmenys yra mažesni už sklindančios šviesos bangos ilgį. Tokiuose bangolaidžiuose sklindanti moda, skersinis šviesos svyravimas, nėra pilnai sutelkta bangolaidyje, bet dalinai iš jo išeina. Šis šviesos laukas ir yra pagrindinė fotoninių sensorių esmė.

1.2 poskyryje aprašomi integruoti mikro rezonatoriai, kuriuos galima įsivaizduoti kaip šviesolaidį, kurio galuose yra šviesą atspindintys Brego veidrodžiai. Integruotų mikro rezonatorių atveju šviesolaidis yra pakeičiamas bangolaidžiu, o veidrodžiai – vienmačiais fotoniniais kristalais, kurių veikimo principas labai panašus į Brego veidrodžių. Tokiame rezonatoriuje susiformuoja stovinti banga. Į šį rezonatorių šviesa įvedama prie veidrodžių prijungus papildomą bangolaidį. Šviesa, kuri atitinka rezonatoriaus palaikomas stovinčias bangas, pateks į jo vidų ir po kurio laiko, kuris apibrėžtas rezonatoriaus kokybės faktoriumi, paliks rezonatorių. 1.2.1 aprašomi mikro žiediniai rezonatoriai, kurie yra mikro rezonatorių dalis. Nuo mikro žiedinių rezonatorių jie skiriasi tuo, kad vietoje veidrodžių bangolaidžio galuose, bangolaidžio pabaiga ir pradžia yra sujungtos, tai yra suformuojamas žiedas. Tokiame rezonatoriuje stovinti banga nesusiformuoja, čia ji sklinda aplinkui rezonatorių, taip vadinama bėganti banga. Pagrindinis jų pliusas lyginant su mikro rezonatoriais yra veidrodžių

nebūvimas, kas supaprastina jų gamybą ir leidžia pasiekti aukštesnį kokybės faktorių. Šiuo atveju naudojama pilnai dielektrine struktūra, todėl gaunamos siauros linijos, palyginus su paviršinių plazmonų rezonansais (SPR). Bet jautrumas priklauso ne vien nuo linijos siaurumo, dar ir nuo persidengimo. Nors SPR linijos ir plačios, bet turi gera persidengimą su tiriama medžiaga. Su perforacijomis mes geriname persidengimą ir jautrumą. Šviesa į tokį rezonatorių įvedama šalia rezonatoriaus priartinus bangolaidį. Atstumas parenkamas toks, kad šviesos laukas, kuris sklinda šalia bangolaidžio, persiklotu su žiediniu rezonatoriumi. Modai, kuri sklinda bangolaidžiu, priartėjus prie žiedinio rezonatoriaus, dalis jos lauko persikloja su rezonatoriumi ir šviesa įsivedą į jį. Įvedamos tik tos modos, kurios tenkiną fazinio sinchronizmo sąlygą tarp bangolaidžio ir žiedo. Atstumas turi būti parenkamas toks, kad susidarytų fazinis sinchronizmas tarp rezonatoriuje esančios bėgančios bangos ir bangolaidyje sklindančios bangos.
1.3 poskyryje apibendrinami prieš tai minėti reiškiniai ir apibūdinami fotoniniai sensoriai, kurių veikimo principas yra pagrįstas efektyvaus lūžio rodiklio modifikavimu. Čia pateikiami ir pavyzdžiai, kaip tiriamos medžiagos ar terpės keičia rezonatoriaus palaikomas stovinčias ar bėgančias bangas bei apibūdinamas rezonatoriaus jautrumas.

METODAI IR MEDŽIAGOS

Antrame skyriuje aprašomos darbe naudotos skaičiavimo, prietaisų gamybos metodikos bei eksperimentinis stendas. Aprašomi naudoti baigtinių skirtumų laiko erdvės skaičiavimai, kurie leidžia skaičiuoti šviesos sklidimą realiame laike. Papildomai aprašomas metodas, skirtas tikrinių mikro rezonatorių verčių (palaikomų modų) radimui. Aprašytos prietaisų gamybos technologijos, kurios remiasi elektronų pluošto litografija bei ultravioletine litografija.
2.1 poskyryje trumpai apibūdinti naudoti skaičiavimo metodai. 2.1.1 poskyryje plačiau aprašytas baigtinių skirtumų laiko erdvės metodas (FDTD). Naudojant šį FDTD metodą skaičiuojama struktūra yra suskaidoma į mažas celes laike ir erdvėje, kurios yra daug mažesnės už bangos ilgį. Tokiu būdu mes galime aprašyti šviesos šaltinį tam tikroje skaičiuojamos struktūros vietoje (apima keletą celių) ir leisti sistemai kisti laike. Pati struktūra yra aprašyta naudojant jos lūžio rodiklį ir sugerties koeficientą. Šis metodas leidžia rasti rezonatorių pralaidumo spektrus, palaikomas stovinčias bangas, bei stebėti kaip šviesa sąveikauja su tiriamomis medžiagomis. 2.1.2 poskyryje aprašomas metodas skirtas rasti tikrines tiriamos struktūros

palaikomas vertes (modas). Naudojant šį metodą tiriama struktūra, kaip ir prieš tai, yra suskaidoma į mažas celes. Šiuo atveju yra tiriama ne visa struktūra o tik vienas jos periodinis elementas, pavyzdžiui vienas Brego veidrodžio elementas. Šiam metodui naudojamos periodinės kraštinės sąlygos, kurių dėka galima rasti struktūros palaikomas tikrines vertes, kurios atitinka fazinio sinchronizmo sąlygą, kuri yra apibrėžta kraštinėmis sąlygomis ir pačios struktūros. Šis metodas leidžia suskaičiuoti tiriamos struktūros dispersinę kreivę bei tikrinių verčių profilius.

2.2 poskyryje trumpai aprašomi fotoninių prietaisų gamybos technologija. 2.2.1 aprašoma „top-down“ technologija, kuri pasikliauja bandinių gamyba naudojant įvairias litografines kaukes. Šios kaukės atspindi norimą pagaminti bandinį ir yra formuojamos naudojant specialias elektronams ar šviesai jautrias medžiagas. Šias medžiagas galima lengvai užnešti ant bandinio naudojant išsukimo būdą. 2.2.2 yra aprašoma elektronų pluošto litografija. Čia aktyvia medžiaga padengtas bandinys yra lokaliai paveikiamas elektronų pluoštu. Judinant bandinį elektronų pluošto atžvilgiu yra sugeneruojama norima pagaminti struktūra. Vėliau apšvitinta medžiaga yra apdirbama ėsdinimo skystyje, kuris pašalima paveiktą arba ne (priklausomai nuo fotorezisto medžiagos) medžiagą. Šiuo metodu galima pasiekti net 10 nm skyrą. 2.2.3 skyriuje aprašoma panaši technologija, tačiau čia pasitelkiami ultravioletiniai fotonai. Tai sumažina skyrą (~130 nm) tačiau rašymo greitis ir plotis yra gerokai didesni negu elektronų pluoštas. 2.2.4 poskyryje aprašoma kaip elektronų ar šviesos pluoštu apdirbtų bandinių kaukės yra perkeliamos į norimą medžiagą. Naudojant cheminį (medžiagos sudaro chemines jungtis) ar kinetinį (bombardavimas jonais) ėsdinimą sritys, kurios yra neapsaugotos kaukės, yra pašalinamos, tokiu būdu perkeliant kaukės formą į norimą medžiagą.

2.3 poskyryje aprašomas sudarytas bei tyrimu metu naudotas eksperimentinis stendas. Pirmiausia aprašoma kaip šviesa yra įvedama (**pav. 1**.) į pagamintas struktūras. Tam naudojami gardelių elementai (**pav. 1a**), kurie remiasi antros eilės Brego sąlyga. Šios gardelės yra suformuotos taip, kad iš šviesolaidžio sklindanti šviesa būtų nukreipta į bangolaidį (**pav. 1b**) ar iš jo (**pav. 1c**).

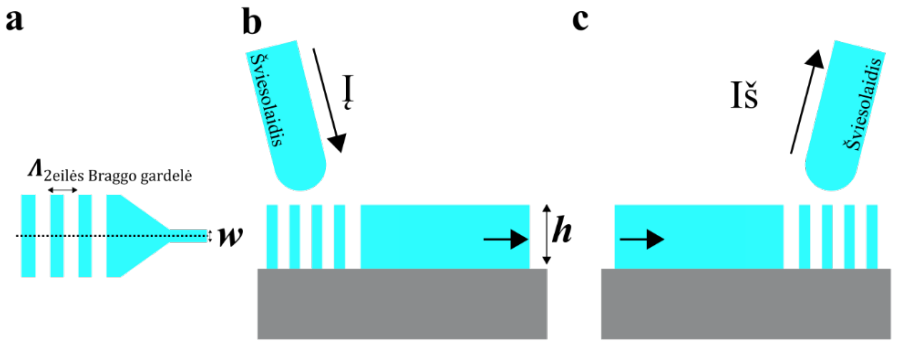

Pav. 1. Šviesos įvedimo į integruotą bangolaidį schema. a, Vaizdas iš viršaus. **b**, Skersinis struktūros pjūvis rodantis šviesos įvedimą. **c**, Skersinis struktūros pjūvis rodantis šviesos išvedimą. Brūkšninė linija **a** žymi skerspjūvius **b** ir **c**, $\Lambda_{2\text{eilės Brego gardelė}}$ — antros eilės Brego gardelės periodas.

Tam, kad tiriama medžiaga pasiektų fotoninį sensorių, reikia ją nukreipti prie rezonatoriaus. Tai atliekama naudojantis PDMS polimere suformuotu kanalu (**Pav. 2**). Viename gale yra įšvirkščiama tiriama medžiaga o, kitame kanalo gale medžiaga palieka kanalą ją išsiurbiant.

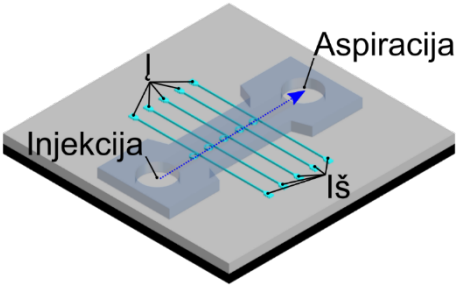

Pav 2. Mikro rezonatorių masyvas su PDMS kanalu. Mikro žiediniai rezonatoriai yra išdėstyti lusto centre ir sujungti su gardeliniais šviesos įvedimo elementais, kurie naudojami šviesai įeiti ir išeiti. Masyvas padengtas PDMS kanalu, kad būtų galima įšvirkšti ir išsiurbti skystį su tiriamomis medžiagomis. Mėlyna punktyrinė rodyklė žymi tiriamos medžiagos judėjimo kryptį.

Eksperimento stendas yra apibūdintas (**Pav. 3**). Jį sudaro valdomas lazeris, kurio bangos ilgis gali būti keičiamas 0.1 tikslumu (diapazonas: 1500 – 1600 nm), poliarizatorius, kuris skirtas šviesos poliarizacijai valdyti. Tai yra

svarbu, nes Brego gardelės, kurios naudojamos šviesai įvesti, yra jautrios šviesos poliarizacijai. Šviesa yra nukreipiama į bandinį naudojant poliarizaciją išlaikančius šviesolaidžius, kurių vienas galas yra nusmailintas tam, kad šviesa paliktų jį ir efektyviai įsivestų į bangolaidį. Bandinį palikusi šviesa yra surenkama kito tokio pačio šviesolaidžio ir yra nukreipiama į šviesos detektorių. Kadangi gardeliniai įvedimo elementai yra labai maži (10:10 mikronų), įvedimo šviesolaidžiai yra patalpinti ant XYZ pozicionavimo sistemų, kurių žingsnis yra ~10 nm.

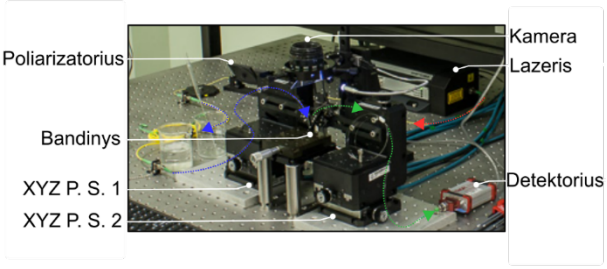

Pav. 3. Eksperimento stendas. Kompiuteriu valdoma optinė sistema. Raudona brūkšninė linija žymi iš lazerio šviesolaidžiu sklindančią šviesą, kuri patenka į linijinį poliarizatorių, mėlyna brūkšninė linija - šviesą, kuri iš poliarizatoriaus patenka į bandinį, žalia brūkšninė linija - šviesą, kuri iš bandinio patenka į detektorių. Rodyklės rodo sklidimo kryptį. P. S. — pozicionavimo sistema.

Pav. 4 pateiktas bandinio vaizdas su įvedimo ir išvedimo šviesolaidžiais iš arti. Optinės sistemos schema yra pateikta **pav. 5**. Be jau minėtų elementų, dalis šviesos yra nuvedama į detektorių kaip atraminis signalas. Tam, kad matyti, kur lokalizuoti bandinį, virš jo įdiegta kamera su objektyvu.
Valdant įvedimo ir išvedimo šviesolaidžių padėtis galima matuoti daug skirtingų elementų esančių ant bandinio paviršiaus. Pats matavimas vyksta realiu laiku, kas leidžia sekti medžiagos ir šviesos sąveiką.

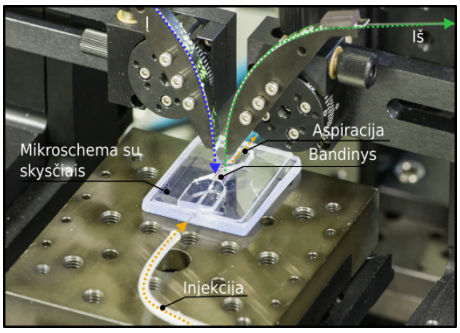

Pav. 4. Bandinys iš arti. Mėlyna brūkšninė linija žymi įvedimo šviesolaidį, žalia brūkšninė linija - išvedimo šviesolaidį, oranžinė brūkšninė linija – įšvirkštimo ir aspiracijos kanalus į PDMS kanalą ir iš jo.

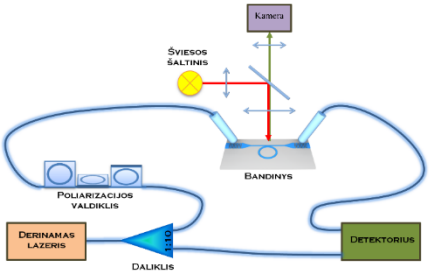

Pav. 5. Optinės sistemos schema. Šviesa iš derinamo lazerio jungiama į optinį pluoštą ir, naudojant 1:10 pluošto skirstytuvą, padalijama į du kanalus: bandinio (patenka į poliarizatorių) ir etaloninį (patenka į detektorių). Poliarizatoriumi galima reguliuoti poliarizaciją, kurios reikia, norint optimizuoti ryšį su gardeliniu jungtuvu. Po mėginio šviesa surenkama šviesolaidžiu ir siunčiama į detektorių. Norint nustatyti mėginio padėtį, jis apšviečiamas šviesos šaltiniu ir atvaizduojamas kameroje.

REZULTATAI

Trečiame skyriuje pateikiama eksperimentų eiga ir rezultatai. Šis skyrius paremtas penkiais straipsniais, kurie buvo atspausdinti disertacijos metu.

3.1 poskyryje pristatomas perforuotas mikro žiedinis rezonatorius, kuris yra sumodeliuotas veikti kaip sensorius. Šis skyrius parengtas remiantis straipsniu: DOI: 10.1088/2040-8978/16/10/105003 (© IOP Publishing. Reproduced with permission. All rights reserved). Parodyta, kad mikro žiedinis rezonatorius su perforacijomis, kurios yra mažesnės už bėgančios bangos ilgį, padidina tūrinį bei dielektrinių dalelių jautrumą lyginant su rezonatoriumi, kuris neturi tokių struktūrų ir išlaiko aukštą kokybės faktorių. Pateikti skaičiavimai atlikti baigtinių skirtumų laiko erdvės (FDTD) bei tikrinių verčių metodais.

3.1.1 poskyryje pateiktas perforuotų žiedinių mikro rezonatorių aktualumas ir aptariami skaičiavimo metodai. 3.1.2 poskyryje pristatomi ir aptariami pagrindiniai rezultatai. 3.1.3 poskyryje pateikiamos skyriaus išvados.

Modeliuotas rezonatorius pateiktas **pav. 6a**. Kaip minėta, šis rezonatorius yra perforuotas elementais, kurių matmenys yra mažesni už bangos ilgį (**Pav. 6b**). Keičiant šių perforacijų geometrinius parametrus galima valdyti, kaip šviesa sąveikauja su rezonatorių supančia terpe ir taip pagerinti ar pasilpninti jo, kaip sensoriaus, veikimą.

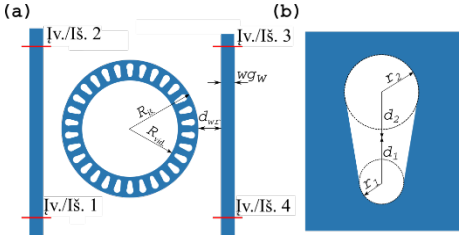

Pav. 6. Mikro žiedinio rezonatoriaus geometrija. a, Keturių įvadų/išvadų (Įv./Iš.) sensoriaus su dviem tiesiais bangolaidžiais ir perforuotu mikro žiediniu rezonatoriumi principinė schema. **b**, Padidinta rezonatoriaus dalis, kurioje matyti išsami defektų geometrija.

Pav. 7 demonstruoja tūrinį (**a**) ir paviršinį (**b**) jautrumus. Valdant modos lauką galima pasiekti kad elektromagnetinis laukas efektyviau sąveikauja su paviršiumi arba tūriu. Tai naudinga turint tiriamas medžiagas, kurios nusėda

ant rezonatoriaus paviršiau. Šiuo atveju galima sumažini tūrinio lūžio rodiklio atsaką.

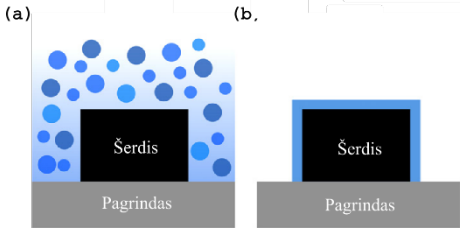

Pav. 7. Sensoriaus jautrumo mechanizmas. a, Tūrinis jautrumas. **b**, Paviršinis jautrumas.

Keli šio rezonatoriaus pralaidumo spektrai pavaizduoti **pav. 8**. Matyti, kad šis rezonatorius sėkmingai paliko bėgančias bangas (keli intensyvumo pikai). Viena banga yra skilusi (**pav. 8a** įterptas paveiksliukas), tai reiškia, kad ši banga yra stovinti banga ir ji susidaro dėl atsiradusios sklaidos nuo įterptų elementų. Užnešus ant šio rezonatoriaus kitą terpę, turinčią didesnį lūžio rodiklį, bėgančių bangų energija pakinta (šiuo atveju efektyvus lūžio rodiklis padidėja ir energija sumažėja, **pav. 8b**).

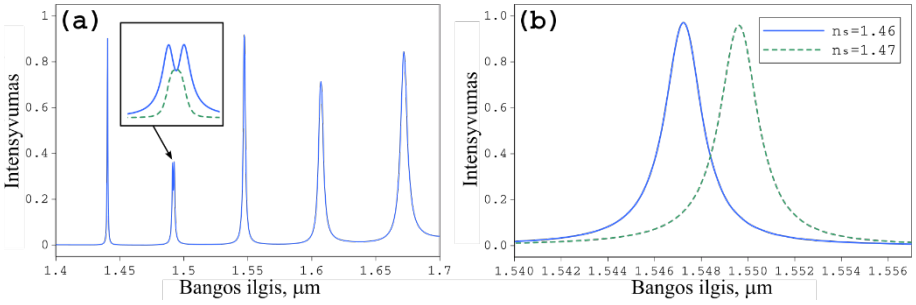

Pav. 8. Žiedinio rezonatoriaus pralaidumo spektras. a, Normalizuotas išvado 1 intensyvumas. Intarpe pavaizduota padidinta figūros dalis, kai bangos ilgis 1,492 µm. Šiame intarpe ištisine linija pažymėtas išvado 1 prievado intensyvumas, o punktyrine linija – išvado 2 intensyvumas. **b**, išvado 1 prievado intensyvumo smailės poslinkis rezonatorių supančios medžiagos lūžio rodikliui keičiantis nuo 1,46 iki 1,47.

Pav. 9 pademonstruota kaip atrodo elektromagnetinio lauko pasiskirstymas tokiame rezonatoriuje ties viena rezonansine moda. Raudona spalva žymi elektromagnetinio lauko apatinę vertę, o raudona – viršutinę.

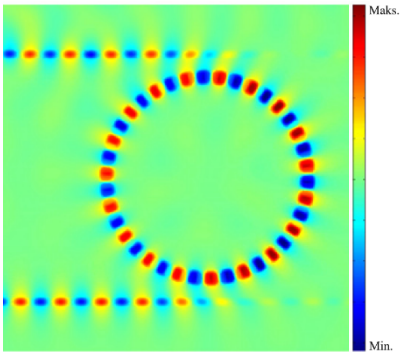

Pav. 9. Elektromagnetinio lauko pasiskirstymas. Elektromagnetinio lauko pasiskirstymas ties 1.547 μm bangos ilgiu (vienas iš rezonansų).

Kaip minėta prieš tai, laikas, kurį šviesa praleidžia rezonatoriuje, priklauso nuo atstumo tarp žiedinio mikro rezonatoriaus ir šviesos įvedimo bangolaidžio. **Pav. 10a** parodyta kaip nuo šio atstumo priklauso rezonatoriaus kokybės faktorius ir nuostoliai. Ši tendencija stebima, nes keičiasi fazinis sinchronizmas tarp rezonatoriaus palaikomos modos ir bangolaidžio palaikomos modos. Esant kritiniui suvedimui (destruktyvios interferencijos sąlyga) matomas aukščiausias kokybės faktorius ir mažiausi nuostoliai atgal į bangolaidį (šviesa pilnai pasilieka rezonatoriuje). Tai reiškia, kad šviesa sklindanti tokiame rezonatoriuje gali daugiau kartų sąveikauti su medžiaga kuri supa šį rezonatorių.

Rezonatoriaus nuostoliai gali būti sumažinti padidinus jo spindulį. Čia esminiai nuostoliai yra įtakoti rezonatoriaus išlinkio. Kuo mažesnis išlinkis , tuo nuostoliai mažesni – rezonatorius tampa panašesnis į tiesų bangolaidį. **Pav. 10b** rodo kaip skiriasi paprasto žiedinio rezonatoriaus ir perforuoto žiedinio rezonatoriaus nuostoliai didėjant jų spinduliams. Kaip matome, paprasto žiedinio rezonatoriaus nuostoliai eksponentiškai mažėja. Perforuoto rezonatoriaus nuostoliai praktiškai nekinta, nes pagrindinis nuostolių šaltinis yra sklaida nuo perforacijų. Tai reiškia, kad šviesa mažiau sąveikauja su išorine rezonatoriaus sienele ir daugiau sąveikauja žiedo viduje. Tai pagerina sensoriaus savybes (sąveika su dalelėmis, kurios yra perforacijose).

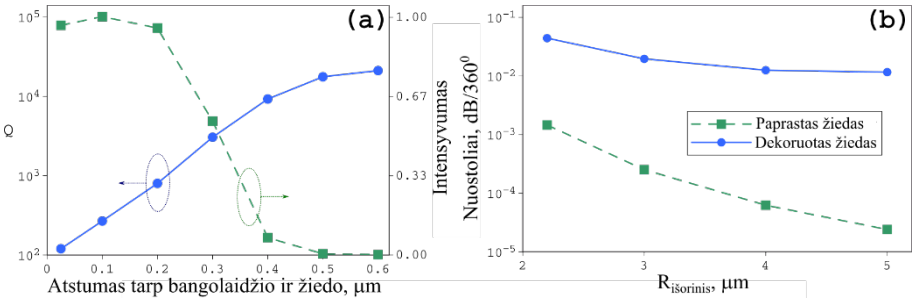

Pav. 10. Kokybės faktorius ir nuostoliai. a, Q faktorius ir normalizuotas „drop“ prievado intensyvumas priklausomai nuo tarpo rezonatoriaus ir bangolaidžio. **b**, Spinduliuotės nuostoliai esant skirtingiems perforuoto mikro žiedinio rezonatoriaus išoriniams spinduliams. Palyginimui tie patys nuostoliai nubraižyti paprastam žiediniam rezonatoriui su tais pačiais geometriniais parametrais.

Prieš tai minėta perforacijų privalumą galime stebėti sekdami rezonansų poslinkį, pridedant dielektrines daleles į rezonatoriaus vidų bei išorę (**pav. 11ab**). Matyti, kad didžiausias rezonanso postūmis stebimas tiriamoms dalelėms esant perforacijų viduje.

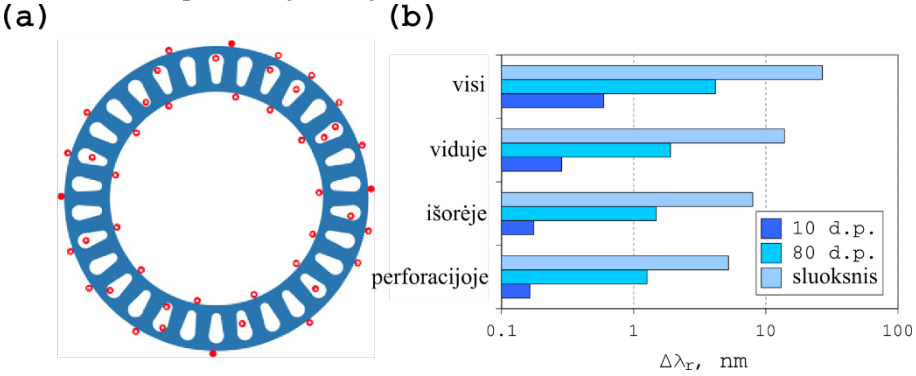

Pav. 11. Dielektrinių dalelių pasiskirstymas. a, Atsitiktinis dielektriko dalelių (raudona spalva) pasiskirstymas aplink perforuotą mikro žiedinį rezonatorių ir jo viduje. **b**, Kritimo prievado intensyvumo smailės poslinkis, kurį sukelia 10, 80 ir begalinis skaičius (imituojamas kaip sluoksnis) rezonatorių dengiančių dielektrinių dalelių, kai dielektrinės dalelės pasiskirsčiusios: vidiniame žiedo paviršiuje; išoriniame žiedo paviršiuje; defektų viduje (perforacijose); ir visuose paviršiuose.

Bendrai, šiame skyriuje lūžio rodiklio jutimui buvo pasiūlyta nauja mikro žiedinio rezonatoriaus struktūra su mažos dielektrinės skvarbos medžiagos defektais. Išnagrinėtas jos veikimas tūrinio ir paviršinio jutiklio schemose. Parodyta, kad pasiūlytas lūžio rodiklio jutiklis, pagrįstas mikro žiediniu

rezonatoriumi, yra pranašesnis už įprastus mikro žiedinius rezonatorius. Pateiktas perforuotas mikro žiedinis rezonatorius leidžia keisti kokybės koeficientą ir jautrumą, todėl jį galima pritaikyti daugelyje optikos sričių. Šia struktūra ne tik pasiekiamas didelis jautrumas, bet ir padidinamas bendras mikro žiedinio rezonatoriaus ir jį supančios terpės sąsajos plotas, todėl gali padidėti šviesos ir medžiagos sąveika su vandeninėmis terpėmis ir dujomis.

3.2 poskyryje pristatomas mikro žiedinis rezonatorius, kuris yra padengtas metalinių nano diskų grandinėle. Šis skyrius parengtas remiantis straipsniu: DOI: 10.1364/OL.40.002977 (© The Optical Society. Reproduced with permission. All rights reserved). Parodyta, kad šis mikro žiedinis rezonatorius leidžia tik vieną rezonansą, padidina sensoriaus jautrumą ir panaikina skylančias modas.

3.2.1 poskyryje pateiktas žiedinių mikro rezonatorių su aukso nano dalelių grandinėle aktualumas. 3.2.2 poskyryje pristatomi ir aptariami pagrindiniai rezultatai. 3.2.3 poskyryje pateikiamos skyriaus išvados.

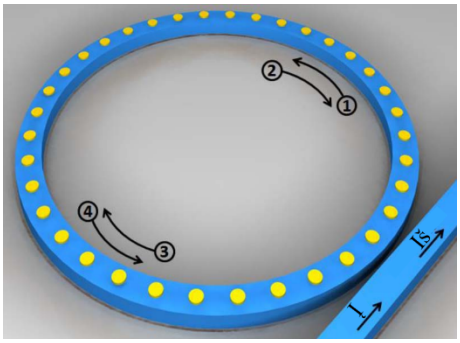

Pav. 12. Žiedinis mikro rezonatorius su aukso nano diskų grandinėle. 1 ir 3 rodyklės žymis sklindančias bangas, o 2 ir 4 rodyklės žymi priešpriešinss bangas.

Pateiktas rezonatoriaus (**Pav. 12**) veikia dėl to, kad aukso nano dalelės atitinka vienos modos rezonanso sąlygą. Dėl to visos kitos modos yra nuslopinamos įvestų papildomų aukso nuostolių. Dėl esančios grandinėlės rezonatoriuje nebelieka bėgančių bangų, likusi moda yra stovinti banga.

Pav. 13 pateikti paprasto ir aukso nano dalelių grandinėle dekoruoto mikro žiedinių rezonatorių pralaidumo spektrai. Matyti, kad lieka tik viena moda. Šios modos energiją galima keisti keičiant aukso nano dalelių skaičių (**Pav. 14**).

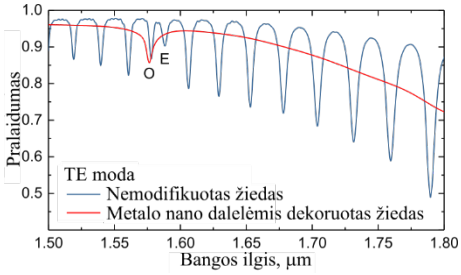

Pav. 13. Pralaidumo spektrai. Nemodifikuotų ir aukso nano diskų grandinėle modifikuotų žiedinių rezonatorių pralaidumo spektrai, esant TE poliarizacijai.

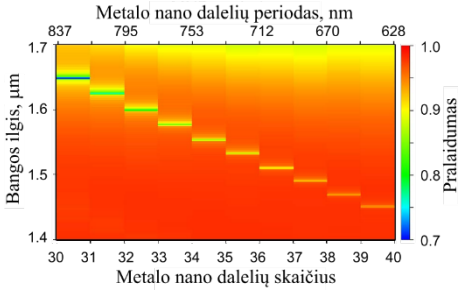

Pav. 14. Rezonansinio dažnio priklausomybė nuo metalo nano dalelių skaičiaus ir periodo. Spalva žymi pralaidumą.

Pav. 15ab pateikti žiedo palaikomo rezonanso elektromagnetinio lajuko pasiskirstymai. Matyti, kad ši moda mažai persikloja su aukso nano dalelėmis. Tuo tarpu net 10 nm nutolus nuo rezonanso matyti, kad elektromagnetinis laukas geriau persikloja su nano dalelėmis. Tai lemia didesnius nuostolius. Šis mechanizmas yra atsakingas už visų kitų modų išfiltravimą.

Keičiant aukso nano dalelių spindulį galima valdyti rezonanso padėtį, bei kokybės faktorių (**Pav. 16**). Didėjant aukso nano dalelėms mažėja efektyvus lūžio rodiklis (rezonansas slenkasi į mėlynąją pusę) ir mažėja jo kokybės faktorius (didėja modos persiklojimas su nano dalelėmis).

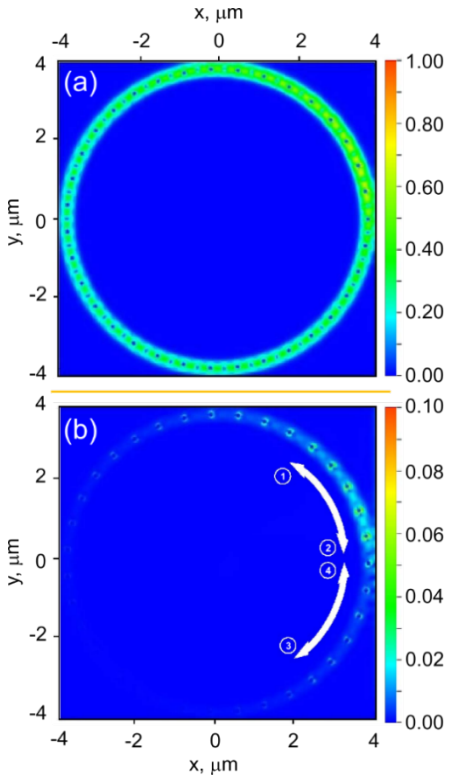

Pav. 15. Elektromagnetinio lauko sklidimas. a, TE modos intensyvumas ties rezonansiniu dažniu (35 aukso nano diskai). **b**, TE modos intensyvumas +10 nm nuo rezonanso. 1 ir 3 rodyklės žymi sklindančias bangas, o 2 ir 4 rodyklės - priešpriešiais sklindančias bangas. Lauko profiliai buvo paimti XY plokštumoje, ties aukso nano diskų viduriu. Spalva rodo lauko intensyvumą. Įvedimo bangolaidis yra vertikalus (šviesa sklinda išilgai y ašies) ir yra dešinėje žiedo pusėje pusėje.

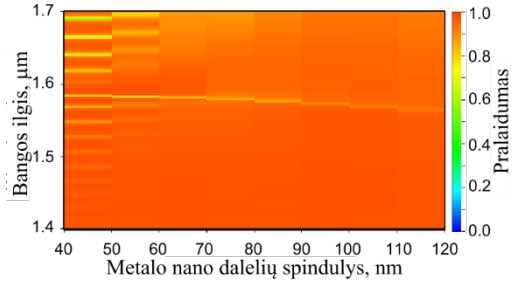

Pav. 16. Pralaidumo spektro priklausomybė nuo aukso dalelių spindulio (35 aukso nano dalelės). Spalvos atspindi pralaidumo intensyvumą.

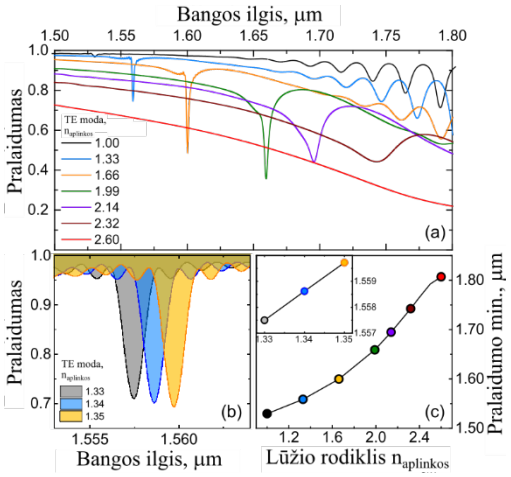

Pav. 17. Pralaidumo spektro priklausomybė nuo rezonatorių supančios medžiagos. a, Rezonansinės modos poslinkis dėl aplinkinės terpės (žiedas dekoruotas 35 aukso nano dalelėmis) lūžio rodiklio pokyčio. **b**, Rezonanso postūmis iš arti lūžio rodikliui kintant per 0,02. **c**, Rezonanso padėties priklausomybė nuo aplinkinės terpės lūžio rodiklio, gauta iš **a**. Intarpe pavaizduotas analogiškas jautrumo grafikas **b**.

Šiuos rezonatorius padengus kita medžiaga galima sukurti sensorių. **Pav. 17abc** rodo, kaip kinta rezonanso padėtis keičiantis aplinkiniam lūžio rodikliui. Akivaizdu, kad didėjant bangos ilgiui mažėja kokybės faktorius (didėja modos persiklojimas su aukso nano dalelėmis). Taip pat matyti, kad rezonatorius leidžia palaikomos modos kitimą nuo 1550 nm iki 1750 nm, kas leidžia naudotį ši prietaisą kaip savaiminio kalibravimo sensorių.

Apibendrinant, šis tyrimas patvirtina, jog metalo nano dalelių grandinėlė ant mikro žiedinio rezonatoriaus sukuria itin platų laisvąjį spektro diapazoną (padidintą viena eile), jį riboja tik bangolaidžio juostos plotis. Vidutinis prietaiso jautrumas yra apie ~176 nm/RIU ir yra 2 kartus geresnis nei nemodifikuoto analogo ~70 nm/RIU reikšmė. Gautos dispersinės gardelės filtravimo savybes galima tiksliai sureguliuoti keičiant žiedo ir nano diskų grandinės parametrus. Padidinus nano diskų spindulį, rezonansinė moda pasislenka į mėlynąją pusę ir susilpnėja. Kadangi auksas yra lengvai funkcionalizuojamas, prie tokių rezonatorių lengva prikabinti tiriamas medžiagas.

3.3 poskyryje aprašytas pagamintas mikro žiedinis rezonatorius, kuris yra perforuotas daline diskine gardele, kuri veikia kaip fotoninis kristalas. Šis skyrius parengtas remiantis straipsniu: DOI: 10.1364/OL.41.003655 (© The Optical Society. Reproduced with permission. All rights reserved). Parodyta, kad šis žiedinis mikro rezonatorius sutelkia elektromagnetinį lauką perforuotuose diskuose ir taip padidina tūrinį jautrumą.

3.3.1 poskyryje pateiktas žiedinių mikro rezonatorių su perforacijomis aktualumas. 3.3.2 poskyryje pristatomi ir aptariami pagrindiniai rezultatai. 3.3.3 poskyryje pateikiamos skyriaus išvados.

Prietaiso schema pateikta **Pav. 18.** Žiedinis mikro rezonatorius yra perforuotas diskais, kurie sudaro vienmatį fotoninį kristalą. Šio kristalo periodas parinktas taip, kad atsivertų draustinės juostos tarpas darbiniame rezonatoriaus bangos ilgių diapazone (1500-1600 nm). Tam, kad pagerinti šviesos įvedimą į rezonatorių bangolaidis yra dekoruotas tokia pačia gardele. Tai leidžia suderinti žiedo ir bangolaidžio modas bei pasiekti fazinę sinchronizmo sąlygą.

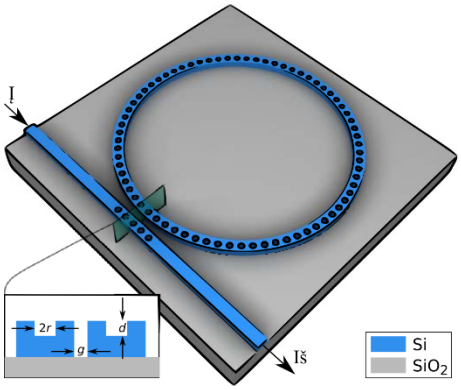

Pav. 18. Žiedinio mikro rezonatoriaus su fotoniniu kristalu geometrija. Intarpe pavaizduotas zonos skersinis pjūvis. Įterpinyje r reiškia skylės spindulį, d - skylės gylį, o g - jungties tarpą.

Pateiktas rezonatorius buvo pagamintas naudojantis ultravioletine litografija (**Pav. 19**). Minimalus perforuotų diskų diametras yra 130 nm (dėl gamybos metu naudojamo bangos ilgio).

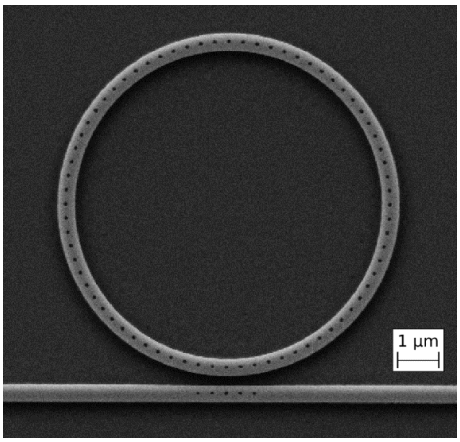

Pav. 19. Pagaminto žiedinio rezonatoriaus nuotrauka gauta elektronų pluošto mikroskopu.

Patį fotoninių kristalų gardelę galima sumodeliuoti pasitelkiant tikrinių verčių metodą. **Pav. 20** pateikta tokios gardelės dispersija. Šiuo atveju skaičiuojamas tik vienas gardelės elementas. Nepaisant to, yra daroma prielaida, kad gardelė yra begalinio ilgio. Matyti, kad juodos linijos, kurios žymi skirtingas modas, pažymėtos (1) ir (2) yra ties 1560 nm, kai $k_x = 0.5$ (banga šiuo atveju sklinda išilgai gardelės). Šioje vietoje susidaro draustinė juosta ir visa šviesa yra atspindima. Tai įvyksta dėl destruktyvios interferencijos tarp 1 ir 2 (priešingi faziniai greičiai).

Tame pačiame paveikslėlyje parodyti skirtingų modų profiliai. Matyti, kad 1 moda yra lokalizuota aukšto lūžio rodiklio medžiagoje, o 2 – perforuotuose diskuose (žemas lūžio rodiklis). Visos šios modos matomos ir eksperimente (**pav. 21abcd**). Keičiant išorinę terpę galime stebėti kaip rezonatoriaus palaikomos modos slenkasi į raudoną pusę (lūžio rodiklis didėja). **Pav. 22** parodyta kaip šie rezonansai kinta kintant išorinės terpės lūžio rodikliui. Verta paminėti, kad modos lokalizuotos perforuotuose diskuose rodo didesnį jautrumą.

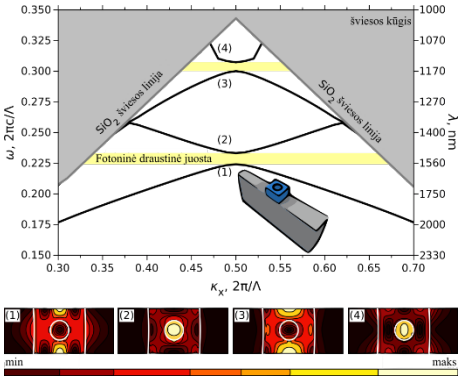

Pav. 20. Fotoninio kristalo dispersija. (1) ir (3) žymi dielektrines juostas, (2) ir (4) - oro juostas. Apatinėse lentelėse parodytas visų keturių juostų elektrinio lauko energijos tankio pasiskirstymas, kai $k_x = 0.49$.

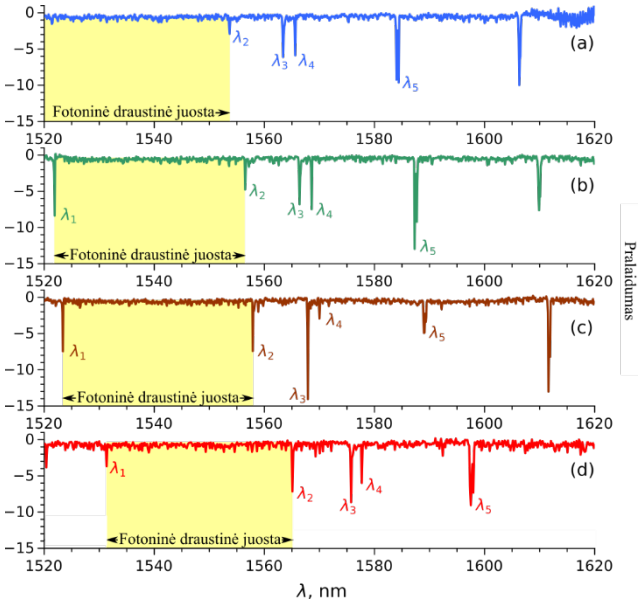

Pav. 21. Pralaidumo spektrai esant skirtingos rezonatorių supančioms terpėms. a, Metanolis, $n_{env} = 1.31$. **b**, Etanolis, $n_{env} = 1.35$. **c**, Izopropanolis, $n_{env} = 1.36$. **d**, Glicerolis, $n_{env} = 1.45$. Fotoninių kristalų indukuota draustinė juosta tęsiasi nuo λ_1 to λ_2. λ_1 rezonansas oro juostoje: λ_2, λ_3, λ_4, ir λ_5 yra rezonansai dielektrinėje juostoje.

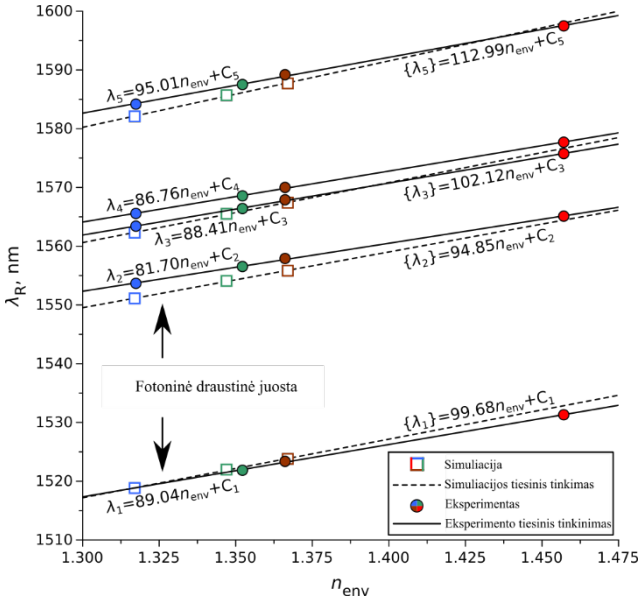

Pav. 22. Rezonansų pozicijų priklausomybė nuo išorinio lūžio rodiklio. Linijų lygtys, gautos atlikus tiesinį mažiausių kvadratų priderinimą, kur eksperimentiniai matavimai pažymėti λ_i, skaitmeninio modeliavimo rezultatai $\{\lambda_i\}$. Kiekvienos linijos nuolydis atitinka jautrumą (nm/RIU) vienetais.

Apibendrinant, buvo pademonstruotas naujas žiedinis mikro rezonatorius su integruotu vienmačiu fotoniniu kristalu, suformuotu iš dalinai išgraviruotų cilindrinių perforacijų. Parodyta, kad dėl didesnės modų lauko lokalizacijos fotoninio kristalo kiaurymės srityje oro juosta pasižymi didesniu jautrumu tūriniam lūžio rodikliui.

3.4 poskyryje aprašytas pagamintas žiedinis mikro rezonatorius, kuris yra perforuotas daline diskine gardele, kuri veikia kaip fotoninis kristalas. Parodyta, kad šio sensoriaus jautrumas ir matavimų ruožas yra didesnis lyginant su įprastu žiediniu rezonatoriumi bei kad šis žiedinis mikro rezonatorius sutelkia elektromagnetinį lauką perforuotuose diskuose ir taip padidina tūrinį jautrumą. Šis skyrius parengtas remiantis straipsniu: DOI: 10.1364/JOSAB.34.000750 (© The Optical Society. Reproduced with permission. All rights reserved).

3.4.1 poskyryje pateiktas žiedinių mikro rezonatorių su perforacijomis aktualumas. 3.4.2 poskyryje pateikiamas struktūros dizainas. 3.4.3 poskyryje aprašomas sensoriaus rezultatai. 3.4.4 poskyryje parodytas pagamintas rezonatorius. 3.4.5 poskyryje pateikiamos išvados.

Šiame darbe tirtas panašus į prieš tai skyriuje tirtą žiedinis rezonatorius. **Pav. 23** parodyta šio žiedinio mikro rezonatoriaus geometrija. Čia vienmatė gardelė suformuota iš dalinių žiedo išpjovimų. Ši geometrija dar labiau padidina terpės ir medžiagos sąveiką.

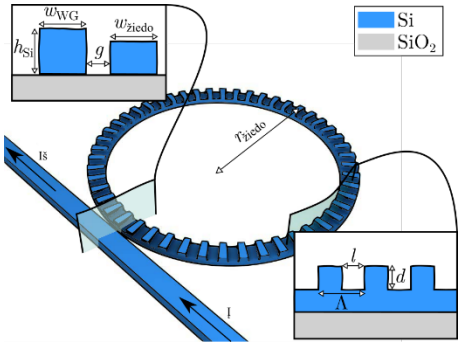

Pav. 23. Perforuoto žiedinio mikro rezonatoriaus geometrija. h_{Si} žymi silicio aukštį, w_{WG} — žymi bangolaidžio plotį, $w_{žiedo}$ — žymi žiedo plotį, g — atstumas tarp bangolaidžio ir šviesolaidžio, $r_{žiedo}$ — žiedo spindulys, d — perforacijos gylis, l — perforacijos ilgis ir Λ — periodas.

Atlikę skaičiavimus galime matyti, kad keičiant perforacijos ilgį ir gylį galime pasiekti rėžimą, kai žemiausios energijos moda išlieka toje pačioje vietoje (**pav. 24**). Tai, lyginant su diskais, teikia daugiau parametrų kuriant sensorių ir leidžia stabilizuoti rezonansu ties norima padėtimi. Verta paminėti, kad perforacijos gylis yra apibrėžtas gamybos technologijos.

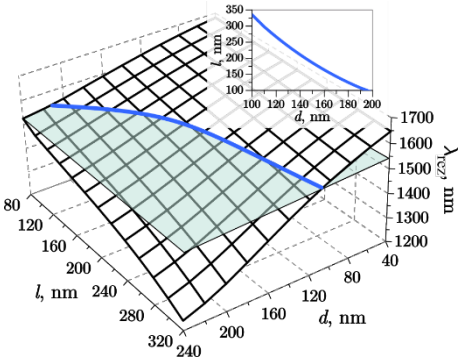

Pav. 24. Arčiausiai fotoninės juostos sandūros esančios modos rezonanso bangos ilgis kaip perforacijos ilgio (l) ir gylio (d) funkcija. Skaidri plokštuma pjauna paviršių ties λ_{rez} = 1540 nm.

Ši vienmatė gardelė sukuria draustinę juostą (**pav. 25**). Taigi galime tikėtis panašių reiškinių kaip ir prieš tai nagrinėtame darbe.

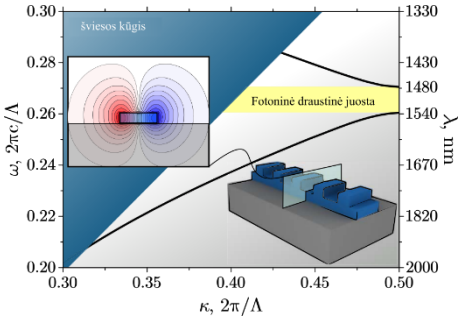

Pav. 25| Periodinio segmento, sudarančio 1D fotoninį kristalą žiedinio mikro rezonatoriaus viduje, dispersija (d = 120 nm). Intarpe parodytas elektrinio lauko vektoriaus komponentės pasiskirstymas statmenai sklidimo krypčiai.

Tam, kad sensorius būtu jautrus, mus domina riba, kai nebeįmanoma išmatuoti lūžio rodiklio pakitimo (matavimo riba). Tai pademonstruota **pav. 26**. Didėjant perforacijos elementui, didėja elektromagnetinio lauko sąveika su prietaisą supančia terpe ir tuo pačiu kyla rezonatoriaus jautrumas (**pav. 26a**). Dėl tos pačios priežasties didėja ir rezonatoriaus terminis atsakas (**pav. 26b**) bei mažėja kokybės faktorius (daugiau sklaidos, **pav. 26c**). Sudėję visus šiuos veiksnius kartu matome, kad matavimo riba išlieka panaši didėjant perforacijai. Tą patį galime pavaizduoti esant skirtingiems veiksniams (**pav. 27**).

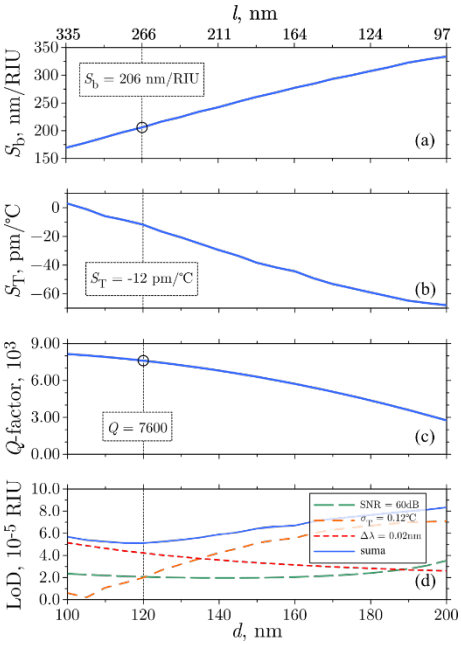

Pav. 26. Perforacijos gylio (su atitinkamu perforacijos ilgiu, kad būtų išlaikyta 1540 nm rezonanso padėtis) priklausomybė nuo pagrindinių mikro jutiklio parametrų. a, Tūrinio lūžio rodiklio jautrumas. **b**, Terminis stabilumas. **c**, kokybės faktorius. **d**, Aptikimo riba (Signal to Noise Ration, SNR), esant skirtingiems dominuojantiems veiksniams: SNR = 60 dB, temperatūros variacija — 0.12 laipsnių Celsijaus, spektrinė rezoliucija — 0.02 nm, visi kartu.

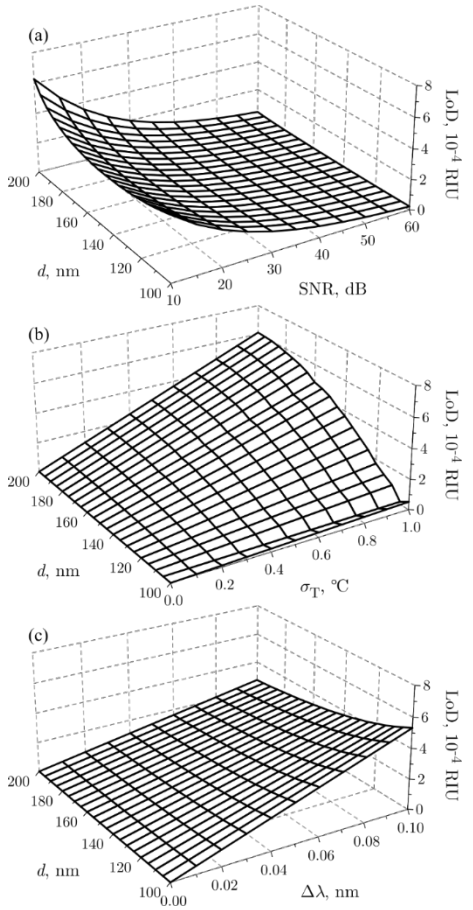

Pav. 27. Aptikimo riba (LoD), kuri lemta skirtingų veiksnių. a, Signalo triukšmo lygis, kinta nuo 10 iki 60 dB. **b**, σT ir **c**, Δλ.

Pagaminto rezonatoriaus nuotrauka pateikta **pav. 28**. Šis rezonatorius demonstruoja draustinės juostos tarpą bei puikiai atitinka teorinį skaičiavimą (**pav. 29ab**). Keičiant šį prietaisą supančią terpę galime nustatyti sensoriaus jautrumą (~200 nm/RIU). Taip pat matyti, kad didėjant bangos ilgiui jautrumas didėja. Taip yra dėl to, kad ilgesnio bangos ilgio modos yra mažiau sutelktos žiede ir labiau įsiskverbia į sensorių supančią terpę.

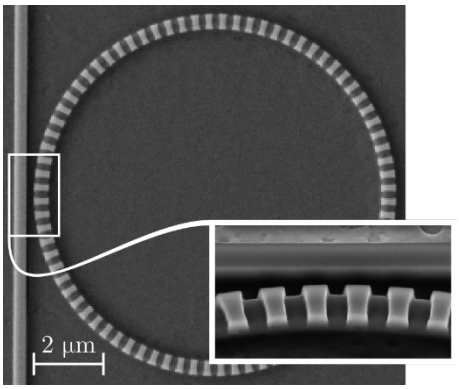

Pav. 28. Pagaminto žiedinio mikro rezonatoriaus vaizdas gautas skenuojančiu elektroniniu mikroskopu. Intarpe pavaizduotas padidintas tarpas tarp bangolaidžio ir žiedinio rezonatoriaus vaizdas.

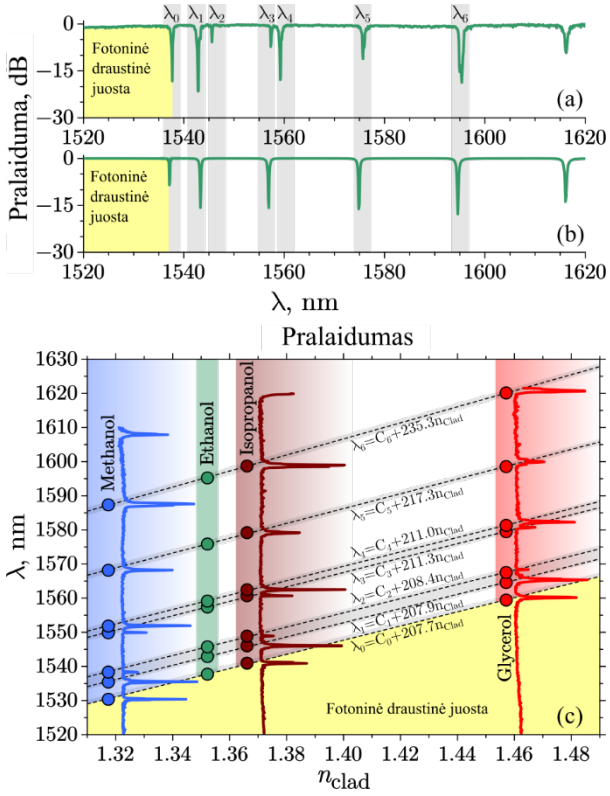

Pav. 29. Žiedinio mikro rezonatoriaus, įterpto į metanolį ir kitas medžiagas, perdavimo spektrai. a, Eksperimentas. **b**, Skaičiavimas. **c**, Rezonanso bangos ilgio padėtis ir pralaidumo spektrai esant skirtingoms apvalkalo medžiagoms.

Apibendrinant, atlikta žiedinio mikro rezonatoriaus su integruotu 1D fotoniniu kristalu analizė, siekiant padidinti jautrumą ir matavimo diapazoną. Perforacijų sukeltas fotoninis juostos tarpas gali būti naudojamas kaip spektrinė nuoroda, leidžianti įveikti laisvojo spektro diapazono apribojimą. Be to, parodyta, kad reguliuojant perforacijos gylį, aptikimo ribą galima sumažinti iki minimumo. Skaitinė analizė buvo patikrinta eksperimentais su pagaminta struktūra, naudojant organinius tirpiklius su skirtingais lūžio rodikliais.

Parodyta, kad kintamo ėsdinimo gylio savybės suteikia papildomą laisvės laipsnį projektuojant ir optimizuojant žiedinio mikro rezonatoriaus jutiklių įtaisus, nes jomis galima valdyti režimo poveikį supančiai terpei ir bendrą efektyvųjį lūžio rodiklį.

3.5 poskyryje aprašytas pagamintas žiedinis mikro rezonatorius, kuris yra perforuotas diskine antros eilės Brego gardele žiedo vidinėje dalyje. Parodyta, kad šis rezonatorius veikia panašiai kaip žiedinis mikro rezonatorius, kuris yra dekoruotas aukso nano diskų gardele. Papildomai matyti, kad šis žiedinis mikro rezonatorius sutelkia vienos modos elektromagnetinį lauką perforuotuose diskuose ir taip padidina tūrinį jautrumą bei nuslopina kitas modas, kurios sutelktos žiedo viduje.

3.5.1 poskyryje pateiktas žiedinių mikro rezonatorių su perforacijomis aktualumas. 3.5.2 poskyryje aprašyti metodai naudoti tyrimo metu. 3.5.3 poskyryje aprašomas sensoriaus rezultatai. 3.4.4 poskyryje parodytas pagamintas rezonatorius. 3.5.5 poskyryje pateikiamos išvados.

Pav. 5 parodyta kaip atrodo matavimo schema. Du šviesolaidžiai yra naudojami įvesti ir išvesti šviesai iš lusto. Pačio žiedinio rezonatoriaus schema pateikta **pav. 30**. Antros eilės Brego gardelė yra sudaryta žiedo viduje, kad persiklojimas su žiede sklindančia moda būtų minimalus. Šios struktūros pralaidumo spektrai pateikti **pav. 31**. Kintant perforacijų spinduliui, kinta pralaidomo spektras, kol galiausiai išnyksta visos modos ir lieka tik viena, kuri yra sutelkta perforacijų viduje (**pav. 32a**). Kitos modos, sklindančio žiedo viduje (**pav. 32b**), rezonatoriuje nesklinda dėl per didelių nuostolių.

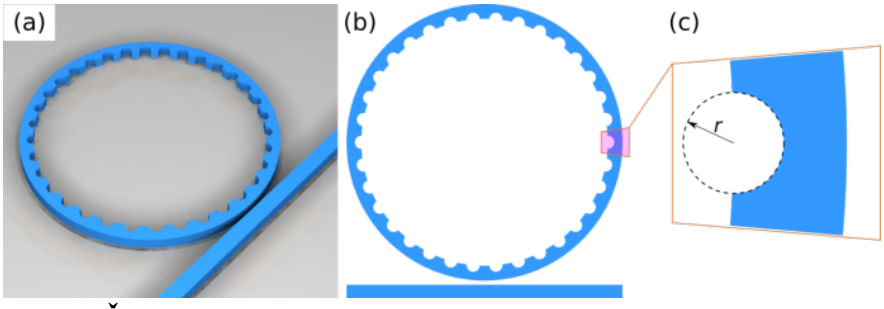

Pav. 30. Žiedinis mikro rezonatorius su antros eilės Brego gardele. a, Prietaiso schematika. **b**, vaizdas iš viršaus. **c**, vienas perforacijos elementas, kur r — perforacijos spindulys. Balta spalva žymi orą (n = 1) o mėlyna silicį (Si, n = 3.476), silicio aukštis - 220 nm.

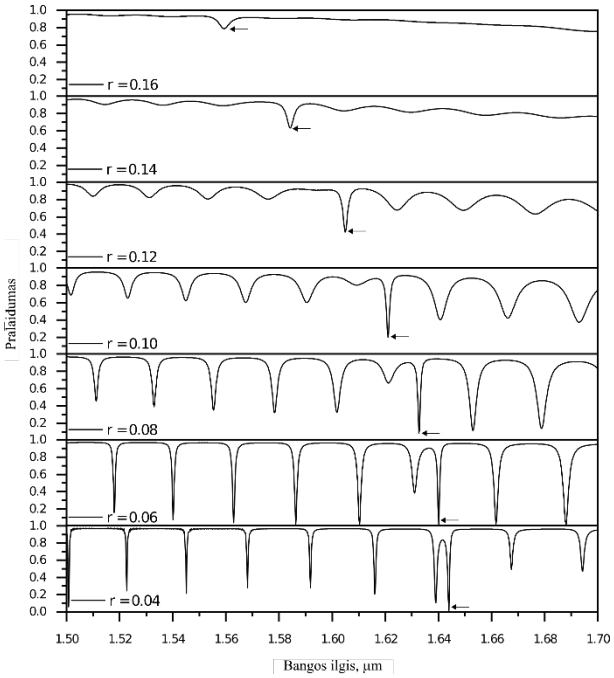

Pav. 31. Apskaičiuoti pralaidomo spektrai. Skirtingų žiedinių mikro rezonatorių pralaidumo spektrai su skirtingais perforacijų spinduliais r. Antros eilės Brego gardelės periodas yra 0,734 µm, o supanti terpė - PMMA (n = 1,481). Rodyklės rodo režimą, kai bangos vektorius k = 0 (šviesa sklinda iš rezonatoriaus kryptimi, kuri yra statmena lustui).

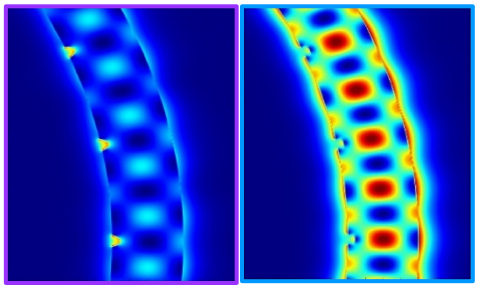

(a) (b)

Pav. 32. Elektromagnetinio lauko pasiskirstymas. Gardelės palaikomų modų intensyvumai: **a**, moda sutelkta perforacijose. **b**, moda sutelkta rezonatoriuje.

Pagaminta struktūra parodyta **pav. 33abcd**. Skirtingi žiediniai rezonatoriai turi perforacijas su skirtingais perforacijų spinduliais. Šių struktūrų pralaidumo spektrai pateikti **pav. 34**. Matyti, kad didėjant

perforacijų spinduliui išnyksta visos žiedinio rezonatoriaus modos be vienos, kuri yra sutelkta pačioje perforacijoje.

Šį prietaisą galima naudoti kaip sensorių, jį patalpinus į skirtingas terpes (**pav. 35**) bei dėl modų filtracijos naudoti jį kaip savaiminio kalibravimo prietaisą.

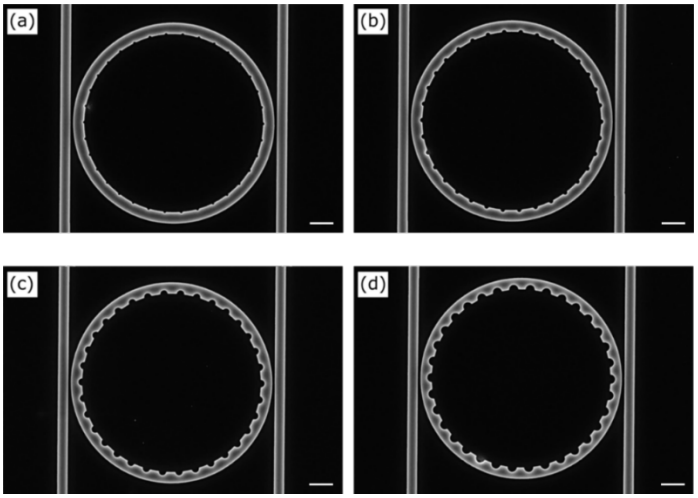

Pav. 33. Žiediniai mikro rezonatoriai turintys skirtingus perforacijų dydžiu r. Skenuojančio elektroninio mikroskopo. a, r = 40nm. **b**, r = 80 nm. **c**, r = 120 nm. **d**, r = 160 nm. Balta skalės juosta žymi 1 μm.

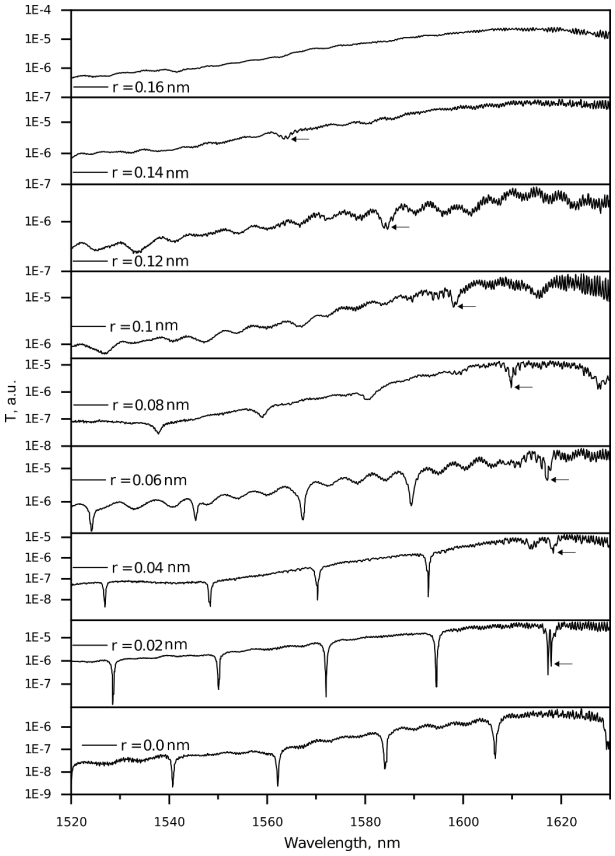

Pav. 34. Išmatuoti pralaidumo spektrai. Skirtingų žiedinių mikro rezonatorių pralaidumo spektrai su skirtingais perforacijų spinduliais r. Antros eilės Brego gardelės periodas yra 0,734 μm, o supanti terpė - PMMA (n = 1,481). Rodyklės rodo režimą, kai bangos vektorius k = 0 (šviesa sklinda iš rezonatoriaus kryptimi, kuri yra statmena lustui).

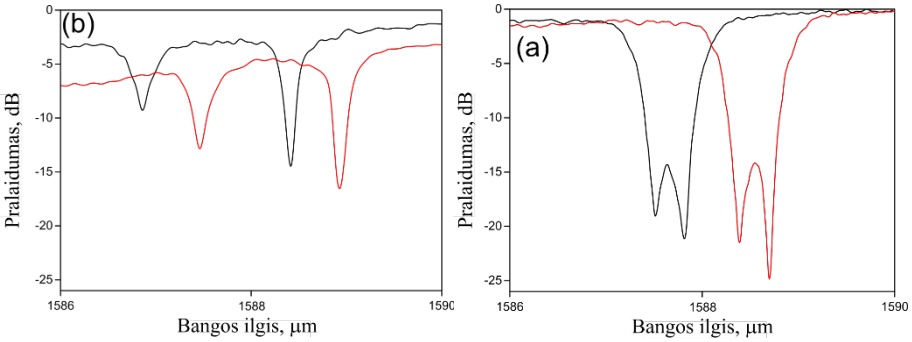

Pav. 35. Žiedinio mikro rezonatoriaus perdavimo spektrai esant skirtingoms terpėms. a, r = 20 nm. **b**, r = 40 nm. Čia juoda kreivė rodo perdavimo spektrą, kai aplinkinė medžiaga yra vanduo (n = 1,333), o raudona — 12 % glicerolis (n = 1,348).

Nustatyta, kad žiediniai mikro rezonatoriai su įdiegtomis antros eilės Brego gardelėmis turi geresnius kokybės koeficientus ir jautrumą išorinei apvalkalo aplinkai. Nuostoliais modifikuotų mikro jutikliai filtruoja nesuderintas modas, padidina jutiklio jautrumą ir laisvąjį spektrinį diapazoną, o tai yra naudinga kuriant savaiminio kalibravimo biologinius ir vandenilio dujų jutiklius.

- Suprojektuota ir pasiūlyta moderni žiedinio mikro rezonatoriaus struktūra su mažo lūžio rodiklio medžiagos defektais, kuri gali būti naudojama kaip efektyvus ir tūrinis lūžio rodiklio jutiklis. Parodyta, kad siūlomo lūžio rodiklio jutiklio jautrumas yra didesnis nei įprasto žiedinio mikro rezonatoriaus. Perforuotas žiedinis mikro rezonatorius leidžia valdyti kokybės koeficientą ir žiedo mikro jautrumą, todėl jutiklį galima derinti ir pritaikyti konkretiems naudojimo atvejams. Ši konstrukcija ne tik leidžia pasiekti didelį jautrumą, bet ir padidina bendrą mikro jutiklinio rezonatoriaus ir jį supančios terpės sąsajos plotą, todėl gali padidėti šviesos ir medžiagos sąveika su vandeninėmis terpėmis ir dujomis.

- Metalo nano diskų matricos ant žiedinio mikro rezonatoriaus sukuria naują itin plataus laisvojo spektro diapazono jutiklio platformą. Vidutinis prietaiso jautrumas yra ∼176 nm/RIU, t. y. 2 kartus didesnis už nemodifikuoto analogo ∼70 nm/RIU.

- Jutikliai buvo sukurti naudojant moderniausią elektronų ir jonų pluošto litografiją bangolaidžiams suformuoti, o vėliau, naudojant pakėlimo būdą, buvo uždėti metaliniai nano diskeliai [68]. Aukso nano diskai užtikrina funkcionalizavimo platformą, todėl siūloma konstrukcija yra labai selektyvus jutiklis.

- Žiedinis mikro rezonatorius su iš dalies išgraviruotu integruotu 1D fotoniniu kristalu, turinčiu 3D geometriją, yra gera alternatyva didesniam jautrumui ir matavimo diapazonui užtikrinti. Perforacijos sukeltas fotoninis juostos tarpas gali būti naudojamas kaip spektrinis etalonas, kad būtų įveikti laisvojo spektro diapazono nustatyti apribojimai. Aptikimo ribą galima sumažinti naudojant jutiklio geometrinius parametrus. Dalinio ėsdinimo savybės suteikia papildomą laisvės laipsnį projektuojant ir optimizuojant žiedinio mikro rezonatoriaus jutiklių įtaisus.

- Žiediniai rezonatoriai su įgyvendintomis antros Brego eilės grotelėmis pasižymi geresniu kokybės koeficientu ir jautrumu išorinei apvalkalo aplinkai. Nuostoliais modifikuoti žiediniai mikro rezonatoriai filtruoja palaikomas modas, didina jutiklio jautrumą ir įgalina jutiklius pasižyminčius savaiminiu kalibravimu.

CURRICULUM VITAE

About the author

Darius Urbonas was Born in 1989 in Šiauliai, Lithuania. In 2008 he graduated from Skaistgirys secondary school in Skaistgirys. In 2012 he received his bachelor's degree in Physics at the Faculty of Physics, Vilnius University. In 2014 he received his master's degree in Laser Physics and Optical Technologies at the Faculty of Physics, Vilnius University. In 2014 he started his doctoral studies at the Center for Physical Sciences and Technology. From 2015 he has been working as a researcher at IBM Research Europe-Zurich.

Apie autorių

Darius Urbonas gimė 1989 m. Šiauliuose, Lietuvoje. 2008 m. baigė Skaistgirio vidurinę mokyklą Skaistgiryje. 2012 m. Vilniaus universiteto Fizikos fakultete įgijo fizikos bakalauro laipsnį. 2014 m. Vilniaus universiteto Fizikos fakultete įgijo lazerių fizikos ir optinių technologijų magistro laipsnį. 2014 m. pradėjo doktorantūros studijas Fizinių ir technologijos mokslų centre. Nuo 2015 m. dirba mokslinį darbą IBM Research Europe-Zurich.

BIBLIOGRAPHY

1. R. Narayanaswamy, and O. S. Wolfbeis, *Optical Sensors* (New York: Springer, 2004).

2. M. S. McClellan, L. L. Domier, and R. C. Bailey, ”Label-free virus detection using silicon photonic microring resonators,” *Biosens Bioelectron.* **31** (1), 388–392 (2012).

3. M. S. Luchansky, and R. C. Bailey, “High-Q optical sensors for chemical and biological analysis,” *Anal. Chem.* **84**, 793-821 (2012).

4. X. Fan, I. M. White, S. I. Shopova, H. Zhu, J. D. Suter, and Y. Sun, ”Sensitive optical biosensors for unlabeled targets: a review,” *Anal. Chem. Acta.* **620** (1-2), 8-26 (2008).

5. W. Bogaerts, P. DeHeyn, T. Van Vaerenbergh, K. DeVos, S. K. Selvaraja, T. Claes, P. Dumon, P. Bienstman, D. Van Thourhout, and R. Baets, ”Silicon microring resonators,” *Laser Photon. Rev.* **6**, 47–73 (2012).

6. F. N. Xia, M. Rooks, L. Sekaric, and Y. Vlasov, ”Ultra-compact high order ring resonator filters using submicron silicon photonic wires for on-chip optical interconnects,” *Opt. Express* **15**, 11934–11941 (2007).

7. P. Dong, S. F. Preble, and M. Lipson, ”All-optical compact silicon comb switch,” *Opt. Express* 15, 9600–9605 (2007). 63 61

8. Q. F. Xu, B. Schmidt, S. Pradhan, and M. Lipson, “Micrometre-scale silicon electro-optic modulator,” *Nature* **435**, 325–327 (2005).

9. J. D. B. Bradley, E. S. Hosseini, T. N. Adam, Z. Su, G. Leake, D. Coolbaugh, and M. R. Watts, ”Monolithic erbium- and ytterbium-doped microring lasers on silicon chips,” *Opt. Express* **22** (10), 12226-12237 (2014).

10. S. L. McCall, A. F. J. Levi, R. E. Slusher, S. J. Pearton, and R. A. Logan, ”Whispering-gallery mode microdisk lasers,” *Appl. Phys. Lett.* **60**, 289 (1992).

11. Y. Sun and X. Fan, ” Optical ring resonators for biochemical and chemical sensing,” *Anal. Bioanal. Chem.* **399** (1), 205-211 (2011).

12. A. F. Gavela, D. G. García, J. Ramirez, and L. Lechuga, ”Last advances in silicon-based optical biosensors,” *Sensors* **16**, 285 (2016).

13. F. Vollmer, and L Yang, ”Label-free detection with high-Q microcavities: a review of biosensing mechanisms for integrated devices,” *Nanophotonics* **1**, 267–291 (2012).

14. J. Heebner, R. Grover, and T. Ibrahim, *Optical Microresonators: Theory, Fabrication and Applications, 1st ed., Springer Series in Optical Sciences* (Springer, 2008).

15. S. L. Chuang, *Physics of Photonic Devices, 2nd ed., Wiley Series in Pure and Applied Optics* (Wiley, 2009).

16. C.-Y. Chao, and L. J. Guo, ”Design and optimization of microring resonators in biochemical sensing applications,” *J. Lightwave Technol.* **24**, 1395–1402 (2006).

17. C. A. Barrios, ”Integrated microring resonator sensor arrays for labs-on-chip,” *Anal. Bioanal. Chem.* **403,** 1467-1475 (2012).

18. M. S. Luchansky, A. L. Washburn, T. A. Martin, M. Iqbal, L. C. Gunn, R. C. Bailey, ”Characterization of the evanescent field profile and bound mass sensitivity of a label-free silicon photonic microring resonator biosensing platform”, *Biosens. Bioelectron.* **26**, 1283–1291 (2010).

19. R. Orghici, P. Lützow, J. Burgmeier, J. Koch, H. Heidrich, W. Schade, N. Welschoff, S. Waldvogel, ”A microring mesonator sensor for sensitive detection of 1,3,5-trinitrotoluene (TNT)”, *Sensors* **10**, 6788–6795 (2010).

20. N. A. Yebo, P. Lommens, Z. Hens, and R. Baets, ”An integrated optic ethanol vapor sensor based on a silicon-on-insulator microring resonator coated with a porous ZnO film”, *Opt. Express* **18**, 11859–11866 (2010).

21. N. A. Yebo, D. Taillaert, J. Roels, D. Lahem, M. Debliquy, D. Van Thourhout, R. Baets, ”Silicon-on-insulator (SOI) ring resonator based integrated optical hydrogen sensor”, *IEEE Photon. Technol. Lett.* **21**, 960–962 (2009).

22. S. Matsuura, N. Yamasaku, Y. Nishijima, S, Okazaki, T. Arakawa, ”Characteristics of highly sensitive hydrogen sensor based on Pt-WO3/Si microring resonator”, *MDPI Sensors* **20**, 96 (2020).

23. C. A. Banios, K. B. Gylfason, B. Sanchez, A. Griol, H. Sohlstroem, M. Holgado, and R. Casquel, ”Slot waveguide biochemical sensor,” *Opt. Lett.* **32**, 3080-3082 (2007).

24. T. Claes, W. Bogaerts, and P. Bienstman, ”Vernier photonic sensor data-analysis,” *Opt. Lett.* **36** 3320–3322 (2011).

25. L. Jin, M. Li and J. J. He, ”Highly-sensitive silicon-on-insulator sensor based on two cascaded micro-ring resonators with vernier effect,” *Opt. Commun.* **284**, 156–159 (2011).

26. S. T. Fard, V. Donzella, S. A. Schmidt, J. Flueckiger, S. M. Grist, P. T. Fard, Y. Wu, R. J. Bojko, E. Kwok, N. A. F. Jaeger, D. M. Ratner, and L. Chrostowski, ”Performance of ultra-thin SOI-based resonators for sensing applications,” *Opt. Express* **22**, 14166–14179 (2014).

27. C. A. Barrios, K. B. Gylfason, B. Sánchez, A. Griol, H. Sohlström, M. Holgado, and R. Casquel, ”Slot-waveguide biochemical sensor,” *Opt. Lett.* **32**, 3080–3082 (2007).

28. S. A. Miller, Y. Okawachi, S. Ramelow, K. Luke, A. Dutt, A. Farsi, A. L. Gaeta, and M. Lipson, ”Tunable frequency combs based on dual microring resonators,” *Opt. Express* **23**, 21527-21540 (2015).

29. O. Gaathon, J. Culic-Viskota, M. Mihnev, I. Teraoka, and S. Arnold, ”Enhancing sensitivity of a whispering gallery mode biosensor by subwavelength confinement,” *Appl. Phys. Lett.* **89**, 223901 (2006).

30. J. G. Wangueemert-Perez, P. Cheben, A. Ortega-Monux, C. Alonso-Ramos, D. Perez-Galacho, R. Halir, I. Molina Fernandez, D.-X. Xu, and J. H. Schmid, ”Evanescent field waveguide sensing with subwavelength grating structures in silicon-on-insulator,” *Opt. Lett.* **39**, 4442-4445 (2014).

31. Z. Wang, X. Xu, D. Fan, Y. Wang, and R. T. Chen, ”High quality factor subwavelength grating waveguide micro-ring resonator based on trapezoidal silicon pillars,” *Opt. Lett.* **41**, 3375–3378 (2016).

32. Z. Tu, D. Gao, M. Zhang, D. Zhang, ”High-sensitivity complex refractive index sensing based on Fano resonance in the subwavelength grating waveguide micro-ring resonator,” *Opt. Express* **25**, 20911-20922 (2017).

33. F.-L. Hsiao and Y.-T. Ren, ”Computational study of slot photonic crystal ring-resonator for refractive index sensing,” *Sens. Actuators A* **205**, 53 –57 (2014).

34. J. Flueckiger, S. Schmidt, V. Donzella, A. Sherwali, D. M. Ratner, L. Chrostowski, and K. C. Cheung, ”Sub-wavelength grating for enhanced ring resonator biosensor,” *Opt. Express* **24**, 15672–15686 (2016).

35. T. Ma, L. Sun, J. Yuan, X. Sang, B. Yan, K. Wang, and C. Yu, ”Integrated label-free optical biochemical sensor with a large measurement range based on an angular grating-microring resonator,” *Appl. Opt.* **55**, 4784–4790 (2016).

36. S. M. Lo, S. Hu, G. Gaur, Y. Kostoulas, S. M. Weiss, P. M. Fauchet, ”Photonic crystal microring resonator for label-free biosensing,” *Opt. Express* **25**, 7046-7054 (2017).

37. N. Acharyya, M. Maher, G. Kozyreff, ”Portable microresonator-based label-free detector: monotonous resonance splitting with particle adsorption, ” *Opt. Express* **27**, 34997-35011 (2019).

38. R. Ahmed, A. A. Rifat, A. K. Yetisen, M. S. Salem, S.-H. Yun, and H. Butt, ”Optical microring resonator based corrosion sensing,” *RSC Adv.* **6**, 56127–56133 (2016).

39. K. R. Hiremath, J. Niegemann, and K. Busch, ”Analysis of light propagation in slotted resonator based systems via coupled-mode theory,” *Opt. Express* **19** (9), 8641–8655 (2011).

40. T. Claes, J. G. Molera, K. D. Vos, E. Schacht, R. Baets, and P. Bienstman, ”Label-free biosensing with a slot-waveguide-based ring resonator in silicon on insulator,” *IEEE Photon. J.* **1**, 197–204 (2009).

41. C. A. Barrios, M. J. Banuls, V. Gonzalez-Pedro, K. B. Gylfason, B. Sanchez, A. Griol, A. Maquieira, H. Sohlstrom, H. Holgado, and R. Casquel, ”Label-free optical biosensing with slot-waveguides,” *Opt. Lett.* **33**, 708–710 (2008).

42. M. Khorasaninejad, N. Clarke, M. P. Anantram, and S. S. Saini, ”Optical bio-chemical sensors on SNOW ring resonators,” *Opt. Express* **19** (18), 17575-17584 (2011).

43. Li, Q. Huang, and W. Bogaerts, ”Design of a single all-silicon ring resonator with a 150 nm free spectral range and a 100 nm tuning range around 1550 nm,” *Photon. Res.* 4, 84 –92 (2016).

44. M. Born and E. Wolf, *Principles of Optics* (Pergamon Press, 1959).

45. Jackson, J. D., *Classical Electrodynamics, 3rd Edition* (John Wiley and Sons, 1999).

46. P. J. Bock, P. Cheben, J. H. Schmid, J. Lapointe, A. Delâge, S. Janz, G. C. Aers, D.-X. Xu, A. Densmore, and T. J. Hall. ” Subwavelength grating periodic structures in silicon-on-

insulator: a new type of microphotonic waveguide," *Opt. Express* **18**, 20251-20262 (2010).

47. M. S. Skolnick, T. A. Fisher and D. M. Whittaker, " Strong coupling phenomena in quantum microcavity structures," *Semicond. Sci. technol.* **13**, 645-669 (1998).

48. I. Chremmos, O. Schwelb, and N. Uzunoglu, *Photonic Microresonator Research and Applications* (New York: Springer, 2010).

49. Y. Guo, Y. Guo, C. Li, H. Zhang, X. Zhou, and L. Zhang, " Integrated Optical Phased Arrays for Beam Forming and Steering," *Appl. Sci.* **11**, 4017 (2021).

50. S. Geidel, S. P. Llopis, M. Rodrigo, G. de Diego-Castilla, A. Sousa, J. Nestler, T. Otto, T. Gessner and V, Parro, "Integration of an Optical Ring Resonator Biosensorinto a Self-Contained Microfluidic Cartridge with Active, Single-Shot Micropumps," *Micromachines* **7** (153), (2016).

51. A. F. Oskooi, D. Roundy, M. Ibanescu, P. Bermel, J. D. Joannopoulos, and S. G. Johnson, "MEEP: A flexible free-software package for electromagnetic simulations by the FDTD method," *Comput. Phys. Commun.* **181**, 687–702 (2010).

52. S. G. Johnson and J. D. Joannopoulos, "Block-iterative frequency-domain methods for Maxwell's equations in a planewave basis," *Opt. Express* **8**, 173-190 (2001).

53. Ossila: https://www.ossila.com/pages/spin-coating

54. Wikipedia: https://en.wikipedia.org/wiki/Polydimethylsiloxane

55. L. H. Gabrielli, D. Liu, S. G. Johnson, and M. Lipson, "On-chip transformation optics for multimode waveguide bends," *Nat. Commun.* **3**, 1217 (2012).

56. A. F. Oskooi, C. Kottke and S. G. Johnson, ”Accurate finite-difference time-domain simulation of anisotropic media by subpixel smoothing,” *Opt. Lett.* **34** (18), 2778–2780 (2009).

57. A. Haddadpour, and Y. Yi, ”Metallic nanoparticle on micro ring resonator for bio optical detection and sensing,” *Biomed Opt. Express* **1** (2), 378–384 (2010).

58. X. Cai, J. Wang, M. J. Strain, B. Johnson-Morris, J. Zhu, M. Sorel, J. L. O’Brien, M. G. Thompson, S. Yu, ”Integrated Compact Optical Vortex Beam Emitters,” *Science* **338**, 263 – 366 (2012).

59. S. Werquin, S. Verstuyft, and P. Bienstman, ”Integrated interferometric approach to solve microring resonance splitting in biosensor applications,” *Opt. Express* **21**, 16955 (2013).

60. S. V. Boriskina, T. M. Benson, P. Sewell, and A. I. Nosich, ”Directional emission, increased free spectral range, and mode Q-factors in 2-D wavelength-scale optical microcavity structures.” *IEEEJ. Sel. Top. Quantum Electron.* **12**, 1175-1182 (2006).

61. M. Fujita and T. Baba, ”Microgear laser,” *Appl. Phys. Lett.* **80**, 2051 (2002).

62. S. Qiu, J. Cai, Y. Li, and Z. Han, ”Q-factor instability and its explanation in the staircased FDTD simulation of high-Q circular cavity,“ *Opt. Commun.* **277**, 406-410 (2010).

63. E. Simsek, ”Full analytical model for obtaining surface plasmon resonance modes,” *Opt. Express* **18** (2), 1722-1733 (2010).

64. M. Février, P. Gogol, A. Aassime, R. Mégy, C. Delacour, A. Chelnokov, A. Apuzzo, S. Blaize, J. M. Lourtioz, and B. Dagens, ”Giant Coupling Effect between Metal Nanoparticle Chain and Optical Waveguide,” *Nano Lett.* **12**, 1032-1037 (2012).

65. R. Quidant, C. Girard, J. C. Weeber, and A. Dereux, ”Tailoring the transmittance of integrated optical waveguides with short metallic nanoparticle chains,” *Phys. Rev.* B **69**, 085407 (2004).

66. M. Fevrier, P. Gogol, A. Aassime, R. Megy, D. Bouville, J. M. Lourtioz, and B. Dagens, ”Metallic nanoparticle chains on dielectric waveguides: coupled and uncoupled situations compared,“ *Appl. Phys. A* **109**, 935 (2012).

67. Y. Nishijima, Y. Hashimoto, L. Rosa, J. B. Khurgin, and S. Juodkazis, ”Scaling Rules of SERS Intensity,” *Adv. Opt. Mater.* **2**, 382 (2014).

68. K. Ueno, S. Juodkazis, V. Mizeikis, K. Sasaki, and H. Misawa, ”Clusters of Closely Spaced Gold Nanoparticles as a Source of Two-Photon Photoluminescence at Visible Wavelengths,“ *Adv. Mater.* **20**, 26-30 (2008).

69. M. Soljačić, E. Lidorikis, L. V. Hau, and J. D. Joannopoulos, ”Enhancement of microcavity lifetimes using highly dispersive materials,” *Phys. Rev. E* **71**, 026602 (2005).

70. D. Goldring, U. Levy, and D. Mendlovic, ”Highly dispersive micro-ring resonator based on one dimensional photonic crystal waveguide design and analysis,” *Opt. Express* **15**, 3156-3168 (2007).

71. J. D. Joannopoulos, S. G. Johnson, J. N. Winn, and R. D. Meade, *Photonic Crystals: Molding the Flow of Light, 2nd ed.* (Princeton University, 2008).

72. C. E. Campanella, A. Giorgini, S. Avino, P. Malara, R. Zullo, G. Gagliardi, and P. D. Natale, ”Localized strain sensing with fiber Bragg-grating ring cavities,” *Opt. Express* **21**, 29435-29441 (2013).

73. J. Wang, I. Glesk, and L. R. Chen, ”Subwavelength grating filtering devices,” *Opt. Express* **22**, 15335-15345 (2014).

74. A. Arbabi, Y. M. Kang, C.-Y. Lu, E. Chow, and L. L. Goddard, ”Realization of a narrowband single wavelength microring mirror,” *Appl. Phys. Lett.* **99**, 091105 (2011).

75. T. W. Lu, W. C. Tsai, T. Y. Wu, and P. T. Lee, ”Laser emissions from one-dimensional photonic crystal rings on silicon-dioxide,” *Appl. Phys. Lett.* **102**, 051103 (2013).

76. S. M. Lo, S. Hu, S. M. Weiss, and P. M. Fauchet, ”Photonic crystal microring resonator based sensors,” *in Conference on Lasers and Electro-Optics: 2014* (Optical Society of America, 2014).

77. G. Gao, Y. Zhang, H. Zhang, Y. Wang, Q. Huang, and J. Xia, *Sci. Rep.* **6**, 1 (2015).

78. J. W. Hoste, S. Werquin, T. Claes, and P. Bienstman, ”Conformational analysis of proteins with a dual polarisation silicon microring,” *Opt. Express* **22**, 2807–2820 (2014).

79. P. Liu, and Y. Shi, ”Simultaneous measurement of refractive index and temperature using a dual polarization ring,” *Appl. Opt.* **55** (13), 3537-3541 (2016).

80. Z. Han, P. Zhang, and S. I. Bozhevolnyi, ”Calculation of bending losses for highly confined modes of optical waveguides with transformation optics,” *Opt. Lett.* **38**, 1778-1780 (2013).

81. A. Farjadpour, D. Roundy, A. Rodriguez, M. Ibanescu, P. Bermel, J. D. Joannopoulos, S. G. Johnson, and G. Burr, ”Improving accuracy by subpixel smoothing in FDTD,” *Opt. Lett.* **31**, 2972–2974 (2006).

82. J. E. Saunders, C. Sanders, H. Chen, and H.-P. Loock, ”Refractive indices of common solvents and solutions at 1550 nm,” *Appl. Opt.* **55**, 947–953 (2016).

83. H. H. Li, ”Refractive index of silicon and germanium and its wavelength and temperature derivatives,” *J. Phys. Chem. Ref. Data* **9**, 561–658 (1980).

84. H. Malitson, ”Interspecimen comparison of the refractive index of fused silica,” *J. Opt. Soc. Am.* **55**, 1205–1209 (1965).

85. P. Seidler, K. Lister, U. Drechsler, J. Hofrichter, and T. Stöferle, ”Slotted photonic crystal nanobeam cavity with an ultrahigh quality factor-to-mode volume ratio,” *Opt. Express* **21**, 32468 (2013).

86. S. Blaize, F. Gesuele, I. Stefanon, A. Bruyant, G. Lérondel, P. Royer, B. Martin, A. Morand, P. Benech, and J.-M. Fedeli, ”Real-space observation of spectral degeneracy breaking in a waveguide-coupled disk microresonator,” *Opt. Lett.* **35**, 3168–3170 (2010).

87. J. G. Wangüemert-Pérez, P. Cheben, A. Ortega-Moñux, C. Alonso Ramos, D. Pérez-Galacho, R. Halir, I. Molina-Fernández, D.-X. Xu, and J. H. Schmid, ”Evanescent field waveguide sensing with subwavelength grating structures in silicon-on-insulator,” *Opt. Lett.* **39**, 4442–4445 (2014).

88. R. Ahmed, A. A. Rifat, A. K. Yetisen, S. H. Yun, S. Khan, and H. Butt, ”Mode-multiplexed waveguide sensor,” *J. Electromagn. Waves Appl.* **30**, 444–455 (2016).

89. Y. Xu and J. Xiao, ”Ultracompact and high efficient silicon-based polarization splitter-rotator using a partially-etched subwavelength grating coupler,” *Sci. Rep.* **6**, 27949 (2016).

90. C. Li, H. Zhang, M. Yu, and G. Q. Lo, ”CMOS-compatible high efficiency double-etched apodized waveguide grating coupler,” *Opt. Express* **21**, 7868–7874 (2013).

91. S. G. Johnson and J. D. Joannopoulos, ”Block-iterative frequencydomain methods for Maxwell’s equations in a plane wave basis,” *Opt. Express* **8**, 173–190 (2001).

92. L. Chrostowski, S. Grist, J. Flueckiger, W. Shi, X. Wang, E. Ouellet, H. Yun, M. Webb, B. Nie, Z. Liang, K. C. Cheung, S. A. Schmidt, D. M. Ratner, and N. A. F. Jaeger, ”Silicon photonic resonator sensors and devices,” in Laser Resonators,

Microresonators, and Beam Control XIV, A. V. Kudryashov, A. H. Paxton, and V. S. Ilchenko, eds. (SPIE, 2012).

93. I. M. White, and X. Fan, ”On the performance quantification of resonant refractive index sensors,” *Opt. Express* **16**, 1020–1028 (2008).

94. T. Yoshie, L. Tang, and S.-Y. Su, ”Optical microcavity: sensing down to single molecules and atoms,” *Sensors* **11**, 1972–1991 (2011).

95. H. P. Loock and P. D.Wentzell, ”Detection limits of chemical sensors: applications and misapplications,” *Sens. Actuators B* **173**, 157–163 (2012).

96. Q. Xu, D. Fattal, and R. G. Beausoleil, ”Silicon microring resonators with 1.5-μm radius,” *Opt. Express* **16**, 4309–4315 (2008).

97. Y. H. Kim, S. J. Park, S. W. Jeon, S. Ju, C. S. Park, W. T. Han, and B. H. Lee, ”Thermo-optic coefficient measurement of liquids based on simultaneous temperature and refractive index sensing capability of a two-mode fiber interferometric probe,” *Opt. Express* **20**, 23744–23754 (2012).

98. Li, T. Van Vaerenbergh, P. De Heyn, P. Bienstman, and W. Bogaerts, ”Backscattering in silicon microring resonators: a quantitative analysis,” *Laser Photon. Rev.* **10**, 420–431 (2016).

99. A. Taflove and S. C. Hagness, *Computational Electromagnetics: The Finite-Difference Time-Domain Method* (Artech House, Boston, 2005) p.852.

100. A. Balcytis, G. Seniutinas, D. Urbonas, M. Gabalis, K. Vaskevicius. R. Petruskevicius, G. Molis, G. Valusis, S. Juodkazis, ”High precision fabrication of antennas and sensors, ” *SPIE Proc.* **9446**, 94461G (2015).

101. X. Xu, H. Subbaraman, J. Covey, D. Kwong, A. Hosseini, and R. T. Chen, ”Complementary metal–oxide–semiconductor

compatible high efficiency subwavelength grating couplers for silicon integrated photonics, ” *Appl. Phys. Lett.* **101**, 031109 (2012).

102. S. V. Boriskina, L. D. Negro, ”Self-referenced photonic molecule bio (chemical) sensor,” *Opt. Lett.* **35**, 2496-2498 (2010).

103. C. M. Campanella, M. Dunai, L. Calabrese, C. E. Campanella, ”Design guidelines for nanoparticle chemical sensors based on mode-splitting silicon-on-insulator planar microcavities, ” *JOSA B* **33**, 2383-2394 (2016).

104. C. E. Campanella, M. De Carlo, A. Cuccovillo, F. De Leonardis, V. M. N. Passaro, ”Methane gas photonic sensor based on resonant coupled cavities, ” *MDPI Sensors* **19**, 5171 (2019).

105. P. Malara, C. E. Campanella, A. Giorgini, S. Avino, P. De Natale, G. Gagliardi, ”Super-resonant intracavity coherent absorption, ” *Scie. Rep.* **6**, 28947 (2016).

106. W. R. Sweeney, C. W. Hsu, S. Rotter, A. D. Stone, ”Perfectly absorbing exceptional points and chiral absorbers, ” *Phys. Rev. Lett.* **122**, 093901 (2019).

107. Q. Zhong, J. Ren, M. Khajavikhan, D. N. Christodoulides, Ş. K. Özdemir, R. El-Ganainy, ”Sensing with exceptional surfaces in order to combine sensitivity with robustness, ” *Phys. Rev. Lett.* **122**, 153902 (2019).

DOI: 10.1088/2040-8978/16/10/105003
© IOP Publishing. Reproduced with permission. All rights reserved

IOPscience iopscience.iop.org

Home Search Collections Journals About Contact us My IOPscience

A perforated microring resonator for optical sensing applications

This content has been downloaded from IOPscience. Please scroll down to see the full text.

View the table of contents for this issue, or go to the journal homepage for more

Download details:

IP Address: 193.219.49.161
This content was downloaded on 01/09/2014 at 05:00

Please note that terms and conditions apply.

IOP Publishing Journal of Optics
J. Opt. **16** (2014) 105003 (6pp) doi:10.1088/2040-8978/16/10/105003

A perforated microring resonator for optical sensing applications

M Gabalis, D Urbonas and R Petruskevicius

Center for Physical Sciences and Technology, Savanoriu Ave. 231, LT-02300 Vilnius, Lithuania

E-mail: gysliukas@zoho.com

Received 24 April 2014, revised 8 June 2014
Accepted for publication 27 June 2014
Published 27 August 2014

Abstract

In this paper, we present numerical simulations of a refractive index sensor based on a perforated optical microring resonator. We show that the introduction of subwavelength perforations in the microring resonator increases the light–matter interaction and the sensitivity of the microring resonator. Here, the sensor performance is analyzed in two sensing schemes: bulk sensing and dielectric particle sensing. In both applications the perforated microring resonator sensor outperforms an ordinary microring resonator sensor and also maintains a high quality factor. The simulations were performed using finite-difference time domain and finite-element methods.

Keywords: microring resonator, nanostructures, refractive index sensor

(Some figures may appear in colour only in the online journal)

1. Introduction

Optical biochemical sensors, which provide detection and quantification of biochemical analytes, have emerged as a field of great interest because of the tremendous needs in early-stage disease diagnosis, pharmaceuticals, security, food quality control and environmental testing [1].

Among the various optical sensing devices, refractive index sensors have emerged as promising technology in the past few years. With these devices, the average refractive index change associated with binding of the sensing object is monitored [2]. Refractive index sensors allow label-free, real-time and direct detection of the molecular interaction at a dielectric interface. Although there are many different refractive index sensors [3], high quality factor (Q) optical sensors based on multiple-photon-passage microstructures perhaps constitute the most sensitive and promising class of label-free sensors. The Q factor of a given device is a measure of the photon lifetime within the structure. Larger Q means longer lifetime. The major advantages of the high Q factor include the multiple-pass interaction of propagating electromagnetic radiation with the respective analyte and narrow resonance linewidth, allowing resolving small resonance wavelength shifts due to the small change in refractive index induced by the analytes.

Among the high Q optical sensors, microring resonators have several particularly attractive properties: they provide low insertion loss, single-mode operation and small size. Biochemical sensors based on silicon on insulator (SOI) microring resonators have been studied extensively [4, 5]. But an ordinary microring resonator does not have high bulk sensitivity. This can be attributed to the strong confinement of light in the core material. It is possible to increase the bulk sensitivity by utilizing the Vernier effect [6, 7]. But this approach requires using a system of two or more rings with slightly different radii, and the radius of each ring must be relatively large (of the order of several tens of microns), so the free spectral range would be quite small. There have also been reports on increasing the sensitivity by adding a polymer layer at the resonator surface [8]. Another way to enhance the light in the cladding material is via the introduction of average refractive index modulation. Several microring geometries based on this strategy have been reported: the slotted microring resonator [9–12] (sensitivity up to 350 nm/RIU), and the SNOW microring resonator [13] (theoretical sensitivity up to 350 nm/RIU).

In this paper we present numerical simulations of novel microring resonator geometry, based on modulation of the average refractive index in the core material. We introduce subwavelength hollow core defects inside the core material in

 © 2014 IOP Publishing Ltd Printed in the UK

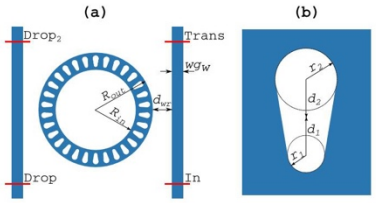

Figure 1. (a) Schematic diagram of a four-port device with two straight waveguides and a perforated microring resonator. (b) Enlarged portion of the resonator, showing the detailed geometry of the defects.

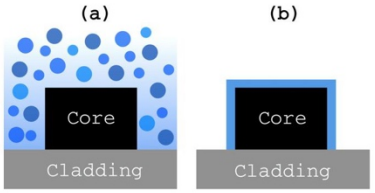

Figure 2. Sensing mechanisms: (a) homogeneous sensing; (b) surface sensing.

order to increase the surface area of the resonator and the light–matter interaction.

2. The perforated microring resonator and simulation methods

A schematic diagram of a four-port device based on a perforated microring resonator is presented in figure 1(a). The resonator consists of a ring with outer radius R_{out}, inner radius R_{in}, and refractive index n_c. The ring contains a total number N_d of low dielectric constant material (refractive index $n_s < n_c$) hollow core defects. The detailed geometry of the defects is shown in figure 1(b).

The resonator is coupled to two identical straight waveguides with width wg_w and refractive index n_c. The entire device is embedded in a host material with refractive index n_s. The computational window is surrounded with PML (perfectly matched layers).

Defects are made from two connected cylinders (figure 1(b)). The radius of the inner cylinder is r_1 and the radius of the outer cylinder is r_2. The distance from the middle of the ring (defined as $(R_{out} + R_{in})/2$) to the center of the inner cylinder is d_1, and that to the center of the outer cylinder is d_2.

The angularly averaged refractive index for our structure would be a function of the radial coordinate. Different defect parameters would result in different average refractive index distributions. So in principle, an effect of the gradient refractive index similar to that obtained with grayscale lithography can be achieved [14]. As for the refractive index sensor, perforations increase the area in which the propagating mode interacts with the surrounding medium. Also, due to the lower mode confinement inside the core material, the evanescent field extends further into the surroundings. Both effects increase the sensitivity of the refractive index sensor. It can be noted that one drawback of an ordinary microring resonator is that the evanescent field does not extend far from the core material. So our design overcomes this drawback.

To model the perforated microring resonator, two-dimensional FDTD (with free software package MEEP [15]) and FEM (with the commercial Comsol Multiphysics software) simulations were performed. We mainly used FDTD to get drop port intensity spectra, since FDTD allows us to easily obtain the system response to a wide wavelength pulse. FEM was used to get steady state solutions at a particular excitation frequency, assuming an $\exp(i\omega t)$ time dependence of the electromagnetic field, where i is the imaginary unit, ω is the angular frequency and t is the time. One advantage that FEM has over FDTD is its flexibility in using a non-uniform mesh. We used FEM to check the results obtained with FDTD.

While the full three-dimensional simulations are necessary for determining parameters of the device, as intended for use in real world applications, two-dimensional simulations can also provide some insight into the structure of the resonator and its performance. Also as the geometry of the structure becomes complicated, with finer details, a smaller grid step size is required. Thus simulations of a structure with fine details in 3D become time-consuming. So most of the results presented in this article came from 2D simulations. However, at the end of the article we present the results of a few 3D simulations that show the possibility of getting the same performance in 3D as in 2D by changing some of the geometrical parameters of our structure.

The measure of resonator performance was based on calculations of two parameters: the sensitivity (S) and the quality factor (Q). Basically there are two sensing mechanisms that are commonly used: surface sensing and bulk (or volume) sensing [4, 5]. Bulk sensing is based on detecting the change of the average refractive index which is induced by the presence of analytes in the whole evanescent field region (figure 2(a)). Surface sensing is based on the amount of analytes distributed on top of the microring resonator, which can be interpreted as a thin coating covering the core (figure 2(b)). The shift of resonance wavelength which is induced by homogeneous distribution of analytes in aqueous cladding or deposition of analytes on the surface of a resonator is monitored. The main parameter describing the sensor's performance is the sensitivity S, which is defined as the change in resonance wavelength per refractive index unit (RIU) [5]:

$$S = \Delta\lambda_r/\Delta n \tag{1}$$

where $\Delta\lambda_r$ stands for the shift of resonance wavelength and Δn is the change of the cladding refractive index. The

smallest detectable wavelength shift does not depend on the resonance bandwidth or the resonance shape and should be determined by the resolution. However, noise can modify the resonance spectrum, so accurate detection of the resonance wavelength shift becomes difficult for a broad resonance lineshape. To enhance the accuracy, a narrower resonance is required, which in turn means that a higher Q value of the resonator is required. The Q factor can be defined as [16]

$$Q = \lambda_r / \Delta\lambda_{FWHM} \tag{2}$$

where λ_r stands for the resonance wavelength and $\Delta\lambda_{FWHM}$ stands for the resonance width at half-maximum of the resonance.

3. Results and discussion

The description of the defects that we are using allows a wide range of different perforation geometries. For example, setting $d_1 = d_2 = r_w$ and $r_1 = r_2$ we obtain layers of alternating low and high refractive indices. If $d_1 = d_2 = 0$ and $r_1 = r_2$ we get circular holes centered in the core material. We decided to aim for a design which has both a relatively high Q factor and a relatively high sensitivity, and has a resonance close to $\lambda = 1.55\,\mu$m. After performing a number of simulations, we observed that as the area of the defect gets larger, the Q factor decreases, and the sensitivity increases. We fixed the parameters of the waveguide and the ring itself to: $R_{out} = 2.2\,\mu$m, $R_{in} = 1.85\,\mu$m, $wg_w = 0.25\,\mu$m, $n_c = 3.46$, $n_s = 1.46$. Defect parameters with which high Q, high sensitivity and mode matching with the waveguide are obtained are as follows: $N_d = 80$, $r_1 = 0.03\,\mu$m, $r_2 = 0.048\,\mu$m, $d_1 = 0.0575\,\mu$m, $d_2 = 0.0575\,\mu$m. The coupling gap (the distance between the waveguide and the ring) was $0.2\,\mu$m. A grid step size of 10 nm was found to be sufficient for FDTD simulations for wavelengths close to $1.55\,\mu$m. At first glance, a grid step size of 10.0 nm would seem to be too large, but MEEP has a material averaging feature, which helps to maintain second-order accuracy at the material interface and allows one to use a larger step size [17]. The resonance wavelength and Q factor obtained with a 5 nm grid step size differed only by 0.05% and 1.64% from the ones obtained with a 10 nm grid step size. We also used FEM to check the results from FDTD close to $\lambda = 1.55\,\mu$m and the agreement was good. The mesh used in the FEM simulations is shown in figure 4(a).

The placement of the defects is crucial to the total internal reflection effect. As the defects get closer to either the inner or the outer edges of the microring, the average refractive index of the core at that edge gets smaller. This change in average refractive index induces a change of the critical angle for total internal reflection:

$$\theta_c = \arcsin(n_{low}/n_{high}) \tag{3}$$

where n_{high} is the average refractive index of the high dielectric constant material and n_{low} is the refractive index of the low dielectric constant material. It is apparent from equation 3 that decrease of n_{high} decreases the number of wavevectors experiencing the total internal reflection effect inside the perforated microring resonator. Thus, the modulation of the average refractive index allows us to pull the light towards and away from the resonator center and correspondingly change the light interaction with the surrounding medium. However, the defects should not touch the edges of the ring; otherwise, due to the loss of n_{high} near the edge of the ring resonator, the total internal reflection would be negligible and correspondingly strong scattering of the light and a decrease of Q would be inevitable.

We used FDTD to get drop port intensity versus wavelength data for our resonator structure. Excitation with a sinusoidal pulse having a Gaussian envelope in time at the bus waveguide was used to cover the wavelength window from $1.4\,\mu$m to $1.7\,\mu$m. The calculated normalized drop port intensity is shown in figure 3(a). The resonance peak corresponding to $\lambda = 1.547\,\mu$m has a Q value of about 800.

Two close peaks at $\lambda = 1.492\,\mu$m visible in figure 3(a) are the result of mode splitting. The inset in figure 3(a) shows drop and $drop_2$ port intensities at this wavelength. The peak in the $drop_2$ port intensity spectra occurs due to a counter-propagating mode. This counter-propagating mode can be the result of the discretization used in the simulation and/or the periodic nature of the structure. This effect is also observed in experiments with a microring resonator having no defects [18]. Its cause is surface roughness, which manifests itself in back scattering of the propagating field. In our case the back reflection is caused by the finite resolution of the rectangular grid used to describe the perforations. The simulation done with FEM reveals that there is no counter-propagating mode at this wavelength, because the device operates below the first-order Bragg bandgap.

To evaluate the bulk sensitivity of a resonator, the refractive index of the host material is slightly altered, on the assumption that we do not strongly disrupt the microring resonator. Here we altered n_s from 1.46 to 1.47. The shift of the drop port intensity peak is presented in figure 3(b).

The FDTD and FEM simulations showed the same resonance wavelength shift of approximately 2.4 nm when the refractive index of the host material was increased by 0.01. Equation 1 yields the sensitivity S of 240 nm/RIU. In comparison, an ordinary microring resonator with the same spatial parameters and no perforations has a sensitivity S of 80 nm/RIU. The increase in the sensitivity by a factor of three must be attributed to the perforations. Not only do the perforations increase the total surface area of the resonator to about triple, but also they increase the total electromagnetic field energy in a low dielectric constant material, which could be essential for applications in nonlinear optics. The field amplitude at the resonance wavelength of $\lambda = 1.547\,\mu$m is shown in figure 4(b).

Our simulations show that the Q factor of the perforated microring structure can be increased while keeping the same sensitivity in a couple of ways—for example, changing the coupling gap from $0.2\,\mu$m to $0.3\,\mu$m increases the Q factor to 3054 (figure 5(a)). However, further increase of the coupling gap results in a lower amplitude of electromagnetic radiation circulating inside the resonator and hence a smaller resonance

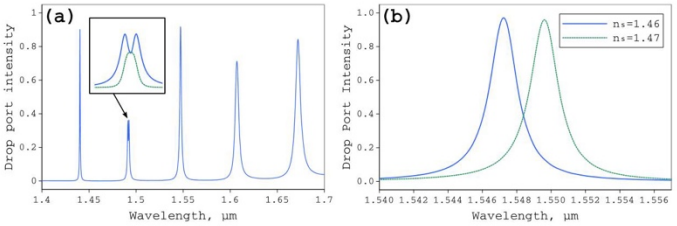

Figure 3. (a) Normalized drop port intensity. The inset shows an enlarged portion of the figure at the wavelength 1.492 μm. In this inset, the solid line represents the drop port intensity, and the dashed line represents the drop$_2$ port intensity. (b) Shift in drop port intensity peak as the refractive index of the host material is altered from 1.46 to 1.47.

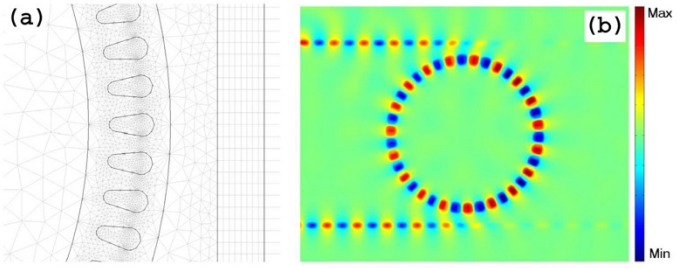

Figure 4. (a) Mesh used in FEM simulations. (b) Field distribution at $\lambda = 1.547\ \mu$m.

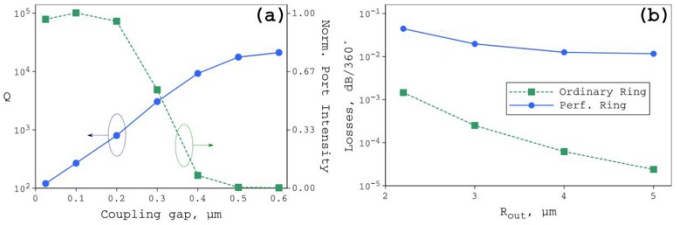

Figure 5. (a) Q factor and normalized drop port intensity versus coupling gap. (b) Radiation losses for various outer radii of the perforated microring resonator. For comparison, the same losses are plotted for an ordinary ring resonator with the same geometrical parameters.

peak in either the drop port or the transmission port intensity spectra, thus complicating detection of the signal in real world applications. From figure 5(a) we can see that with a coupling gap of 0.2 μm, the resonator is undercoupled. For critical coupling, the coupling gap should be reduced to 0.1 μm and at this distance the normalized transmission port intensity is close to 0 while the drop port intensity is almost 1.

Figure 5(b) presents radiation losses per round trip versus the radius of the microring resonator. To get these results we have calculated the time that it takes for a mode at $\lambda = 1.547\ \mu$m to travel one full circle around the resonator, and the Q factor of that mode. This allows us to calculate the loss per round trip. We kept the same density of perforations for all radii of the rings. A larger radius results in a smaller curvature of the ring. In turn this reduces the scattering from

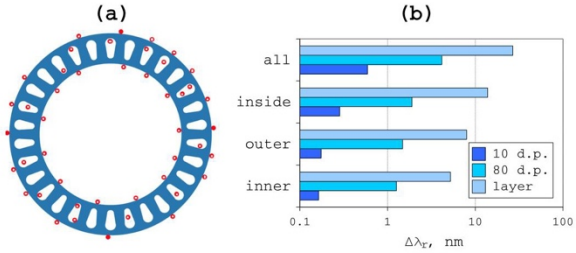

Figure 6. (a) Random distribution of the dielectric particles (red color) around and inside the perforated microring resonator. (b) The shift in the drop port intensity peak induced by 10, 80 and an infinite number (simulated as a layer) of dielectric particles covering the resonator when the dielectric particles are distributed: at the inner surface of the ring; at the outer surface of the ring; inside the defects; and on all surfaces.

side walls. The radiation loss per round trip saturates (minimum losses) at a radius of 5 μm. This indicates that the main factor causing losses is the scattering of light from the perforations.

To evaluate the shift of the drop port intensity peak (surface sensing) which would be induced by dielectric particles distributed on top of the resonator, we introduced random distributions of various numbers of dielectric cylinders of radius 30 nm with refractive index 1.5 near the surface of the resonator (figure 6(a)). For this, we also changed the host refractive index to 1.33 to mimic that of the water. Ten simulations with different random distributions of dielectric particles were run. The results presented are their averages. It can be noted that the exact position of the dielectric particle (provided that it is small and does not have a refractive index much higher than that of the surrounding media) is not as crucial as it is in, for example, the case of gold particles [19]. The resonance peak shift for various distributions and amounts of particles is presented in figure 6(b). With dielectric particles inside the defects, the resonance peak shift is twice that for setups where dielectric particles are distributed on either the inner or the outer surfaces of the resonator: 0.285 nm versus 0.164 nm and 0.175 nm for 10 particles. When dielectric particles are distributed all over, the resonator shift of 0.592 nm results. This is almost the sum (the sum would be 0.623 nm) of the three previous cases. This result can be explained via the wavelength shift prediction based on a model from coupled mode theory [18]:

$$\Delta\lambda = \Delta n_{\mathrm{eff}}\, \lambda_{\mathrm{r}}/n_{\mathrm{g}} \tag{4}$$

where Δn_{eff} is the change in effective mode index caused by the change in surrounding media refractive index and n_{g} is the group index. The effective index of the propagating mode depends strongly on the refractive index of the surrounding material. When there is more material with higher refractive index (as in the case where a layer/particles are distributed all over the resonator), the change in effective index is larger. And so is the change in resonance wavelength.

As the number of particles increases approaching the state of a homogeneous dielectric layer, the shift approaches the value of 26.748 nm. Our calculations here show that even a small number of dielectric particles at the resonator surface have an observable effect on the drop port intensity spectrum shift, showing that inner defects (which can be customized for the different particles) allow us to increase the sensitivity by increasing the total area of interface between the microring resonator and the surrounding medium.

We have also simulated our resonator in 3D to see how its performance changes when radiation losses along the direction perpendicular to the structure are introduced. Using same parameters as in the 2D calculations we obtained a sensitivity of 432 nm/RIU and a Q value of 370 at the resonance wavelength $\lambda = 1.52$ μm. Increasing the outer radius of the resonator from 2.2 μm to 3 μm and the number of defects from 80 to 118 resulted in a lower sensitivity (332 nm/RIU) and a higher Q value (700).

4. Conclusions

A novel microring resonator structure with low dielectric constant material defects has been proposed for refractive index sensing applications. Its performance in bulk and surface sensing schemes has been analyzed. We showed that our proposed refractive index sensor based on a microring resonator outperforms ordinary microring resonators. The perforated microring resonator presented allows variation of the quality factor and the sensitivity, making it applicable in many optical areas. Our design not only achieves high sensitivity, but also increases the total area of the interface between the microring resonator and the surrounding medium, which can increase the light–matter interaction with aqueous media and gases.

Acknowledgments

This research was funded by a grant VP1–3.1-SMM-10-V-02–026 from the European Social Fund Agency in Lithuania.

References

[1] Narayanaswamy R and Wolfbeis O S 2004 *Optical Sensors* (New York: Springer)
[2] Luchansky M S and Bailey R C 2012 *Anal. Chem.* **84** 793–821
[3] Fan X, White I M, Shopova S I, Zhu H, Suter J D and Sun Y 2008 *Analytica Chimica Acta* **620** 8
[4] Barrios C A 2012 *Anal. Bioanal. Chem.* **403** 1467–75
[5] Chao C Y and Guo L J 2006 *Lightwave Technol.* **24** 1395–402
[6] Claes T, Bogaerts W and Bienstman P 2011 *Opt. Lett.* **36** 3320–2
[7] Jin L, Li M and He J J 2011 *Opt. Commun* **284** 156–9
[8] Gaathon O, Culic-Viskota J, Mihnev M, Teraoka I and Arnold S 2006 *Appl. Phys. Lett.* **89** 223901
[9] Hiremath K R, Niegemann J and Busch K 2011 *Opt. Express* **19** 8641–55
[10] Barrios C A, Gylfason K B, Sanchez B, Griol A, Sohlstrom H, Holgado M and Casquel R 2007 *Opt. Lett.* **32** 3080–2
[11] Barrios C A, Banuls M J, Gonzalez-Pedro V, Gylfason K B, Sanchez B, Griol A, Maquieira A, Sohlstrom H, Holgado H and Casquel R 2008 *Opt. Lett.* **33** 708–10
[12] Claes T, Molera J G, de Vos K, Schacht E, Baets R and Bienstman P 2009 *IEEE Photon. J.* **1** 197–204
[13] Khorasaninejad M, Clarke N, Anantram M P and Saini S S 2011 *Opt. Express* **19** 17575
[14] Gabrielli L H, Liu D, Johnson S G and Lipson M 2012 *Nat. Commun.* **3** 1217
[15] Oskooi A F, Roundy D, Ibanescu M, Bermel P, Joannopoulos J D and Johnson S G 2010 *Comp. Phys, Commun.* **181** 687–702
[16] Chremmos I, Schwelb O and Uzunoglu N 2010 *Photonic Microresonator Research and Applications* (New York: Springer)
[17] Oskooi A F, Kottke C and Johnson S G 2009 *Opt. Lett.* **34** 2778–80
[18] Bogaerts W, de Heyn P, van Vaerenbergh T, de Vos K, Kumar Selvaraja S, Claes T, Dumon P, Bienstman P, van Thourhout D and Baets R 2012 *Laser Photon. Rev.* **6** 47–73
[19] Haddadpour A and Yi Y 2010 Biomed *Opt. Express* **1** 378–84

DOI: 10.1364/OL.40.002977
© The Optical Society. Reproduced with permission. All rights reserved

Optics Letters

Ultra-wide free spectral range, enhanced sensitivity, and removed mode splitting SOI optical ring resonator with dispersive metal nanodisks

DARIUS URBONAS,[1,*] ARMANDAS BALČYTIS,[1,2] MARTYNAS GABALIS,[1] KONSTANTINAS VAŠKEVIČIUS,[1] GRETA NAUJOKAITĖ,[1] SAULIUS JUODKAZIS,[2] AND RAIMONDAS PETRUŠKEVIČIUS[1]

[1]Center for Physical Sciences and Technology, Savanorių Ave. 231, LT-02300 Vilnius, Lithuania
[2]Swinburne University of Technology Centre for Micro-Photonics, Hawthorn, Victoria, 3122, Australia
*Corresponding author: darius.urbonas.p@gmail.com

Received 20 April 2015; accepted 29 May 2015; posted 4 June 2015 (Doc. ID 238488); published 18 June 2015

A refractive index sensor with a free spectral range that is unlimited by neighboring mode spacing (10 fold increase with respect to 20 nm of an unmodified ring), based on an optical silicon-on-insulator microring resonator patterned with periodically arranged set of gold nanodisks, is presented and numerically verified. It is shown that the particular periodic arrangement of nanodisks selects a single resonance from a wide set of ring resonator modes and removes mode splitting. Extraction of the waveguided electromagnetic energy into evanescent plasmonic modes enhances light–analyte interaction and increases device sensitivity to variation of refractive index up to 176 nm/RIU (about 2-fold increase compared to the unmodified ring), which is useful for sensor applications. Proof of the concept is presented by finite-difference time-domain simulations of a design readily practicable by means of modern nanotechnology. © 2015 Optical Society of America

OCIS codes: (230.5750) Resonators; (130.0130) Integrated optics; (130.7408) Wavelength filtering devices; (130.6010) Sensors; (250.5403) Plasmonics.

http://dx.doi.org/10.1364/OL.40.002977

Optical microring resonators have become a topic of great interest for devising wavelength selective filters [1], low-threshold semiconductor lasers [2,3], and especially for sensing applications in early-stage disease diagnosis, security, and environmental monitoring [1,4,5], where high-sensitivity label-free sensors based on optical resonators are among the most promising in the field [6].

As established previously [1,4,5,7], optical ring resonators have numerous advantages such as a high quality factor (Q) and a narrow resonance line width, which allows detection of small spectral resonance shifts due to minute changes of refractive index induced by trace amounts of analytes. However, if an induced resonance shift is large enough to overlap with a neighboring resonant mode position, the refractive index variation driven line-shift can no longer be unambiguously determined. In other words, when a resonance shift exceeds the free spectral range (FSR), sensor performance is compromised. This critically limits the applicability of very narrow FSR resonances such as in optical microring resonators, in which large spectral shifts cannot be reliably determined.

How could an optical microring resonator be modified so that it would have a neighboring mode spacing unlimited FSR? Here, it is achieved by engineering waveguide dispersion using metal nanodisks (MNDs) periodically arranged on top of a silicon-on-insulator (SOI) optical ring resonator thereby creating a second-order $m = 2$ Bragg grating:

$$m\lambda_R = 2n_{\text{eff}}\Lambda, \tag{1}$$

where Λ is the period of MNDs, and n_{eff} is the complex effective refractive index of a particular mode at Bragg resonance wavelength λ_R. Interference between light coupled into the ring resonator and the Bragg-reflected waves results in suppression of most of the resonances that would be otherwise supported by an unmodified microring.

To show the proof of concept, 3D finite-difference time-domain (FDTD) simulations for TE polarization were performed. The simulated test structure, sketched in Fig. 1, is a SOI optical ring resonator with 4.2-μm outer and 3.8-μm inner radii and a height of 0.22 μm. The bus waveguide is 0.22 μm high and 0.45 μm wide. The distance between the optical ring resonator and the bus waveguide is 0.13 μm. An array of equally spaced gold nanodisks that are 30 nm high and have 87 nm radii is added on top of the ring. The ring resonator was considered to be operating in a dielectric environment with a refractive index n_{env} of 1.33, corresponding to water.

Numerical investigation of modal properties and sensor performance was conducted by first simulating a fully dielectric

0146-9592/15/132977-04$15/0$15.00 © 2015 Optical Society of America

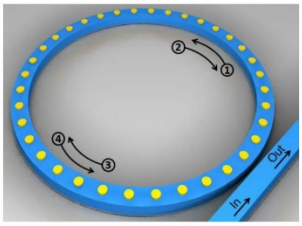

Fig. 1. Visualization of SOI optical-ring resonator with implemented gold nanodisks. Directions 1 and 3 are launched wave, while 2 and 4 are counter-propagating waves (see text for details).

reference SOI microring with shallow 2nd-order Bragg grating on the inner surface [8] without the MND array.

Light is coupled into the SOI optical ring resonator via a bus waveguide (port IN in Fig. 1), and transmission spectra are measured at the OUT port. A typical transmission spectrum is shown in Fig. 2. The structure supports multiple ring resonator modes at which resonant transmission dips occur. It is evident that resonant mode close to 1.575 μm is split into two (blue curve). This occurs due to a band-gap induced by the Bragg grating and is related to the appearance of even and odd standing-wave modes (E and O modes on Fig. 2) as a symmetric and antisymmetric superposition of the counterpropagating traveling waves [9]. Addition of the gold MND array leads to formation of a single resonance dip, which coincides with the O-mode resonance peak of the unmodified ring. The O-mode survives due to having its intensity peaks localized between the MNDs and the resulting low overlap with the metal disks. Conversely, the E-mode is strongly suppressed due to the introduction of MNDs because its intensity peaks are localized directly underneath them. Other resonances that are supported by an unmodified resonator also dissipate while propagating through the microring due to scattering losses as observed for dielectric microgear and microflower disk resonators [10–12]. In the case of a MND decorated microring, this dissipation effect is further enhanced by excitation of surface plasmons and the resulting dissipation in the metal. In other words the device operates as a perfect filter—only a single-ring-resonator mode, which matches the MND introduced second-order Bragg condition [10,12] (Eq. 1), (O-mode) is preserved, and mode splitting is removed.

Position of the resonant peak depends on both the number of gold nanodisks (period of arrangement) and the overall perimeter of the ring resonator. In Fig. 3, shifts of the solitary resonance peak with respect to the number of nanodisks (period) are illustrated. From Eq. (1), the real part of the n_{eff} for the resonant mode can be determined, which is shown to monotonically blue-shift and become narrower for a larger number of MNDs (the circumference of the ring resonator is kept fixed for all simulations). This blue-shift is the result of the 2nd-order Bragg grating period change, which in turn influences the phase matching conditions.

The electric-field-intensity distribution of a particular resonant mode in a simulated optical ring resonator is shown in Fig. 4(a). It is evident that this mode is supported by the modified ring resonator, whereas off resonance (+10 nm), it is strongly suppressed [Fig. 4(b)] and is unable to offset the damping due to excitation of localized plasmonic mode [13].

Light coupled into the ring [arrow 1 in Figs. 1 and 4(b)] gets scattered due to interaction with the periodic MND array and gives rise to a counter-propagating wave (CPW) (arrow 2). Some of this reflected light is decoupled out of the ring back into to the bus waveguide and propagates toward the IN port. The remainder of the reflected electromagnetic radiation propagates counter-clockwise (arrow 3), generating further reflections (arrow 4) along the way, which in turn can be decoupled back in to the bus waveguide as well as scattered out of the device plane by MNDs. As the cycle is repeated, the waveguided reflections interfere with the originally launched wave. If this interference is constructive, a resonant stationary O-mode with a periodic pattern of electric field intensity maxima localized between the MNDs is established.

In principle, the approach presented here would also work with a first-order $m = 1$ Bragg grating. The only difference is that a first-order Bragg grating creates a CPW only, whereas the second-order Bragg grating creates CPWs and also scatters the light in a perpendicular out-of-plane fashion. However, a gold nanodisk-derived first-order Bragg grating configuration is less efficient at single-frequency filtering due to proximity-driven coupling between neighboring MNDs giving rise to a propagating plasmonic mode [14,15].

The size of the nanodisks is another key factor in determining the single-resonant frequency of the device. Simulation results presented in Fig. 5 indicate that when gold nanodisks have

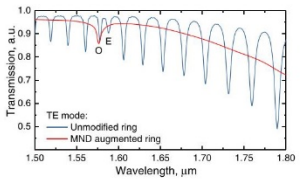

Fig. 2. Transmission spectra of unmodified and Au MND-augmented SOI optical ring resonators at OUT port for TE polarization.

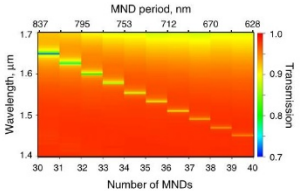

Fig. 3. Dependence of the resonant frequency on the number (period) of gold nanodisks. Color represents transmission intensity.

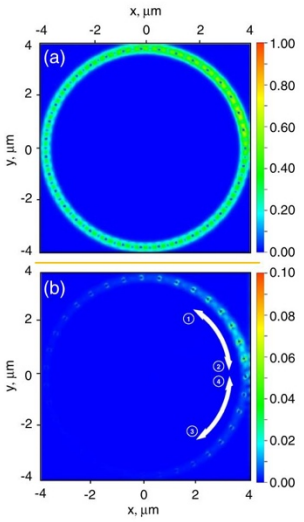

Fig. 4. (a) TE intensity at resonant frequency (35 gold nanodisks). (b) TE intensity +10 nm off-resonant wavelength. The arrows 1 and 3 denote launched waves, and arrows 2 and 4 represent counter-propagating waves (see text for details). The field profiles were taken in the XY plane at half height of gold nanodisks. Color represents intensity. The bus waveguide is vertical (light propagates along y-axis) and is at the right-side of the maps.

a 40 nm radius the device still works as an ordinary ring resonator; however, when the radii exceed ~70 nm, all other resonances become suppressed. This size-dependent effect is caused by the frequency shift of localized plasmonic modes supported by MNDs (which are recognizable around the edges of

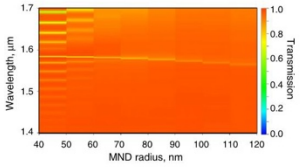

Fig. 5. Dependence of the resonant frequencies and the appearance of ultra-wide FSR operation regime in an MND-decorated microring resonator as the gold nanodisk radii are increased (35 gold nanoparticles). Color represents transmission intensity.

the disks in Fig. 4). An instructive, although simplified, way of considering this plasmonic contribution is to describe it as a decrease of the real and an increase of the imaginary parts of the effective refractive index as the plasmonic resonance is shifted by changing MND geometry [16].

Capability for the proposed device to operate even at extremely variable sensing environments was tested by simulating resonance shift with respect to the change of refractive index of the surrounding medium (bulk sensitivity). When refractive index is altered from $n_{env} = 1$ to $n_{env} = 2.6$, the corresponding device transmission spectra are shown in Fig. 6(a). The FSR of the resonant mode is proven to be terminated only by the bandwidth of the waveguide (mode cut-off). The total FSR of the proposed device is roughly ~200 nm, whereas for the corresponding unmodified microring with the same parameters, the FSR is only ~20 nm. Furthermore, the MND-augmented ring resonator does not sacrifice sensitivity. As shown in Fig. 6(b), at moderate refractive index changes $n_{env} = 1.33 \pm 0.01$, typical for sensing waterborne analytes, resonator response shows excellent linearity. The simulated sensitivity of the proposed ring resonator device was found to be around 110 nm/RIU. At higher refractive indices in Fig. 6(c), $n_{env} = 2.32 \pm 0.01$, the sensitivity is 242 nm/RIU due to the mode approaching the cut-off and delocalization of the mode field extending to external medium. The ultra-wide FSR average sensitivity is about 176 nm/RIU, which is a substantial increase (about 2 fold) over the value of ~70 nm/RIU for an unmodified microring resonator. This sensitivity enhancement is attributed to the extraction of the electromagnetic energy from confinement in the high-index SOI waveguide into evanescent plasmonic modes supported by the nanodisks, where it can interact with the analytes more strongly.

The simulated quality factor of a resonance at 1.577 μm was at $Q \approx 500$ for the unmodified microring, and decreases to $Q \approx 300$ after the addition of MNDs. However, even this

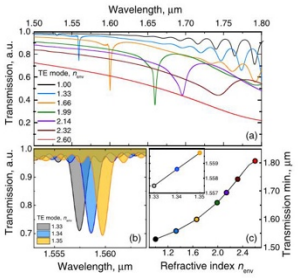

Fig. 6. (a) The resonant mode shift due to large changes in refractive index of the surrounding medium (ring decorated with 35 gold nanoparticles). (b) Resonant transmission dip shifts due to moderate $n_{env} = 1.33 \pm 0.01$ refractive-index modifications of the surrounding environment, typical when sensing water-soluble analytes. (c) Spectral position dependence of the resonant transmission dip on the refractive index of the surrounding medium extracted from panel (a). Inset displays an analogous sensitivity plot for panel (b).

DOI: 10.1364/OL.41.003655
© The Optical Society. Reproduced with permission. All rights reserved

Optics Letters

Air and dielectric bands photonic crystal microringresonator for refractive index sensing

Darius Urbonas,[1] Armandas Balčytis,[1,2] Konstantinas Vaškevičius,[1] Martynas Gabalis,[1,*] and Raimondas Petruškevičius[1]

[1]Center for Physical Sciences and Technology, Savanoriu Ave. 231, LT-02300 Vilnius, Lithuania
[2]Centre for Micro-Photonics, School of Science, Swinburne University of Technology, John St., Hawthorn, VIC 3122, Australia
*Corresponding author: martynas.gabalis@ftmc.lt

Received 17 May 2016; revised 11 July 2016; accepted 13 July 2016; posted 18 July 2016 (Doc. ID 264743); published 1 August 2016

We present the experimental and numerical analysis of a microring resonator with an integrated one-dimensional photonic crystal fabricated on a silicon-on-insulator platform and show its applicability in bulk refractive index sensing. The photonic crystal is formed by periodically patterned, partially etched cylindrical perforations, whose induced photonic bandgap is narrower than the range of measurable wavelengths (1520–1620 nm). Of particular interest is that the microring operates in both air and dielectric bands, and the sensitivities of the resonances on both edges of the bandgap were investigated. We showed that a higher field localization inside the volume of the perforations for the air band mode leads to an increase in sensitivity. © 2016 Optical Society of America

OCIS codes: (130.3120) Integrated optics devices; (050.5298) Photonic crystals; (130.6010) Sensors; (260.2030) Dispersion.

http://dx.doi.org/10.1364/OL.41.003655

Microring resonators due to their small size and high achievable quality factor have become an attractive platform in many different types of applications, such as sensing, delay lines, nonlinear optics, etc. [1]. The silicon-on-insulator (SOI) platform, due to the high refractive index of silicon (Si), enables the fabrication of waveguides with extremely small bending radii [2], resulting in the possibility of making exceptionally small microring resonators. But the high mode field confinement inside the Si waveguide puts SOI devices at a disadvantage in applications where mode field interaction with the environmental medium is of critical importance.

As a way of increasing the volume of interaction between the microring resonator mode field and the environmental medium it was suggested to introduce a one-dimensional photonic crystal inside the ring waveguide [3,4]. The resulting reduction in Si volume and mode field confinement may lead to a lower quality factor (Q-factor) of the resonances. However, as it was shown by Soljačić *et al.* [5] and later by Goldring *et. al.* [6], introducing high dispersion inside the cavity material via photonic crystal may lead to a dramatic increase in Q-factor of the cavity resonance. For wavelengths close to the edge of the photonic bandgap group velocity approaches zero and spectral narrowing of resonance lines occurs.

The photonic bands above and below the photonic bandgap can be distinguished by where the energy of their modes is concentrated: in the low or high refractive index (RI) regions. Correspondingly, the modes on the respective sides of the bandgap are usually denoted as air band (higher frequency) and dielectric band (lower frequency) [7].

Recently the applicability of microring resonators with integrated one-dimensional photonic crystals (*MRR-PhCs*) was shown in applications such as localized strain sensing [8], optical filtering [9], narrow-band mirror [10], lasers [11], and optical vortex generation [12].

In this Letter, we present a SOI *MRR-PhC* applied in bulk refractive index sensing. The operation of the previously reported *MRR-PhC* was limited exclusively to the dielectric or air band [3,13,14]. The novelty of our design is that it operates in both bands and we can simultaneously measure sensitivities of resonance modes on both edges of the bandgap. We show that due to higher field localization inside the perforations, sensitivity of the air band mode to variations in surrounding RI is higher than for the dielectric band mode.

While the results presented in this Letter are for bulk refractive index sensing, in which the extension of analyte material is larger than the extension of the guided-mode evanescent field, the device could potentially be used in other applications. Different sensitivities of air and dielectric band modes could be employed in surface sensing to simultaneously monitor surface layer thickness and refractive index, or simultaneous bulk refractive index and temperature measurements, where previously dual-polarization (TE and TM) ring resonators were used in order to associate two unknown quantities with two measurement results (resonance line shifts for TE and TM polarizations) [15,16]. Thus eliminating the need for dual-polarization excitation and discrimination between TE and TM resonance lines in the measured transmission spectra.

Another attractive feature of the presented sensor is that the photonic bandgap could provide a reference point for sensing refractive index changes whose induced resonance wavelength shift exceeded spectral spacing between resonances [17], as it

0146-9592/16/153655-04 Journal © 2016 Optical Society of America

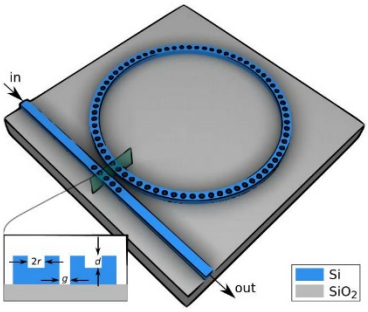

Fig. 1. Geometry of the microring resonator with an integrated photonic crystal (*MRR-PhC*). Inset shows cross section of the evanescent coupling region. In the inset r denotes hole radius; d, hole depth; and g, coupling gap.

helps to identify and follow MRR-PhC resonance modes during sensor operation.

The geometry of the *MRR-PhC* under investigation is shown in Fig. 1. Five holes of the same size and periodicity as the holes forming the one-dimensional photonic crystal inside the microring were added to the bus waveguide to ensure good evanescent coupling between the bus waveguide and the microring resonator. The scanning electron microscopy image of a lithographically fabricated representative *MRR-PhC* is shown in Fig. 2. The geometrical parameters of the microring resonator structure are summarized in Table 1.

The one-dimensional photonic crystal was integrated onto a 4000 nm radius microring resonator structure constructed of a waveguide with width and height of 400 nm and 240 nm, respectively. The one-dimensional photonic crystal was formed by periodically placing cylindrical perforations. Our device was

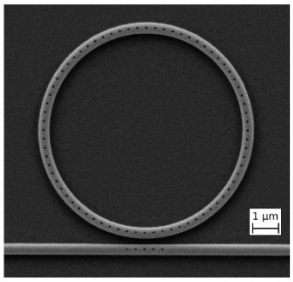

Fig. 2. Scanning electron microscopy image of a fabricated *MRR-PhC*.

Table 1. Geometrical Parameters of MRR-PhC

Parameter	Numerical Value
Middle radius	4000 nm
Ring waveguide width	400 nm
Hole radius (r)	70 nm
Hole depth (d)	70 nm
Number of holes	72
Hole periodicity (Λ)	350 nm
Bus waveguide width	400 nm
Coupling gap (g)	180 nm
Silicon thickness	240 nm

fabricated at ePIXfab (*imec*, Leuven) using a standard complementary metal oxide semiconductor process [18], with the possibility of having three silicon etch depth levels: 240, 150, or 70 nm. Our characterization setup allowed us to measure transmission spectra in the wavelength window ranging from 1520 to 1620 nm. Therefore, the photonic crystal design was chosen so that it would form a photonic bandgap bounded within this wavelength region. Thereby the number of cylinders was fixed to 72, resulting in the period $\Lambda = 350$ nm, for which the first-order Bragg wavelength is equal to 1550 nm.

Numerical simulations were conducted using a free finite-difference time-domain Maxwell's equation solver software package Meep [19]. Meep was used for both whole structure and photonic band structure simulations. For band structure simulations we used a transformation optics approach to convert a single-period segment of the microring from a bended to straight one by correspondingly altering the material properties [20]. To increase the accuracy of numerical simulations subpixel smoothing, available in Meep [21], was used for full ring simulations (10 nm grid step size). In all simulations and experimental measurements TE-polarized light (electric field parallel to the device plane) was used.

Simulation results for bandgap width as a function of hole radius at various hole depth values are presented in Fig. 3. As the air fraction introduced by the holes increases, so does the photonic bandgap width. However, the decrease in the bandgap width visible in Fig. 3 for hole radius values in excess of 120 nm

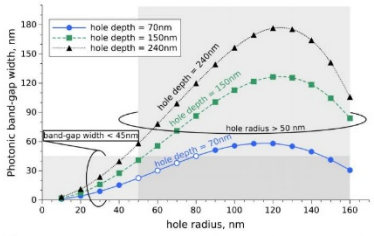

Fig. 3. Photonic bandgap width as a function of the hole radius for three hole depth values: 70, 150, and 240 nm. Gray area represents limitations imposed by fabrication process and measurement setup. Hole radius must exceed 50 nm and bandgap width must be thinner than 45 nm. Intersection of two areas are the available designs: hole depth of 70 nm and hole radius in the range 50–80 nm.

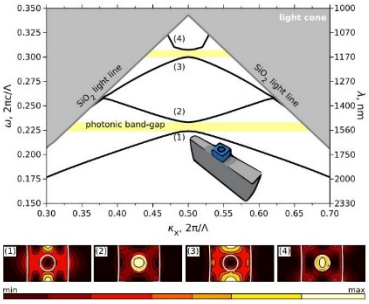

Fig. 4. Band diagram of holey bend waveguide. (1) and (3) denote dielectric bands, (2) and (4) denote air bands. The bottom panels show the distribution of electric field energy density of all four bands at $\kappa_x = 0.49$.

is a result of the structure geometry approaching that of a conventional waveguide, but with a smaller waveguide height. The experimentally attainable range of wavelengths for our characterization setup is 100 nm. In order to have at least one resonance on one side of the photonic bandgap and several on the other side we limited the maximum width of the photonic bandgap to 45 nm or less. Therefore, for a hole depth of 70 nm the range of hole radii is <80 nm. When the hole depth is 150 nm their radius should be <50 nm, and for 240 nm depth it should be <45 nm. However, a small hole radius can result in poor sensor performance due to the analyte's inability to expel the air trapped within and fill them [22]. Therefore an optimal hole radius of 70 nm at a hole depth of 70 nm was chosen. For theoretical analysis and custom fabrication conditions different values could be considered, with shallower holes making analyte accommodation easier, however, at the cost of to some extent losing the benefit from reduced mode field confinement.

The simulated band diagram of the photonic crystal inside the microring resonator is presented in Fig. 4. The bandgap extends from roughly 1520 to 1560 nm. An additional bandgap is also established in the wavelength region from 1110 to 1120 nm. The electric field energy density distributions of each mode presented in the mode diagram are also shown in Fig. 4. It is evident that energy of the air band is mostly confined inside the hole region [region (2) in Fig. 4], in stark contrast to the dielectric band modes mostly confined in Si [region (1) in Fig. 4]. The fraction of mode energy inside the environmental medium for the air band mode is 0.110, whereas for the dielectric band mode it is 0.104. However, as we move away from the bandgap edge, from slow-light to traveling wave regime, the mode having larger wavelength (lower frequency) becomes less confined and more sensitive to environmental changes.

Transmission spectra of the microring resonator were measured by exposing the device to four different environmental materials: methanol (RI 1.3174), ethanol (RI 1.3522), isopropanol (RI 1.3661), and glycerol (RI 1.4571). Refractive index values at the free-space wavelength of 1550 nm are taken from [23]. Silicon RI used in simulation was 3.476 [24], whereas the RI of the underlying SiO_2 was assumed to be 1.444 [25]. The measurements are carried out on a temperature stabilized setup similar to [26] excited with TE polarization using vertical fiber grating couplers. Measurements for air environment were not included since the coupling gap (Fig. 1) was specifically chosen for environment with refractive index 1.3 or higher, thus resulting in low coupling efficiency and low extinction ratio in air environment.

The two quantities of interest in bulk refractive index sensing applications are sensitivity (S) and Q-factor. The sensitivity is a measure of resonance dip position change ($\Delta\lambda_{res}$) induced by refractive index change in the environmental medium (Δn_{env}) and can be expressed as [27] $S = \Delta\lambda_{res}/\Delta n_{env}$, while for high Q cavities the Q-factor can be expressed as the ratio between resonance wavelength and its linewidth: $Q = \lambda_{res}/\Delta\lambda_{fwhm}$.

The numerical simulations of the full microring structure with different environmental materials showed that the expected sensitivity of the dielectric band mode closest to the bandgap edge is 94.9 nm/RIU, and the sensitivity of the air band mode closest to the bandgap edge is 99.7 nm/RIU, 5.2 nm/RIU higher than that of the dielectric band mode. It is also worth mentioning that bulk refractive index sensitivity generally increases with longer wavelengths, and here the effect of mode field localization inside the holes overcomes this effect. Measured transmission spectra of the device are shown in Fig. 5. A bandgap approximately 35 nm in width is clearly visible in the transmission spectra, replicating that of the numerical simulations in both its width and position with good accuracy.

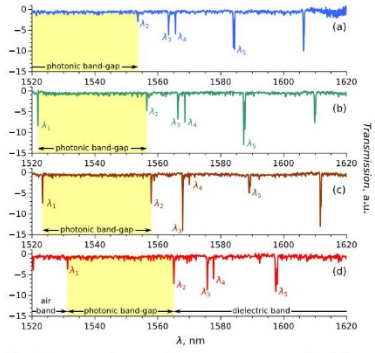

Fig. 5. Measured *MRR-PhC* transmission spectra for different environmental mediums: (a) methanol, $n_{env} = 1.3174$; (b) ethanol, $n_{env} = 1.3522$; (c) isopropanol, $n_{env} = 1.3661$; (d) glycerol, $n_{env} = 1.4571$. The photonic crystal induced bandgap extends from λ_1 to λ_2. λ_1 is the resonance in the air band; λ_2, λ_3, λ_4, and λ_5 are resonances in the dielectric band.

DOI: 10.1364/JOSAB.34.000750
© The Optical Society. Reproduced with permission. All rights reserved

Journal of the Optical Society of America B
OPTICAL PHYSICS

Enhanced sensitivity and measurement range SOI microring resonator with integrated one-dimensional photonic crystal

KONSTANTINAS VAŠKEVIČIUS,[1,*] MARTYNAS GABALIS,[1] DARIUS URBONAS,[1] ARMANDAS BALČYTIS,[1,2] RAIMONDAS PETRUŠKEVIČIUS,[1] AND SAULIUS JUODKAZIS[2]

[1]Center for Physical Sciences and Technology, Savanoriu Ave. 231, LT-02300 Vilnius, Lithuania
[2]Centre for Micro-Photonics, School of Science, Swinburne University of Technology, John St., Hawthorn, Victoria 3122, Australia
*Corresponding author: konstantinas.vaskevicius@ftmc.lt

Received 3 November 2016; revised 3 January 2017; accepted 24 January 2017; posted 26 January 2017 (Doc. ID 280096); published 8 March 2017

We present a silicon-on-insulator microring resonator-based refractive index sensor with enhanced sensitivity and measurement range. Both improvements are achieved by integrating a 1D photonic crystal inside the microring waveguide. A photonic crystal is formed by periodically patterning, partially etching the rectangular perforations. Sensor performance is numerically analyzed for various combinations of perforation depth and length, each of which maintains a constant resonance wavelength. Our findings show that, while deeper perforations result in a larger bulk refractive index sensitivity, the optimal design exhibiting the smallest limit of detection can be obtained at some intermediate value, depending on the leading term in sensor resolution. In addition to theoretical analysis, we present an experimental demonstration of a fabricated microring resonator with 120 nm height perforations. © 2017 Optical Society of America

OCIS codes: (130.0130) Integrated optics; (130.6010) Sensors; (140.4780) Optical resonators; (230.5298) Photonic crystals.

https://doi.org/10.1364/JOSAB.34.000750

1. INTRODUCTION

Microring resonators recently emerged as a promising platform for various applications. Numerous photonic devices based on microring resonators, e.g., [1] filters [2], switches [3], modulators [4], and sensors [5,6], have been demonstrated. In sensing applications, microring resonators are attractive due to their small size and high quality factor. A silicon-on-insulator (SOI) platform is among the most popular technologies for microring resonators. An SOI is attractive due to its compatibility with the well-established complementary metal oxide semiconductor (CMOS) process as well as high refractive index contrast that enables strong mode field confinement and small waveguide bending radius (down to 1.5 μm for microring resonator [7]).

The simplest microring resonator consists of a bus waveguide and ring structure (all pass resonator [8]); see Fig. 1. The optical field from a bus waveguide through the evanescent tail couples into the microring. The wave, after propagating a full round trip and gaining some phase, couples back to the bus waveguide and interferes with the transmitted wave. At resonance, the phase gain is such that the waves destructively interfere [9].

Sensory properties of such resonators emerge from mode field interaction with the surrounding medium. The change in refractive index of a surrounding medium induces change in the propagation constant of the particular mode, which then causes the change in resonance conditions. This effect can be observed by monitoring the shift in the resonance wavelength position ($\Delta\lambda_{res}$) [10].

Despite its conduciveness to miniaturization, the high mode field confinement exhibited by SOI resonators produces a disadvantage in sensing applications due to the small overlap between cladding material and mode evanescent field. In the case of microring resonators, several strategies have been proposed to overcome this: ultra-thin SOI microring resonator [11], introduction of a photonic crystal inside the microring resonator [12–15], slotted waveguide microring resonator [16,17], and a microring resonator with periodically arranged metal nanodisks [18,19].

Another problem arising from high refractive index contrast, especially for relatively large radius microring resonators, is the free spectral range (FSR, spectral spacing between nearby resonances), which imposes a limit on the measurable extent of variations in analyte concentration ($\Delta\lambda_{res} < FSR$). A resonance wavelength shift that exceeds the FSR becomes indistinguishable from a nearby resonance. Hence, to increase the measurement range it has been suggested to employ nearby mode

0740-3224/17/040750-06 Journal © 2017 Optical Society of America

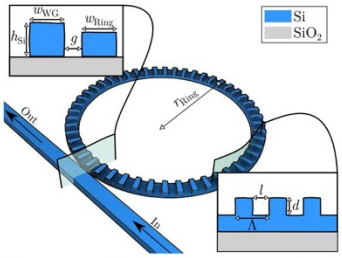

Fig. 1. Geometry of the perforated microring resonator. h_{Si}, silicon thickness; w_{WG}, bus waveguide width; w_{Ring}, ring waveguide width; g, coupling gap; r_{Ring}, ring radius; d, perforation depth; l, perforation length; Λ, period.

suppression [18,20] and to use microring resonators with embedded asymmetric Mach–Zehnder interferometers [21].

In this paper we present a microring resonator designed specifically to enhance sensitivity and increase the measurement range. Both improvements are achieved via integration of a 1D photonic crystal inside the microring waveguide. The photonic crystal is formed by periodically patterned, partially etched rectangular perforations. It is designed to induce a photonic bandgap with an edge at the lower part of the measurable wavelength window (1520–1630 nm in our measurement setup). Thus, the position of the photonic bandgap can be used as a reference point during sensor operation, eliminating the limitation imposed by FSR.

We limit our analysis in this work to bulk (or volume/homogeneous) refractive index sensitivity. In this sensing scheme, the volume of analyte material extends far beyond the range of the mode evanescent field. And, while the bulk refractive index sensitivity has been shown to increase with longer perforations (or smaller duty cycle) [22], the effect of perforation depth on the interaction between mode evanescent field and surrounding medium, to the best of our knowledge, has not been previously analyzed. We note that the proposed structure could also be used in a surface sensing scheme, where effective mode index change is induced by the dielectric layer of thickness, which is comparable with that of evanescent field. While single mode operation provides a limited amount of information (thickness if the refractive index is known, or converse), several strategies have been proposed to measure both surface layer thickness and its refractive index [15,23,24]

The possibility to fabricate waveguides with different perforation depths opens a new degree of freedom in device design. It was previously utilized in devising polarization splitters–rotators [25] and grating couplers [26]. We conduct numerical simulations of microring resonators with 1D photonic crystals resulting from varying perforation depths to analyze how sensors characteristics are affected. We show that deeper perforations result in higher bulk refractive index sensitivity. However, another important characteristic of a sensor, limit of detection, can obtain its minimum at some intermediate value, dependant on which mechanism dominates the sensor resolution.

In addition to theoretical analysis, we also present measurement results of a fabricated SOI microring resonator sensor in which a photonic crystal is formed by 120 nm depth rectangular perforations.

2. STRUCTURE DESIGN

The general structure of the analyzed SOI microring resonator is shown in Fig. 1. The photonic crystal inside the microring resonator is formed by periodically patterned, partially etched rectangular perforations. The depth of the perforations is denoted by d and their length by l. In all simulations, we assumed the microring radius (r_{Ring}) to be 5100 nm, microring waveguide width (w_{Ring}) is 410 nm, bus waveguide width (w_{WG}) is 380 nm, coupling gap (g) is 120 nm, and total height of silicon (h_{Si}) is 240 nm. The chosen coupling gap ensures microring resonator operation close to critical coupling [1,13]. All parameters are well within the limits of fabrication requirements. The number of perforations was chosen to be 80, which results in a period of 400 nm. A silicon refractive index (RI) used in simulation was 3.4757 [27], SiO_2 RI was 1.4440 [28]. Excitation polarization in both theoretical model and manufactured structure is TE.

Numerical simulations of a full microring structure were conducted using a fully 3D finite-difference time-domain (3D FDTD) method implemented in a noncommercial software package Meep [29]. Band diagram calculations on a one period segment of a photonic crystal was modeled using a fully vectorial, open-access, eigenmode solver MPB [30]. The grid step size used in 3D FDTD simulations was 20 nm, and in-band diagram calculations were 10 nm. Also, to increase accuracy of numerical simulations, subpixel smoothing [31] was used.

Three quantities of interest in sensing applications were measured: bulk refractive index sensitivity ($S_b = \Delta\lambda_{res}/\Delta n_{clad}$ [32]), quality factor of the resonance (Q-factor, $Q = \lambda_{res}/\Delta\lambda_{fwhm}$), and the limit of detection (LoD).

The limit of detection is the minimal refractive index change that a sensor can detect [33], which can be expressed as

$$\mathrm{LoD} = R/S_b, \tag{1}$$

where R stands for sensors resolution. It can be expressed as

$$R = 3\sqrt{\sigma_{SNR}^2 + \sigma_{Temp}^2 + \sigma_{\lambda}^2}, \tag{2}$$

where the first term is a standard deviation of spectral location due to signal-to-noise ratio (SNR), the second term is a result of thermal fluctuations, and the third term depends on the available wavelength resolution.

σ_{SNR} can be expressed as

$$\sigma_{SNR} = \frac{\lambda_{res}}{4.5Q(\mathrm{SNR})^{0.25}}, \tag{3}$$

and σ_{Temp} as

$$\sigma_{Temp} = S_T\sigma_T, \tag{4}$$

where S_T is thermal sensitivity and σ_T is the standard deviation in temperature.

Some authors define the limit of detection as $\lambda_{res}/(QS_b)$ [14,32,34]. However, this expression is simply proportional to LoD [Eq. (1)] if only the σ_{SNR} term in resolution is considered. Another common practice is to include only σ_λ in Eq. (2). But, as stated in [35], one cannot simply assume that the sensor resolution is identical to the discretization limit of one of the components of the system. Thus, in our analysis we include all three terms.

We first analyze how perforation depth (d) and length (l) affect resonant wavelength position closest to the edge of the photonic crystal induced bandgap. For this we performed a series of MPB simulations to obtain dispersion curves, containing a relationship between the wave vector (κ) and angular frequency (ω). This relationship, together with the microring resonance condition $m\lambda_{res} = 2\pi r_{Ring} n_{eff}$ [5], was used to obtain the resonance wavelength value. The resulting dependence of the resonance wavelength on d and l is shown in Fig. 2.

While waveguide bending was neglected in MPB simulations, comparison with full ring 3D FDTD simulations revealed that results are in satisfactory agreement. This in turn suggests that, for a 5100 nm radius microring, the effect of bending on resonance frequency position is small.

Assuming that resonance wavelength shift is toward longer wavelengths and that our measurement setup allows us to measure in a 1520–1630 nm wavelength window, we choose a resonance wavelength close to the lower edge, 1540 nm. Thus, the photonic bandgap below 1540 nm can be used as a reference point during sensor operation, giving a measurement range of 80 nm. If the direction of the resonance wavelength shift is not known beforehand, then the bandgap edge should be chosen at the middle of the measurable wavelength window (1575 nm).

From the surface plot intersection with the plane $\lambda_{res} = 1540$ nm, the relationship between d and l, for which the resonance closest to the photonic bandgap edge is situated at 1540 nm, was obtained. This relationship was approximated using the exponential function

$$l(d) = 1223.4e^{-0.0127d}. \quad (5)$$

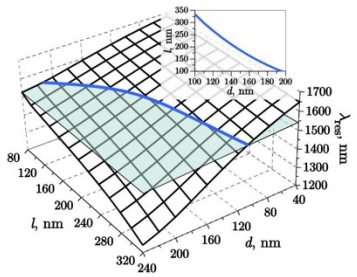

Fig. 2. Resonance wavelength of mode closest to the photonic bandgap as a function of perforation length (l) and depth (d). Transparent plane cuts surface at $\lambda_{res} = 1540$ nm.

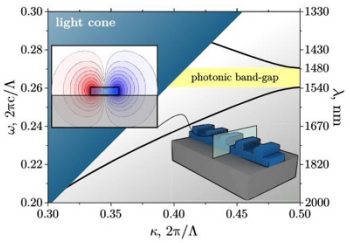

Fig. 3. Band diagram of a periodic segment forming a 1D photonic crystal inside the microring resonator ($d = 120$ nm). Inset shows distribution of electric field vector component perpendicular to the direction of propagation.

The band diagram for one set of such values (for which the actual microring resonator was fabricated) is shown in Fig. 3. The photonic bandgap can be seen to extend from 1480 to 1540 nm. The sensor depicted here operates in the lower frequency (or dielectric) band mode [15].

Analysis of the sensor performance was performed only with respect to the perforation depth and length (Fig. 1). Waveguide height is usually defined by the fabrication process and cannot be changed; width was chosen to correspond to single-mode quasi TE operation. We chose to keep the period and coupling gap constant due to the introduction of two additional degrees of freedom in both the Q-factor and bulk refractive index sensitivity; consequently, the limit of detection would go well beyond the scope of this article [7,9,10].

3. SENSOR PERFORMANCE

We next analyze how the microring resonator sensor performance depends on perforation depth and length values that satisfy Eq. (5), ensuring resonance positions at 1540 nm.

The bulk refractive index sensitivity (S_b) dependence on perforation depth is shown graphically in Fig. 4(a). We see that increasing the depth of the perforations results in a higher S_b. This result can be explained by a larger mode field overlap with cladding material. The overlap dependence quite closely mimics the one of S_b. Hence, this is evidence that the mode field is more significantly exposed to the surrounding media in strongly perforated microrings.

The spectral deviation due to thermal fluctuations was determined by simulating thermal sensitivity of the device and multiplying it by the assumed standard deviation in temperature. Thermal sensitivity was determined to increase with increasing perforation depth, as shown in Fig. 4(b), although it is negative because the thermo-optic coefficient of liquid (ethanol used in simulations, but the same holds for water) is negative and larger than the thermo-optic coefficient of silicon in its absolute value [36]. It was observed that a thermal sensitivity of zero can be obtained for d of approximately 103 nm, which is an attractive feature for designing sensors with a focus on thermal stability.

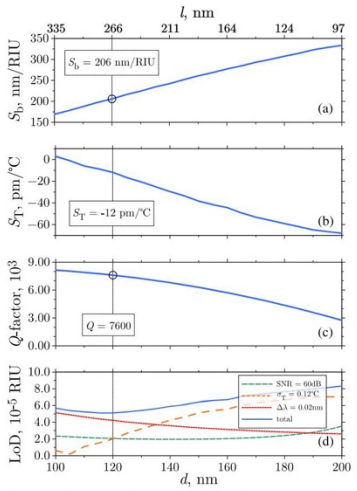

Fig. 4. Perforation depth (with a corresponding perforation length to maintain the 1540 nm resonance position) dependences of key microring sensor parameters. (a) Bulk refractive index sensitivity. (b) Thermal sensitivity. (c) Q-factor. (d) Limit of detection, for different dominant factors: SNR of 60 dB, temperature variation of 0.12 deg, spectral resolution of 0.02 nm, and all together.

Due to further decrease of mode field overlap with cladding material at smaller values of perforation depth, the thermo-optic coefficient of silicon starts to dominate effective index change, and thermal sensitivity becomes positive.

The effect of a larger mode field extension into the cladding material results in lower Q-factor values of deeper perforations, as shown in Fig. 4(c). The vertical lines at $d = 120$ nm denotes the perforation depth value for which a microring resonator sensor was fabricated. Simulations suggest a S_b value of 206 nm/RIU (refractive index unit) and a Q-factor of 7600. Contrary to the microring resonator sensor with partially etched cylindrical perforations [15], the partially etched rectangular perforations show a twofold increase in the bulk refractive index sensitivity (from 110 nm/RIU [15] to 207 nm/RIU).

The limit of detection exhibits a more complex dependence [see Fig. 4(d)]. Cases when only one term in Eq. (2) contributes to the resolution are presented. And, when all three terms are considered, the smallest LoD value is obtained for d close to 120 nm.

However, the location of smallest LoD value depends on exact contribution from each term. To analyze this further, we separately calculated the LoD of each term for a range of their values. The results are presented graphically in Fig. 5.

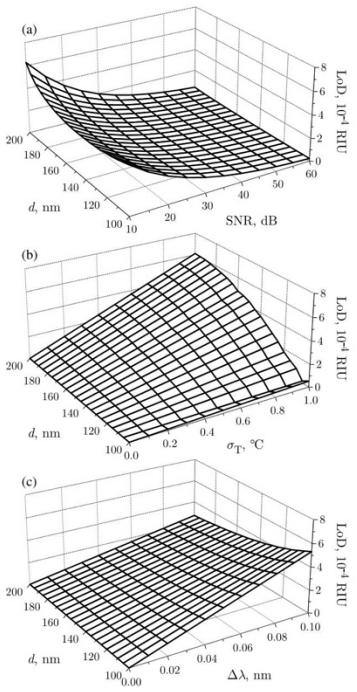

Fig. 5. LoD from various contributions. (a) SNR, varying from 10 to 60 dB; (b) σ_T; and (c) $\Delta\lambda$.

SNR influence on LoD depends on S_b and the Q-factor. Because one increases with increasing d and the other decreases, minimal LoD lands somewhere at the intermediate value of perforation depth. This might be better observed in Fig. 4(d).

Last, $\Delta\lambda$ effect [Fig. 5(c)] provides the least amount of new information, as it simply mirrors the dependence of S_b on perforation depth. Taken all together, we can summarize that, when considering LoD, some analysis must be performed to determine what form of perforation is most suited and which effect has the largest influence on a sensor's resolution.

4. FABRICATED MICRORING RESONATOR SENSOR

A perforated microring resonator was fabricated on an SOI platform at ePIXfab (*imec*, Leuven) using a standard CMOS

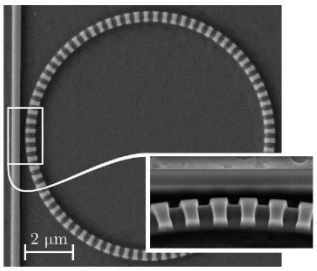

Fig. 6. Scanning electron microscopy image of the fabricated microring resonator. Inset shows enlarged view of coupling region between bus and microring waveguides.

process [37]. Scanning electron microscopy images of the fabricated device are shown in Fig. 6.

To test the sensor's performance, transmission spectra were measured with four different cladding materials: methanol (RI 1.3174), ethanol (RI 1.3522), isopropanol (RI 1.3661), and glycerol (RI 1.4571). Refractive index values at the free space wavelength of 1550 nm for all four materials are taken from [38]. Measured wavelength range was 1520–1630 nm. Refractive indices of all the materials were assumed to be uniform in this range.

Measured resonance wavelength positions were fitted using linear least squares to a straight line in the form $\lambda_{res}(n_{clad}) = C + S_b n_{env}$, where the slope of the line is bulk refractive index sensitivity.

Measured transmission spectra of the microring resonator are shown in Fig. 7(a). Compared with the plot shown in Fig. 7(b), which shows transmission spectra obtained via 3D FDTD simulations using microring parameters given in Section 2, we can conclude that a good agreement between measurements and simulation was obtained. However, resonances λ_2 and λ_4 from measurements do not correspond to any of the resonances in numerical simulation spectra. We expect those resonances to be a result of mode splitting [39,40] due to ring waveguide sidewall roughness and/or imperfections in photonic crystal structure. Also the extinction ratio (ER) in measurements was higher (19 dB) than in numerical simulations (12 dB). This disagreement can be accounted for by minute deviations in the coupling gap of the fabricated device (Fig. 1). It should be noted that FSR compression from 22 to 7 nm near the bandgap is expected due to strong dispersion induced by the photonic crystal.

As the refractive index of the cladding material is increased by changing the surrounding medium, resonance wavelength positions shift toward longer wavelengths. This shifting for all measured surrounding mediums is summarized graphically in Fig. 7(c). Each line is given a fitted linear equation with bulk refractive index sensitivity values. An experimentally obtained S_b value of resonance closest to the photonic bandgap λ_0 is 207.7 nm/RIU, which is in good agreement with numerical

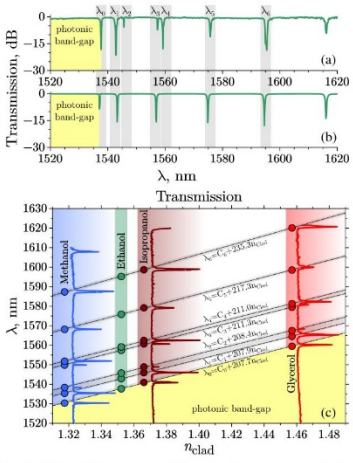

Fig. 7. Transmission spectra of the microring resonator embedded in methanol. (a) Experiment. (b) Simulation. (c) Resonance wavelength position and transmission spectra at various cladding materials.

simulations using MPB [206 nm/RIU, Fig. 4(a)] and 3D FDTD (214 nm/RIU).

The maximum resonance wavelength shift that can be measured with a fabricated resonator is 80 nm. With a bulk refractive index sensitivity of 207.7 nm/RIU, this gives a maximum measurable refractive index change of 0.385 RIU.

The quality factor of the resonances λ_0 shown in Fig. 7 is Q-factor = 2600 based on measurement and Q-factor = 7600 as deduced from 3D FDTD simulations [Fig. 4(c)]. The smaller value of a Q-factor in measurement can be attributed to the same reasons as mode splitting (sidewall roughness and irregularities in photonic crystal) and additionally to the fact that, in numerical simulations, absorption of cladding material was not taken into account. Assuming an SNR of 30 dB and temperature deviation of 0.12 deg, the limit of detection of a fabricated microring resonator sensor is 4.5×10^{-4} RIU.

5. CONCLUSIONS

In conclusion, we presented an analysis of a microring resonator with an integrated 1D photonic crystal for enhanced sensitivity and measurement range. The perforation-induced photonic bandgap can be used as a spectral reference to overcome limitations imposed by the FSR. Furthermore, we showed that, by adjusting perforation depth, the limit of detection can be minimized, depending on considerations of the leading factor determining sensor resolution. Numerical analysis was verified by experiment on a fabricated structure using organic solvents

DOI: 10.35848/1347-4065/ab9232
© IOP Publishing. Reproduced with permission. All rights reserved

Japanese Journal of Applied Physics

The Japan Society of Applied Physics

REGULAR PAPER

Microring resonators with circular element inner-wall gratings for enhanced sensing

To cite this article: Raimondas Petruškevičius *et al* 2020 *Jpn. J. Appl. Phys.* **59** SOOD02

View the article online for updates and enhancements.

This content was downloaded by raimondas from IP address 193.219.49.161 on 27/05/2020 at 06:10

Japanese Journal of Applied Physics **59**, SOOD02 (2020) **REGULAR PAPER**
https://doi.org/**10.35848/1347-4065/ab9232**

Microring resonators with circular element inner-wall gratings for enhanced sensing

Raimondas Petruškevičius[1*], Armandas Balčytis[1,2], Darius Urbonas[1], Konstantinas Vaškevičius[1], and Saulius Juodkazis[3,4]

[1]*Center for Physical Sciences and Technology, Savanorių ave. 231, LT-02300 Vilnius, Lithuania*
[2]*Graduate School of Engineering, Yokohama National University, 79-5 Tokiwadai, Hodogaya-ku, Yokohama 240-8501, Japan*
[3]*Optical Sciences Centre and ARC Training Centre in Surface Engineering for Advanced Materials (SEAM), School of Science, Swinburne University of Technology, Hawthorn, VIC 3122, Australia*
[4]*Tokyo Tech World Research Hub Initiative (WRHI), School of Materials and Chemical Technology, Tokyo Institute of Technology, 2-12-1, Ookayama, Meguro-ku, Tokyo 152-8550, Japan*

[*]E-mail: raimondas.petruskevicius@ftmc.lt

Received March 6, 2020; revised April 17, 2020; accepted May 11, 2020; published online May 26, 2020

We suggest that implementation of a circular element second order Bragg grating 1D photonic crystals into the inner-wall of silicon-on-insulator microring resonators increases the light-matter interaction strength and device free spectral range. Introduction of a specifically tailored grating changes the quality factor of a selected resonance and modulates the losses of the system, leading to the presence of longitudinal resonant air and dielectric Bloch modes. This phenomenon can be harnessed for the development of a self-referenced sensor that is immune to changes in ambient temperature and is well suited for both biomolecule and hydrogen gas exposure sensing. The recent results on numerical modeling, lithographic fabrication, and characterization of microring resonators with circular elements on inner-wall are presented.
© 2020 The Japan Society of Applied Physics

1. Introduction

Microring resonators are key components in integrated photonics, where they fulfill the function of a high quality factor cavity whilst maintaining a small device footprint. As such they lend themselves as fundamental building blocks for a staggering variety photonic applications, such as spectral filters, optical switches and routers, delay lines, lasers, as well as cavities for sensing.[1,2] The state of the art silicon-on-insulator (SOI) platform represents a cornerstone of contemporary telecommunications photonics and is among the most popular technologies for microring resonators. There SOI is attractive due to its compatibility with the well-established complementary metal oxide semiconductor (CMOS) process as well as a high refractive index contrast that enables strong mode field confinement and small waveguide bending radii.[3] However, the high mode field confinement exhibited by SOI resonators produces a disadvantage in sensing applications due to the relatively small overlap between cladding material and mode evanescent field. While the exceptionally rapid decay of the evanescent field around Si waveguide elements, estimated to decrease by a factor of $1/e$ at a distance of 63 nm,[4] is useful for surface bio-sensing of water-borne analytes, as it allows for higher specificity due to the signal being dominated by contributions from the functionalized surface layer. However, strong confinement is detrimental when bulk sensitivity is required such as in gas sensing. In this field functionalization is often achieved by applying various cladding materials, such as spray-coating triphenylene-ketal receptor for TNT detection,[5] drop-casting ZnO nanoparticles for ethanol sensing,[6] or dip-coating Pt-doped tungsten oxide in a sol-gel solution for hydrogen detection via catalytic combustion,[7,8] deposited at thickness values ranging from 150 nm to multiple micrometers.

In the case of microring resonators, several strategies have been proposed to overcome this limitation, including ultra-thin SOI microring resonators,[9] slotted waveguide microring resonators,[10] introduction of subwavelength grating structures[11–14] and photonic crystals inside the microring cavity,[15–19] and a microring with periodically arranged metal nanodisks.[20,21]

The possibility to fabricate microrings with different perforation depths and arrangements opens a new degree of freedom in device design. The loss-modified microring resonator can be created by integration of a second order Bragg grating that allows for control of leaky mode radiation losses, ejected out of the device plane. Modulation of a microring resonator by a periodic chain of Au nanodiscs thereby was able to filter out photonic modes of mismatched periodicity out of a SOI ring, enhancing sensitivity and free spectral range (FSR) of sensing performance.[20] In this paper, however, we present a fully dielectric microring resonator with a 2nd order annular Bragg grating, designed specifically to enhance sensitivity and increase the FSR of measurements. It exhibits similar effects as predicted in metal nanoparticle decorated designs,[20] however, here it is realized in SOI without introducing excessively lossy metals or performing multiple cumbersome lithography steps. This article details a partial version of results presented in.[22]

2. Methods

Numerical simulations of perforated microring structures were conducted using finite-element method (FEM)[12] and finite-difference time-domain (FDTD) method.[23,24] The perforated microring resonators were fabricated on SOI platform at ePIXfab (imec, Leuven) using a standard CMOS process by deep ultraviolet (DUV) lithography and by electron beam lithography (EBL) at Melbourne Center for Nanofabrication as well as at the Nanofabrication Facility at Swinburne University of Technology in Australia.[25] The experimental characterization of microrings was performed in the wavelength window 1520–1630 nm using a measurement setup (depicted in Fig. 1) equipped with a TE polarized tunable telecom continuous wave laser coupled into the integrated SOI waveguide devices through vertical grating couplers via a lensed fiber.[26] The transmitted light is likewise

 © 2020 The Japan Society of Applied Physics

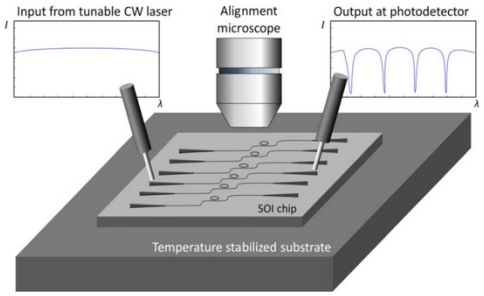

Fig. 1. (Color online) Schematic image of the characterization setup for transmittance spectral measurements. Light from a tunable telecom waveband laser is coupled into and out of the SOI chip via vertical lensed fibers. Representations of typical input and output spectra are given as insets.

collected through a fiber via grating couplers at the output ports and passed on to a telecom wavelength InGaAs detector. Alignment of coupling fibers is controlled by means of a microscope and a precision positioning stages.

3. Results

The structure under consideration is a loss-modified microring resonator with an integrated 2nd order Bragg grating [Figs. 2(a), 2(b)], introduced in order to increase the light-matter interaction with the surrounding medium and to attain control over the supported modes. The circular grating elements were placed asymmetrically, on the inner side of ring resonator, to reduce the modal overlap with confined radiation and thereby to attain more precise control of optical losses. Similarly, a circular shape of grating elements was chosen to minimize the introduced scattering losses. The use of circular element grating on outer-wall of microring is less practicable due to introduction of higher scattering losses and more difficult precise control of coupling gap between ring and bus waveguide during fabrication process. Changing the radii of the circular elements enables the tuning of evanescent field extension to the surrounding medium and control the losses of modes supported by the ring resonator. In particular, a 2nd order annular Bragg grating generates a vortex beam of light in the vertical direction to the ring surface.[27] This vertically propagating vortex beam corresponds to the zero diffraction order and a 2nd order photonic band gap is induced. Due to this band gap, the modes are also expected to experience mode splitting as the introduced elements lead to counter-propagating modes. The latter eliminates traveling modes and results in the buildup of two standing-wave resonances. These resonances are related to the appearance of even and odd standing-wave modes (E and O modes in Fig. 2[20]) as a symmetric and anti-symmetric superposition of the counter-propagating traveling waves, which corresponds to air and dielectric Bloch modes,[15] predominately located either in the surrounding air of grooves and inside the dielectric material of microring waveguide.

FEM and FDTD were used to numerically explore the effects introduced by periodic circular defects of increasing magnitude. The numerical simulation results are summarized in Fig. 3. The geometrical parameters of structure simulation assume a microring middle-radius of $R = 4$ μm, microring waveguide widths of 0.45 μm and 0.4 μm for bus waveguides, respectively, and a coupling gap of 130 nm. The total number of 2nd order Bragg grating elements was $m = 36$. When the introduced periodic circular incisions are at or above $r = 40$ nm, pronounced mode splitting at a 1.64 μm

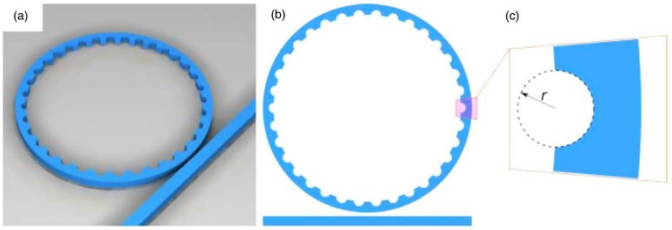

Fig. 2. (Color online) Microring resonator with a 2nd order annular Bragg grating. Sketch of the microring with a bus waveguide in (a) isometric and (b) top-down view. (c) Circular element of the 2nd order Bragg grating where r is the radius of the cylinder. White color indicates air ($n = 1$) and blue silicon (Si, $n = 3.476$), thickness of the silicon ~220 nm.

© 2020 The Japan Society of Applied Physics

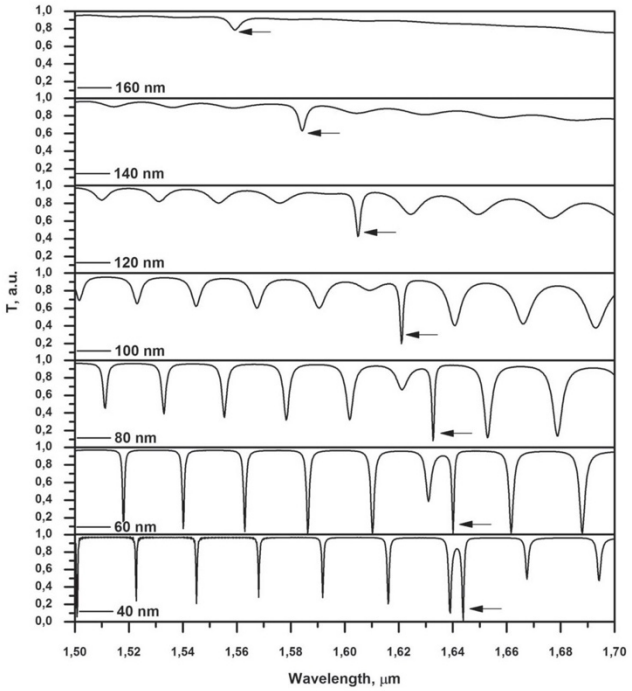

Fig. 3. Theoretical transmission spectra. The transmission for different microring resonators with varying radii r of the circular 2nd order Bragg grating elements. Here r is given in nanometers, the grating period is 0.734 μm and surrounding medium is PMMA (Poly methyl methacrylate, $n = 1.481$). Arrow indicates the dielectric Bloch mode, where $\mathbf{k} = 0$.

wavelength is induced, which is accompanied by leaky mode radiation in the vertical direction to the microring surface at wavenumber $\mathbf{k} = 0$, and, notably, the increase of the quality of factor of the split mode. The arrows in Fig. 3 indicate the high-Q dielectric Bloch mode of even symmetry. The air Bloch mode of odd symmetry has a considerably lower Q-factor due to grating induced scattering losses. The field intensity plots of both split resonances, corresponding to air and dielectric Bloch modes, are presented in Fig. 4.

It is defined in,[12] that, for $r = 0$ in this ring resonator geometry, critical coupling occurs at a 100 nm coupling gap width. Hence, our ring resonator is undercoupled as it employs a slightly larger coupling gap of 130 nm. As the grating element radii r are made larger, despite enhanced undercoupling due to changes in mode effective refractive index, the scattering losses in the system increase until only a single resonance mode—the dielectric Bloch mode—which matches the second order Bragg condition and has the highest intrinsic quality factor, remains. This situation is opposite to the case studied in,[20] where microring decorated by plasmonic Au nanodics supports an air Bloch mode of odd symmetry and filters the dielectric Bloch mode via damping by losses in the metal disks. In general, such filtering mechanisms enable the precise identification of the effective index of the guided mode, making it ideal for sensing applications as FSR plays less of a role (since other modes are suppressed) and a large resonance shift can be detected without ambiguity. The blueshift of all the spectral peaks (Fig. 3) is related to an effective mode refractive index decrease due to increased volume fraction of the radial grating elements.

EBL and DUV lithography were used to fabricate different microring resonators with 2nd order Bragg grating, which have varying radii r of the circular grating elements, varying from 0 to 160 nm in steps of 20 nm, with images of select examples given in Fig. 5. Each microring was coupled to two bus waveguides in an add-drop configuration for measurement and characterization purposes. While it was numerically

 © 2020 The Japan Society of Applied Physics

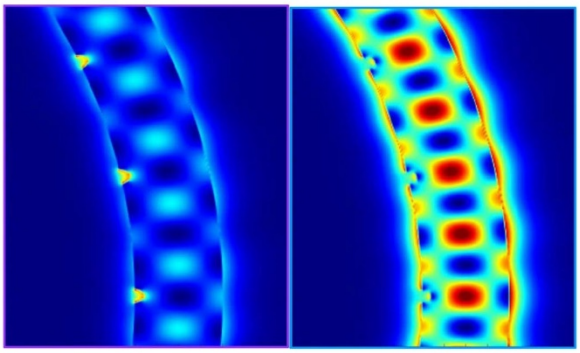

Fig. 4. (Color online) FDTD simulated mode distribution at 2nd order photonic band gap in annular grating modified micro-ring resonator with groove radii $r = 40$ nm. The field intensity plots of modes for the 2nd order Bragg grating split resonances: (a) air Bloch mode, (b) dielectric Bloch mode.

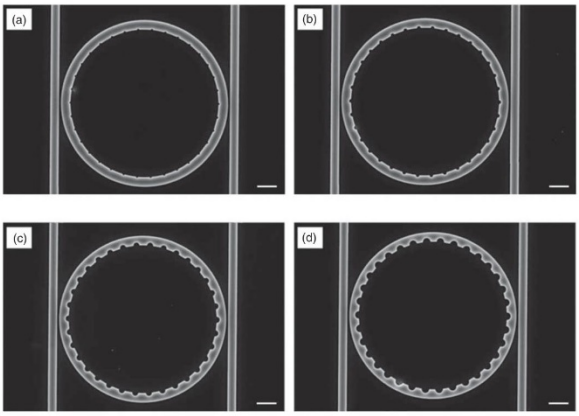

Fig. 5. Scanning electron microscopy images of fabricated microring resonators equipped with 2nd order Bragg gratings with varying radii of the circular grating elements. (a) $r = 40$ nm (b) $r = 80$ nm, (c) $r = 120$ nm, (d) $r = 160$ nm. The white scale bar represents 1 μm.

predicted that mode splitting would appear at 1.64 μm wavelength (Fig. 3), in experiment it was observed at 1.62 μm (Fig. 6). This mismatch between model and experiment can be attributed to variations in the Si device layer thickness and fabrication imperfections.

To experimentally verify the viability of the microring resonator with an integrated 2nd order Bragg grating as a sensor the device was exposed to different refractive index surrounding media (Fig. 7). Here, water (n =1.333) and 12% Glycerol water solution (n =1.348) were chosen as sensing materials. We approximated transmission spectra (Fig. 7) by Lorentzian curves with a least-square fitting method and obtained Q-factors for the radius of the circular grating element $r = 20$ nm [Fig. 7(a)] $Q_{A1} = 3153$, $Q_{D1} = 3408$, $Q_{A2} = 3976$, $Q_{D2} = 4189$, where notations A1 and D1 are used for air and dielectric Bloch modes in water and A2 and D2 used for air and dielectric Bloch modes in 12% Glycerol, respectively. For the radius of the circular grating element $r = 40$ nm [Fig. 7(b)], we obtained $Q_{A1} = 1849$, $Q_{D1} = 2942$, $Q_{A2} = 2165$, $Q_{D2} = 3017$, respectively. Because m is defined by design, it is easy to simulate effective losses of our microring resonator using $\alpha = m/(QR)$. For the radius of the circular grating element

© 2020 The Japan Society of Applied Physics

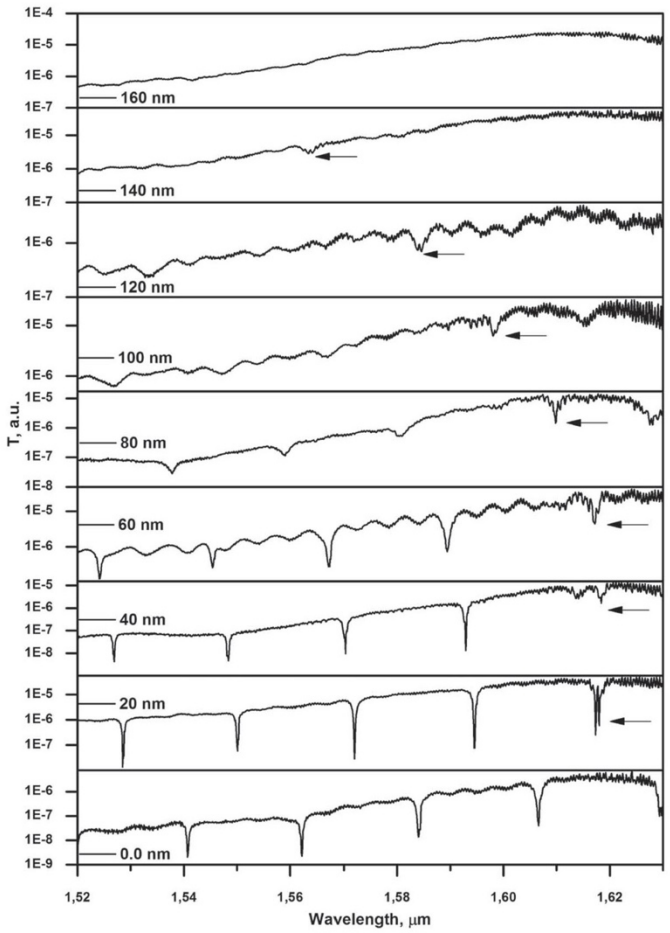

Fig. 6. Experimental transmission spectra exhibited by different microring resonators with varying radii r of the circular 2nd order Bragg grating elements. Here r is given in nanometers, the grating period is 0.734 μm and surrounding medium is PMMA. Arrow indicates the dielectric Bloch mode, where $k = 0$.

$r = 20$ nm [Fig. 7(a)], the losses are $\alpha_{A1} = 28.5\,\mathrm{cm}^{-1}$, $\alpha_{D1} = 26.4\,\mathrm{cm}^{-1}$, $\alpha_{A2} = 22.6\,\mathrm{cm}^{-1}$, $\alpha_{D2} = 21.5\,\mathrm{cm}^{-1}$. Furthermore, for the radius of the circular grating element $r = 40$ nm [Fig. 7(b)], the losses are $\alpha_{A1} = 48.7\,\mathrm{cm}^{-1}$, $\alpha_{D1} = 30.6\,\mathrm{cm}^{-1}$, $\alpha_{A2} = 41.6\,\mathrm{cm}^{-1}$, $\alpha_{D2} = 29.8\,\mathrm{cm}^{-1}$. The losses are mainly dominated by 2nd order Bragg grating induced scattering.

The measured sensitivity of such a resonator is approximately $S_A = 73.5$ nm/RIU for shifting of air Bloch mode and $S_D = 73.4$ nm/RIU for shifting of dielectric Bloch mode, respectively, due to changes in cladding refractive index, when circular grating element radii are $r = 20$ nm [Fig. 7(a)]. At this shallow microring resonator perforation depth, the device bulk sensitivity is approximately equal to that of a

© 2020 The Japan Society of Applied Physics

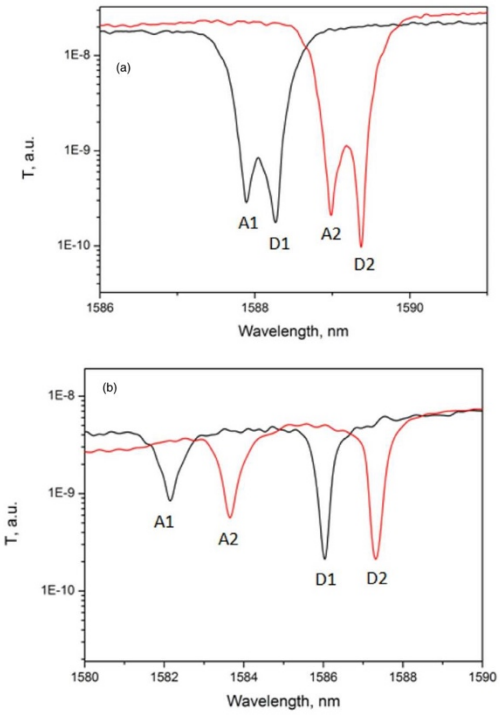

Fig. 7. (Color online) Transmission spectra of a microring resonator with second order Bragg grating having the radius of the circular grating element (a) $-r = 20$ nm, (b) $-r = 40$ nm. Here black curve indicates the transmission spectrum when the surrounding material is water ($n = 1.333$) and red-Glycerol 12% ($n = 1.348$). A1 and A2 are air Bloch mode resonances, D1 and D2—dielectric Bloch mode resonances.

conventional microring $S_b = 70$ nm/RIU.[3)] When perforation depth is increased to $r = 40$ nm [Fig. 7(b)], the measured sensitivity becomes $S_A = 102.1$ nm/RIU for air Bloch mode and $S_D = 83.1$ nm/RIU for dielectric Bloch mode. Hence, the experimental sensitivity of air Bloch mode is roughly 1.5 times larger than the sensitivity of an unmodified microring resonator.

As reported previously for different perforated microring designs, the sensitivities had been measured $S_b = 81.7 \div 95.0$ nm/RIU for partial depth circular hole first order Bragg grating implemented in SOI microring[15)] and $S_b = 207.7 \div 235.3$ nm/RIU for rectangular first order Bragg grating implemented in SOI microring.[17)] However, the main advantage of this proposed scheme is the self-referenced detection enabled by 2nd order Bragg grating induced controllable mode splitting. Despite higher optical losses and a lower Q-factor [Fig. 7(b)] of air Bloch mode, this mode is more sensitive to the surrounding medium than the waveguide-confined dielectric Bloch mode. This peculiarity of mode splitting induced by a 2nd order Bragg grating can be used for the development of a self-referenced sensor that would be similar to that suggested in[28)] based on coupled microcavities ("photonic molecules") or in[29)] based on a single Au nano disk attached to a microring resonator. This self-referenced sensor could be immune to changes of the ambient parameters, such as temperature, and capable of discriminating between bulk index changes and specific/nonspecific surface binding events. This provides a significant advantage over conventional microring resonator sensors for drug discovery, point-of-care testing applications and sensing of gases.[30)]

Harnessing the feature of coherent perfect absorption of split Bloch modes,[31–33)] if the surrounding medium exhibits an absorption coefficient that is dependent on hydrogen gas concentration, such as Pd or WO_3 nano materials,[6–8)] it is

© 2020 The Japan Society of Applied Physics

possible to develop a hydrogen gas sensor based on excitation of an air Bloch mode that is immune to changes of temperature induced by exothermic catalyst burning reactions of Pd or WO_3 hydrides in ambient air conditions.

4. Conclusion

It is established that microrings with implemented 2nd order Bragg gratings can have enhanced quality factors and sensitivity to external cladding environment. For loss-modified microring resonators with second order Bragg grating, the annular grooves filter out photonic non-matching modes of a SOI ring, enhance sensitivity and FSR of the sensor, which is useful for development of self-referenced bio and hydrogen gas sensors.

Acknowledgments

This research was partially supported by a grant No. S-LJB-19-1 from Research Council of Lithuania the Joint Research Project hybRING between Lithuania and Japan. A.B. is an International Research Fellow of the Japan Society for the Promotion of Science [Postdoctoral Fellowships for Research in Japan (Standard)].

1) M. S. Luchansky and R. C. Bailey, "High-Q optical sensors for chemical and biological analysis," Anal. Chem. **84**, 793 (2012).
2) F. Vollmer and L. Yang, "Label-free detection with high-Q microcavities: a review of biosensing mechanisms for integrated devices," Nanophotonics **1**, 267 (2012).
3) W. Bogaerts, P. DeHeyn, T. VanVaerenbergh, K. De Vos, S. K. Selvaraja, T. Claes, P. Dumon, P. Bienstman, D. Van Thourhout, and R. Baets, "Silicon microring resonators," Laser Photonics Rev. **6**, 47 (2012).
4) M. S. Luchansky, A. L. Washburn, T. A. Martin, M. Iqbal, L. C. Gunn, and R. C. Bailey, "Characterization of the evanescent field profile and bound mass sensitivity of a label-free silicon photonic microring resonator biosensing platform," Biosens. Bioelectron. **26**, 1283 (2010).
5) R. Orghici, P. Lützow, J. Burgmeier, J. Koch, H. Heidrich, W. Schade, N. Welschoff, and S. Waldvogel, "A microring mesonator sensor for sensitive detection of 1,3,5-trinitrotoluene (TNT)," Sensors **10**, 6788 (2010).
6) N. A. Yebo, P. Lommens, Z. Hens, and R. Baets, "An integrated optic ethanol vapor sensor based on a silicon-on-insulator microring resonator coated with a porous ZnO film," Opt. Express **18**, 11859 (2010).
7) N. A. Yebo, D. Taillaert, J. Roels, D. Lahem, M. Debliquy, D. Van Thourhout, and R. Baets, "Silicon-on-insulator (SOI) ring resonator based integrated optical hydrogen sensor," IEEE Photonics Technol. Lett. **21**, 960 (2009).
8) S. Matsuura, N. Yamasaku, Y. Nishijima, S. Okazaki, and T. Arakawa, "Characteristics of highly sensitive hydrogen sensor based on Pt-WO3/Si microring resonator," MDPI Sens. **20**, 96 (2020).
9) S. T. Fard et al., "Performance of ultra-thin sol-based resonators for sensing applications," Opt. Express **22**, 14166 (2014).
10) C. A. Banios, K. B. Gylfason, B. Sanchez, A. Griol, H. Sohlstroem, M. Holgado, and R. Casquel, "Slot waveguide biochemical sensor," Opt. Lett. **32**, 3080 (2007).
11) J. G. Wangueemert-Perez, P. Cheben, A. Ortega-Monux, C. Alonso-Ramos, D. Perez-Galacho, R. Halir, I. Molina Fernandez, D.-X. Xu, and J. H. Schmid, "Evanescent field waveguide sensing with subwavelength grating structures in silicon-on-insulator," Opt. Lett. **39**, 4442 (2014).
12) M. Gabalis, D. Urbonas, and R. Petruskevicius, "A perforated microring resonator for optical sensing applications," J. Opt. **16**, 105003 (2014).
13) Z. Wang, X. Xu, D. Fan, Y. Wang, and R. T. Chen, "High quality factor subwavelength grating waveguide micro-ring resonator based on trapezoidal silicon pillars," Opt. Lett. **41**, 3375 (2016).
14) Z. Tu, D. Gao, M. Zhang, and D. Zhang, "High-sensitivity complex refractive index sensing based on Fano resonance in the subwavelength grating waveguide micro-ring resonator," Opt. Express **25**, 20911 (2017).
15) D. Urbonas, A. Balcytis, K. Vaikevicius, M. Gabalis, and R. Petruskevicius, "Air and dielectric bands photonic crystal microring resonator for refractive index sensing," Opt. Lett. **41**, 3655 (2016).
16) T. Ma, L. Sun, J. Yuan, X. Sang, B. Yan, K. Wang, and C. Yu, "Integrated label-free optical biochemical sensor with a large measurement range based on an angular grating-microring resonator," Appl. Opt. **55**, 4784 (2016).
17) K. Vaskevicius, M. Gabalis, D. Urbonas, A. Balcytis, R. Petruskevicius, and S. Juodkazis, "Enhanced sensitivity and measurement range SOI microring resonator with integrated one dimensional photonic crystal," J. Opt. Soc. Am. B **34**, 750 (2017).
18) S. M. Lo, S. Hu, G. Gaur, Y. Kostoulas, S. M. Weiss, and P. M. Fauchet, "Photonic crystal microring resonator for label-free biosensing," Opt. Express **25**, 7046 (2017).
19) N. Acharyya, M. Maher, and G. Kozyreff, "Portable microresonator-based label-free detector: monotonous resonance splitting with particle adsorption," Opt. Express **27**, 34997 (2019).
20) D. Urbonas, A. Baldytis, M. Gabalis, K. Vaskevicius, G. Naujokaite, S. Juodkazis, and R. Petruskevicius, "Ultrawide free spectral range, enhanced sensitivity and removed mode splitting SOI optical ring resonator with dispersive metal nanodisks," Opt. Lett. **40**, 2977 (2015).
21) R. Ahmed, A. A. Rifat, A. K. Yetisen, M. S. Salem, S.-H. Yun, and H. Butt, "Optical microring resonator based corrosion sensing," RSC Adv. **6**, 56127 (2016).
22) R. Petruškevičius, A. Balčytis, D. Urbonas, M. Gabalis, K. Vaškevičius, and S. Juodkazis, "Perforated micro-ring resonators for enhanced sensing," IEEE Proc., Inter. Conf. 24th Microoptics Conf. (MOC2019), 2019 (Toyama, Japan), p. 320, November 17–20.
23) A. Taflove and S. C. Hagness, *Computational Electromagnetics: The Finite-Difference Time-Domain Method* (Artech House, Boston, 2005), p. 852.
24) D. Urbonas, M. Gabalis, and R. Petruskevicius, "Numerical simulation of microring resonator biosensor with FDTD algorithms based on GPU B-CALM and CPU Meep," Opt. Quantum Electron. **46**, 1021 (2014).
25) A. Balcytis, G. Seniutinas, D. Urbonas, M. Gabalis, K. Vaskevicius, R. Petruskevicius, G. Molis, G. Valusis, and S. Juodkazis, "High precision fabrication of antennas and sensors," SPIE Proc. **9446**, 94461G (2015).
26) X. Xu, H. Subbaraman, J. Covey, D. Kwong, A. Hosseini, and R. T. Chen, "Complementary metal–oxide–semiconductor compatible high efficiency subwavelength grating couplers for silicon integrated photonics," Appl. Phys. Lett. **101**, 031109 (2012).
27) X. Cai, J. Wang, M. J. Strain, B. Johnson-Morris, J. Zhu, M. Sorel, J. L. O'Brien, M. G. Thompson, and S. Yu, "Integrated compact optical vortex beam emitters," Science **338**, 263 (2012).
28) S. V. Boriskina and L. D. Negro, "Self-referenced photonic molecule bio (chemical)sensor," Opt. Lett. **35**, 2496 (2010).
29) C. M. Campanella, M. Dunai, L. Calabrese, and C. E. Campanella, "Design guidelines for nanoparticle chemical sensors based on mode-splitting silicon-on-insulator planar microcavities," J. Opt. Soc. Am. B **33**, 2383 (2016).
30) C. E. Campanella, M. De Carlo, A. Cuccovillo, F. De Leonardis, and V. M. N. Passaro, "Methane gas photonic sensor based on resonant coupled cavities," MDPI Sens. **19**, 5171 (2019).
31) P. Malara, C. E. Campanella, A. Giorgini, S. Avino, P. De Natale, and G. Gagliardi, "Super-resonant intracavity coherent absorption," Sci. Rep. **6**, 28947 (2016).
32) W. R. Sweeney, C. W. Hsu, S. Rotter, and A. D. Stone, "Perfectly absorbing exceptional points and chiral absorbers," Phys. Rev. Lett. **122**, 093901 (2019).
33) Q. Zhong, J. Ren, M. Khajavikhan, D. N. Christodoulides, Ş. K. Özdemir, and R. El-Ganainy, "Sensing with exceptional surfaces in order to combine sensitivity with robustness," Phys. Rev. Lett. **122**, 153902 (2019).

 © 2020 The Japan Society of Applied Physics

Vilniaus universiteto leidykla
Saulėtekio al. 9, LT-10222 Vilnius
El. p. info@leidykla.vu.lt,
www.leidykla.vu.lt
Tiražas 15 egz.